UNIVERSITY OF MIAMI

# MEAN BOUNDARY LAYER STRUCTURE AND TURBULENCE ASSOCIATED WITH FAIR WEATHER CUMULUS CLOUDS DURING RICO 2005

By

Shaunna Donaher

A THESIS

Submitted to the Faculty
of the University of Miami
in partial fulfillment of the requirements for
the degree of Master of Science

Coral Gables, Florida

May 2007

UNIVERSITY OF MIAMI

A thesis submitted in partial fulfillment of
the requirements for the degree of
Master of Science

# MEAN BOUNDARY LAYER STRUCTURE AND TURBULENCE ASSOCIATED WITH FAIR WEATHER CUMULUS CLOUDS DURING RICO 2005

Shaunna Donaher

Approved:

| | |
|---|---|
| _____ | _____ |
| Dr. Bruce A. Albrecht<br>Professor of Meteorology | Dr. Steven G. Ullmann<br>Dean of the Graduate School |
| _____ | _____ |
| Dr. Paquita Zuidema<br>Assistant Professor of Meteorology | Dr. Pavlos Kollias<br>Assistant Professor of Meteorology<br>McGill University |

DONAHER, SHAUNNA (M.S., Meteorology & Physical Oceanography)
Mean Boundary Layer Structure and Turbulence (May 2007)
Associated with Fair Weather Cumulus Clouds
During RICO 2005

Abstract of a thesis at the University of Miami.

Thesis supervised by Professor Bruce A. Albrecht.
No. of pages in text. (96)

Between November 2004 and January 2005, the first large scale field experiment in decades to study fair weather cumulus clouds in the Eastern Atlantic Trade Wind Regime took place, called Rain In Cumulus over the Ocean (RICO). There were many observational components of RICO including aircraft flights, land-based radars and soundings, and ship-based observations. Observations on the ship provided information about boundary layer structure, fractional cloudiness, cloud depth and rainfall characteristics that are used to classify the cruise period into four distinct synoptic periods. This study uses vertically staring lidar data from the ship to study the subcloud region of the boundary layer in detail and describe the turbulence structure and mass flux into cloud base. This is the first application of Doppler lidar to subcloud layer turbulence in oceanic fair weather cumuli. The observed boundary layer and turbulence structures are composited for the four synoptic periods. The results from the synoptic periods with suppressed convective conditions coincide with those from previous studies based on aircraft observations which found increasing vertical velocity variance in the lower half of the subcloud layer with decreasing variance from the middle up to cloud base. In contrast, results from the convective synoptic periods show a different structure of increasing vertical velocity variance from the middle of the subcloud layer extending up to cloud base. Vertical velocity spectra show an overall increase in vertical velocity

variance just below cloud base, which is controlled by the presence of clouds. Lidar observations of fractional cloudiness (cruise average of .30) are compared with observations from the ceilometer (cruise average of .39) and are typically found to be significantly lower. The correlations between clouds and strong updrafts are calculated and are found to remain constant despite the variations due to synoptic conditions, with clouds and strong updrafts occurring together 6-7% of the time. Downdrafts are found to play a significant role at cloud base when a cloud is active, but not to be as important when a cloud is weak and shallow. These results are discussed and summarized and an outlook for future work and research programs is provided.

This thesis is dedicated to my father, who never once allowed me to believe that it couldn’t be done.

**ACKNOWLEDGEMENTS**

Several people were instrumental in the completion of this work and the least I can do to show them my appreciation is to acknowledge them.

First of all, I would like to thank my advisor Dr. Bruce Albrecht for offering me the opportunity and ample resources to pursue this research project. The entire RSMAS experience has been wonderful, including the opportunities to meet and work with top individuals in the field, and the ability to participate in field experiments. Dr. Albrecht has been a wonderful mentor and role model and is very generous to share his seemingly endless knowledge and experiences in the field of meteorology. I am grateful to him for always being kind and patient with his suggestions, and I thank him for all of his support during this thesis.

Dr. Pavlos Kollias is another individual whose encouragement was instrumental in my pursuing of this degree. His growing research interests and his will to share his knowledge and experience with me were motivational towards the accomplishment of my task.

In addition, I would like to express my appreciation to Dr. Paquita Zuidema, who served as member of my committee and encouraged me many times by showing interest in my work. She also provided some of the data used in this study and generously allowed me to stay with her for a week during a trip to NOAA to discuss this thesis, and for that I am very grateful.

Special thanks are due to Drs. Sara Tucker and Alan Brewer at the Earth Science Research Laboratory of NOAA in Boulder, CO. I had the opportunity to meet and work

with these two great individuals during the RICO cruise, and I learnt so much about the lidar during that time. They generously provided the majority of the data used in this study and shared a lot of their knowledge with me. It was a pleasure to get to know both of them during the course of this research, and I cannot thank Dr. Tucker enough for all of her help and support, both personally and with this project. Dr. Chris Fairall of NOAA also gets many thanks for providing the flux data.

I would also like to thank the UM radar group, including Virendra Ghate, Ieng Jo, Efthymios Serpetzoglou, and Tom Snowdon for their help and support over these past 3 years. Dan Voss was instrumental in providing computer support and friendship. Vinny gets a special acknowledgement for not charging me for all the help he gave me, even though he threatened to. Thanks also go to our two undergraduate assistants, Kristen Rasmussen and Gregory Izzo for their work on RICO data.

Moreover, I would like to thank Chris, Kelly, Josi, Liz, Evan, Martha, and my other RSMAS friends for being there for me during this experience. Their friendship and support has helped to make this process even more enjoyable.

I would like to thank my parents Susan and Tony, my brother Kevin, my grandmother Alexia, and the rest of my family for their endless love, support and encouragement throughout my entire academic career. My new family, the Donahers', has been extremely encouraging and supportive of my goals, and I thank my uncle-in-law Thomas for his scientific comments on this thesis. Finally, I would like to thank my husband Ryan for being so understanding and patient while I followed this dream. The year that we were apart was challenging, and I can only hope that he knows how much his moving to

Miami for me has meant. Both of our families have been far away from us these past 3 years, but they are closer than ever in my mind and heart.

# TABLE OF CONTENTS

## LIST OF TABLES

## LIST OF FIGURES

# LIST OF EQUATIONS

# Chapter 1- Introduction

## 1.1 Motivation

During the last four decades, marine fair weather cumulus clouds have been the focus of theoretical/modeling studies (e.g. Albrecht 1981; Albrecht 1993, Bretherton and Park 2007) and field experiments (e.g. Holland and Rasmusson 1973; Augstein et al. 1973). Shallow, oceanic cumulus convection is one of the most prevalent cloud types on Earth, although only a small percentage of these clouds may be considered active (contain active updrafts) at any given time (Albrecht 1989). Fair weather cumuli (FWC) typically exist in the trade wind regime of steady northeast winds in the tropics, are closely tied to surface fluxes through thermals in the boundary layer, and are dominated by warm rain processes (cloud tops below 0 °C). Advection, convection, and radiation maintain a characteristic thermodynamic structure with a cloud layer that is often capped by an inversion of sufficient strength to inhibit deep convection (Albrecht 1993). Fair weather cumuli are present over much of the tropical oceans, and characterizing their properties is important towards understanding the global energy balance and climate, improving large-scale climate and weather forecast models, and even for basic and highly idealized cloud models that rely on information about entrainment and precipitation processes (Kollias et al. 2001).

In the Northern Hemisphere, typical trade wind conditions involve east or northeast wind directions as winds blow from the high-pressure area in the horse latitudes (30-35$^{o}$N) towards the low-pressure area around the equator. During the winter season, this

flow is generally uninterrupted by strong convective events and is only varied by troughs, high pressure air masses and small systems embedded in the trade wind flow. During the summer months, tropical systems and deep convection can disrupt the "typical" trade wind zonal flow along the southern parts of the subtropical highs. Trade cumuli are the visible manifestation of the vertical transport of heat and moisture from the well mixed layer near the ocean surface and thus their role is crucial to the chain of atmospheric energy supply. Heated by the sun, the warm tropical oceans generate a near surface well-mixed layer (typically from the surface to 500-650 m height). The well mixed conditions are maintained by thermal-turbulent eddies 50-150 meters in diameter. At the top of the well-mixed layer is the Lifting Condensation Level (LCL) and beyond this altitude we have the formation of FWC. The vertical development of the FWC depends on the atmospheric stability and the strength of the thermals in the subcloud layer that support the FWC. A large fraction of the FWC die out in the early stages due to entrainment and mixing, but those that survive help to distribute water vapor through a layer about 1.5-2 km deep (Malkus 1958). The top of this moist layer is typically capped by a stable layer—the trade wind inversion.

A good area to study FWC is the tropical Atlantic, especially to the east of the Leeward Islands. In this area, FWC develop, evolve and dissipate in a pure oceanic environment away from land or human effects. The large area of open Atlantic Ocean under this trade wind regime extends from the western coast of Africa westward to about 61.5$^{o}$W and from about 10$^{o}$N to 25$^{o}$N in latitude.

In this study, data collected during the Rain In Cumulus over the Ocean (RICO, Rauber et al. 2007b) research cruise are used to study oceanic FWC and boundary layer

structures in their purest uninfluenced form. The main objectives in this study are to characterize the boundary layer structure and use Doppler lidar observations in the upward facing mode to study subcloud layer turbulence and examine the relationship between subcloud turbulence, convection and precipitation.

### 1.2 Background

Many field experiments on the trade wind regime in the tropical Atlantic Ocean took place in the late 1960s and early 1970s and collected a plethora (for that time, but not by today's standards) of data, much of which is still frequently referenced today (e.g. Holland and Rasmusson 1973; Nicholls and LeMone 1980; Augstein et al. 1973; LeMone and Pennell 1976). However, our observational knowledge of the trade wind conditions has not progressed substantially since this time due to a lack of field experiments in this region. Almost all of our advances in understanding fair weather cumulus clouds over the past three decades have come from modeling (e.g. Albrecht 1981; Albrecht 1993). The five major field experiments that have provided our general understanding of the trade wind conditions in this region are ATEX, BOMEX, GATE, and two separate experiments in Puerto Rico. A common characteristic of these previous experiments is the very good description of the boundary layer thermodynamic structure but with little or not actual measurements of FWC beside a few aircraft in-situ measurements. In contrast, during RICO sophisticated new remote sensors such as cloud radars and Doppler lidar were used to provide a detail view of clouds and their environment. Each experiment is briefly described below.

**Puerto Rico- Experiment 1**

Two experiments were done just to the north of Puerto Rico, the first by Malkus in April 1946 in which the trades were strong from the northeast and trade cumulus convection was vigorous (Malkus 1958). This study included aircraft, pilot balloon observations, and meteorological observations from a research vessel. This study concluded that in the subcloud layer eddies 50-150 meters across were common, but that there was no evidence of cloud-scale motions below clouds base except in precipitating downdrafts (Malkus 1958).

**ATEX**

The Atlantic Trade Wind Experiment (ATEX) took place in the Atlantic Northeast Trades, around $10^{o}$N and $30^{o}$W, from February 6-21, 1969. Data were collected from 3 (4 in the first period) ships that formed a triangle and moved together throughout the region. Data were collected in the lowest 4 km of the atmosphere by radiosondes, radar, buoys and deck-level observations (Augstein et al. 1973). This experiment encountered mostly suppressed conditions, which is typical of wintertime in the trades. Under these conditions, they were able to characterize the boundary layer into 5 subdivisions, which are described in more detail in Chapter 3.

**BOMEX**

The Barbados Oceanographic and Meteorological Experiment (BOMEX) took place during May and June of 1969 over the area east of Barbados. The season was chosen to provide a wide range of convective activity without well-developed storms (Holland and

Rasmusson 1973). Again there was a 5-ship array of 500 km, as well as radiosondes and radar and satellite observations. In addition to these, there were aircraft flying the perimeter of the array and releasing dropsondes. The primary objective of this experiment was to determine the rate of transfer of water vapor, heat, and momentum from the tropical ocean to the atmosphere by examining the atmospheric budgets of mass, water vapor, heat, momentum, and mechanical energy (Holland and Rasmusson 1973).

**Puerto Rico –Experiment 2**

The second experiment done to the north of Puerto Rico was by LeMone and Pennell on December 14-15, 1972. This study was an intense aircraft project with the intent of studying both mean and turbulent quantities of wind, temperature, humidity. The major findings of this study were that in highly suppressed cases, the cloud distribution was dependent on the subcloud roll vortices, but in the enhanced cases (active but non-precipitating FWC) the predominant coupling was by well-defined cloud scale updrafts which were traceable to at least 100 meters below cloud base. Due to these interactions, the fluxes of moisture and momentum in the upper subcloud layer were found to be strongly coupled to cloud distribution (LeMone and Pennell 1976).

**GATE**

The GARP Atlantic Tropical Experiment (GATE) observations were made from June-September 1974 mainly from aircrafts equipped with gust probes, but also from a 5-ship array located around $9^{o}$N and $23^{o}$W. An unusual aspect of this experiment is that in addition to radars, satellites and radiosondes, it used tethered balloons attached to the

ships to collect continuous data from the boundary layer (BL) (Emmitt 1978). This study found updrafts extending from near the ocean surface to just above cloud base. They classified updrafts and downdrafts and found that about 80% were either warm/moist (up) or cold/dry (down) relative to their immediate environments, showing the stabilization effect of cloud transports on the subcloud layer (Emmitt 1978).

The most recent field experiment to study tropical Atlantic FWC was RICO, which took place during November 2004- January 2005 off the Caribbean Islands of Antigua and Barbuda within the Northeast Trades of the western Atlantic. An overall objective of RICO was to characterize and understand the properties of trade wind cumulus at all scales, with particular emphasis on determining the importance of precipitation (RICO Operations Plan 2004). Not only is RICO the first major field experiment to study the trade wind boundary layer in several decades, it is one of the first experiments at sea where a lidar has been included. This means that advances in technology will not only help to make our observations from previously used instruments better, but that we will gain a new perspective of the detail of the subcloud region through the use of the lidar.

### 1.3 Scientific Objectives

The main focus of the thesis is to improve our understanding of the processes that maintain and perturb the boundary layer structure associated with marine fair weather cumulus clouds, with a strong focus on the subcloud layer turbulence.

Properties such as cloud fraction, heating rate, parcel vertical velocity, water vapor and liquid water content play a substantial role on the lifecycle and evolution of marine fair weather cumuli and their statistical characteristics are essential for realistic climate model simulations. Mean profiles of the thermodynamic variables (e.g. potential temperature, mixing ratio, wind speed and direction) can provide baseline boundary layer structures for testing models and evaluating the effect that structure may have on boundary layer cloudiness (Albrecht et al. 1995).

Under this context, the specific scientific objectives to be addressed in this study are:

I. Investigate the coupling between the observed boundary layer cloud variability and subcloud turbulence.

I attempt to analyze the effects of updrafts on the subcloud layer by examining the updraft-downdraft statistics and calculating the mass flux throughout the subcloud layer following a method used for Doppler cloud radar observations (Kollias and Albrecht 2000). These subcloud turbulence characterizations are compared with surface flux data to examine the connections between the mass flux and the vertical velocity statistics on the surface fluxes.

II. Estimate the temporal and spatial scales of variability of cloud properties and boundary layer structure during RICO.

III. Analyze the observed variability and the interconnection between MABL cloud properties and surface meteorology variables and radiative fluxes.

The role of the large-scale ocean and atmospheric dynamics on influencing the MABL structure and variability is also examined. The Climate Diagnostics Center (CDC) web interactive plots were used to obtain the regional Sea Surface Temperature (SST) and Sea Level Pressure (SLP) patterns, the atmospheric pressure systems evolution and surface wind plots in the area.

# Chapter 2- Data Collection and Analysis Procedures

## 2.1 Experiment Description

The RICO field experiment took place during November 2004- January 2005 off the Caribbean Islands of Antigua and Barbuda within the Northeast Trades of the western Atlantic. This time period was specifically selected to study trade wind clouds while avoiding hurricanes and deep convection (Rauber et al. 2007b). Under typical wintertime trade wind conditions it is usual to find a well-mixed subcloud layer topped by numerous shallow non-precipitating clouds (Nicholls and LeMone 1980). There were many observational components of RICO, including aircraft missions by the NCAR/NSF Hercules C-130, University of Wyoming King Air 200T and Facility for Airborne Atmos. Meas. (FAAM) BAE 146-301 that sampled clouds and cloud systems, a ground-based SPol-Ka radar based on Barbuda that observed large clouds and rainfall surrounding the island, rawinsondes launched from Barbuda, aerosol measurements on Antigua and Puerto Rico and ship-based instrumentation onboard the *R/V Seward Johnson*, which is described in more detail in the next section. In addition to the various means of data collection, RICO also had an outreach component, forecasting team and seminar series.

## 2.2 Cruise Description

This study is focused on data collected onboard the *R/V Seward Johnson* which is owned and operated by Harbor Oceanographic out of Ft. Pierce, FL. The ship left Florida

on December 28, 2004 and was scheduled to arrive at the experiment site on January 4, 2005. However, due to rough weather and unforeseen ship mechanical problems, it was delayed for a few days in Puerto Rico. While some intermittent data were collected during the ship repairs, this study is only going to focus on the data collected during the official RICO portion of the cruise, from 1/09/05- 1/14/05 (Leg 1) and 1/16/05-1/24/05 (Leg 2).

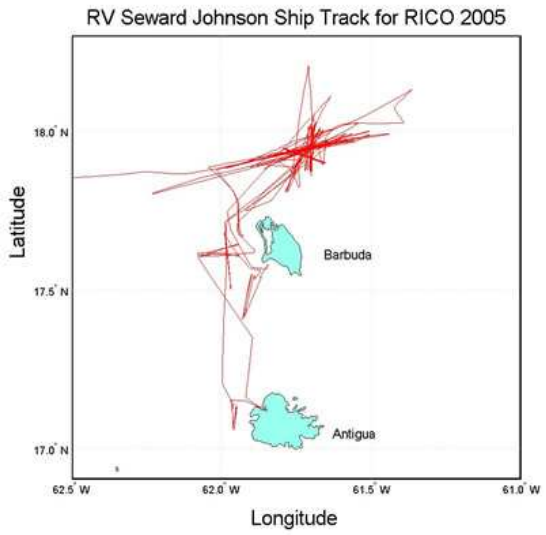


Figure 2.1: Ship Track for R/V Seward Johnson during RICO 2005 cruise (1/09 – 1/23).

Figure 2.1 illustrates the ship track during RICO. The typical observing strategy was to spend two hours traveling continuously into the trade winds and then quickly return to the starting point and repeat this track. This was done since a continuous upwind journey lasting at least 2 hours was needed for high quality averages of flux tower data. Other than a one day port stop in Antigua between two legs of the experiment, the ship sampled NE (upwind) of Barbuda to avoid land effects.

### 2.2.1 Instrumentation Onboard

The RICO research cruise was a collaborative effort between the National Oceanic and Atmospheric Administration (NOAA) Physical Science Division, the University of Colorado and the University of Miami (UM). An extensive suite of instruments was deployed onboard the research vessel for making measurements of boundary layer clouds and thermodynamic structure, as well as surface fluxes and meteorology. The remote sensing systems that were used on the cruise and the parameters they measure are described briefly in Table 2.1. Instruments on the ship included a ceilometer, a 2-channel microwave radiometer and 3 radar-- an 8.6 mm scanning Doppler cloud radar, a 3.2 mm vertically pointing Doppler cloud radar, and 3.2 cm vertically pointing Doppler radar-- and a Doppler lidar (described in detail below). Surface meteorology, air-sea fluxes, turbulence and radiative flux measurements as well as aerosol spectrometer measurements and rain gauges provided a near surface complement to these remote sensing instruments. Rawinsonde launches were made 4-6 times daily (with a cruise total of 77 successful launches) with Vaisala GPS RS-92 sondes to define the thermodynamic structure of the atmosphere and show inversion height and characteristics.

| Remote Sensor | Comments | Measurement (s) |
|---|---|---|
| 905 nm Ceilometer (NOAA ETL) | vertically pointing | Cloud-base height with time, reflectivities |
| Scanning Doppler Lidar (ESRL) | Stabilized and motion corrected, range ~ 5km, more details below | Aerosol backscatter, velocity |
| W-Band Doppler radar (UM) | 94 GHz (3.2 mm)- vertically pointing, unstabilized, only until Jan. 12th | High resolution Doppler spectra, cloud and precipitation microphysics and dynamics, reflectivity, velocity |
| Ka-Band Doppler cloud radar (NOAA ETL) | 35GHz (8.6 mm)- Scanning, dual-polarized, unstabilized but earth-referenced | Cloud microphysical properties, reflectivity, velocity |
| X-Band Doppler Radar (UM) | 9.4 GHz (3.2 cm)- vertically pointing, unstabilized | Cloud dynamics and precipitation physics, reflectivity, velocity |
| Wind Profiler (NOAA ETL) | 915 MHz (32.8 cm) | PBL 3-D winds, inversion height, clouds |
| Microwave Radiometer (NOAA ETL) | Laser diode, 2-channel (21 and 31 GHz ) “mailbox” | Integrated cloud liquid water and integrated total water vapor |

Table 2.1: A list of the remote sensing instruments onboard the R/V Seward Johnson during RICO.

The NOAA Earth Science Research Laboratory (ESRL) Doppler lidar (light detection and range) is the principal remote sensing observing system used in this analysis because of its ability to measure small-scale vertical velocity variations in the subcloud layer. The lidar is a master-oscillator, power-amplifier Doppler lidar with a line tunable wavelength between 9.2-11.3 μm, pulse length of 600 ns, low pulse energy (2 mJ) and a high pulse rate (up to 300 Hz, normally operated at 120 Hz). The instrument provides wideband signal to noise ratio (SNR) and line-of-sight velocity estimates (Brewer et. al 1998). For the vertical stare scans, the laser pulse width was shortened from 1 μs to 450 ns, resulting in improved vertical resolution. Data were averaged into 1 Hz temporally and 60 meter vertical gates spatially.

The lidar operates similarly to radars, however it utilizes lasers instead of a radio transmitter and it uses optics to direct and receive the laser beam. This lidar sends out a short pulse of light 270-280 times per second and each pulse lasts about 300 nanoseconds looking vertical or 1.2 nanoseconds looking horizontally within the atmosphere. The large difference in pulse length is due to the abundance of aerosol particles in the lower atmosphere, which causes the lidar signal to be attenuated faster when looking horizontally. The wavelength of the lidar is in the infrared range instead of the radio wave range, making it much more sensitive to small particles such as aerosols in the atmosphere. When the beam hits a particle, it is scattered in every direction, including back toward the source. Once the reflected beam returns to the receiver, the lidar compares the polarity and pulse frequency to that of the original beam. The difference between the two polarities directs the beam through a specific path to be recorded and measured. The difference between the frequencies provides information about the intensity and velocity of the particles as a function of range. If the lidar beam hits a cloud rather than just small aerosol particles, it is either absorbed or reflected and does not penetrate the cloud. Thus the lidar cannot sample the entire cloud, but it can determine velocities in clear sky conditions as well as small, shallow clouds that larger wavelength radars may miss (see comparison between X-band and lidar reflectivity, Fig. A1). The sensitivity of the lidar can be used to locate where small-scale features differ from the mean wind (i.e. turbulence). During RICO an integrated differential GPS navigation unit provided information for real time removal of ship’s motion from the velocity data.

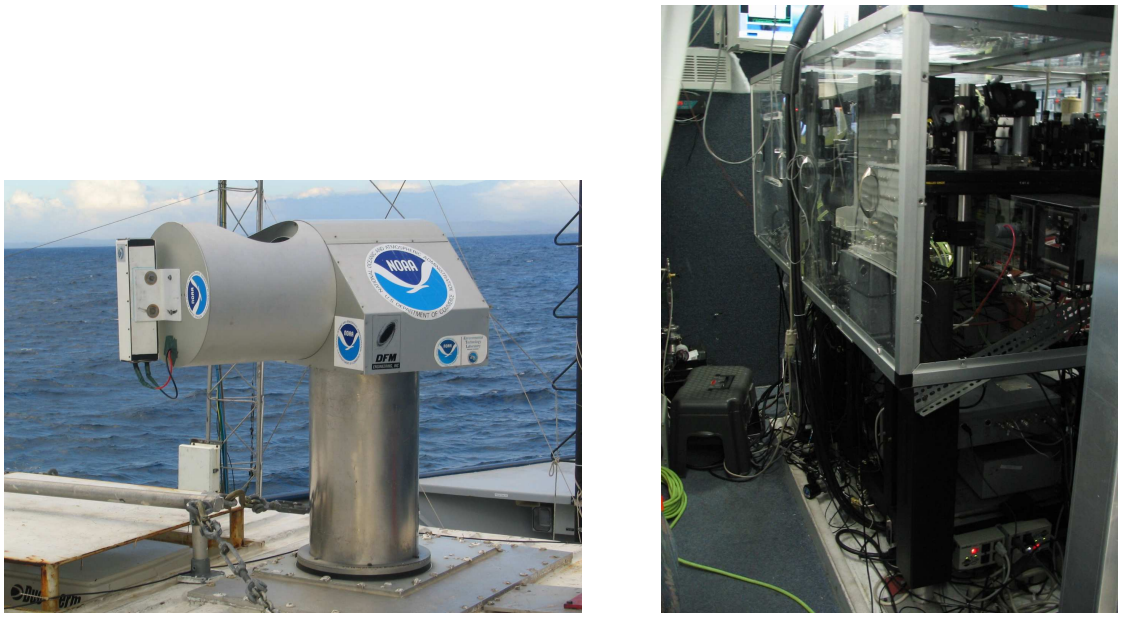

Figure 2.2: Photographs of the lidar during RICO. The left panel shows the receiver on top of the NOAA ESRL container. The right panel shows the hardware and optics inside of the container.

### 2.3 Data Availability and Processing

The first, rather technical challenge of this study was the acquisition, collection and quality control of the various data sets used in this study. The University of Miami Radar Meteorology Group (UMRMG) participated in the RICO 2005 experiment and was primarily responsible for the preparation of the deployment, data collection and preliminary processing of the X-band and W-band radars. We were also actively involved in the operation and data collection of some of the other instruments onboard the R/*V Seward Johnson*, as well as keeping an hourly log of weather conditions and cruise status. Our participation in the cruise provided us with immediate access to some of the RICO data, including GPS information, ceilometer, flux and rawindsonde data. The data from the lidar was generously provided by Dr. Sara Tucker and Dr. Alan Brewer, of NOAA

ESRL, who along with Dr. Janet Intrieri had the actual command of this instrument during the cruise.

A major issue affecting the quality of the Doppler lidar data is contamination due to ship motions. The majority of the time, the ship was heading into the winds, and thus we faced rough seas and significant pitching, rolling and yawing, which strongly impact any Doppler data collected, especially the velocity components and the direction that radar beams wound up pointing as the ship tipped. During RICO, the pointing angle of the Doppler lidar was compensated in real-time for ship motion using differential GPS sensors on all four edges of the lidar seatainer. Nevertheless, the lidar data were post-processed to remove ship-induced velocity components. Alan Brewer, Reginald Hill and Sara Tucker of NOAA ESRL have developed an algorithm (Hill et al. 2006) to remove residual velocity errors during the vertical stares that was applied to the entire lidar data set from RICO during post-processing.

During RICO, the Doppler lidar operated in several modes (PPI, RHI, sector, zenith, stare) (see Appendix, Fig. A2). In this study, I use the zenith (or vertically staring mode) data, which is extremely useful for calculating turbulence statistics during RICO, although this mode was only operated for the last 10-15 minutes of each hour that the lidar was operating. Since the lidar was located on the bow of the ship and experienced the roughest conditions and is a very sensitive machine, it was only operated for 8-12 hours per day as deemed most useful to the experiment, so on the best days there is only about 2.5 hours of combined vertical data, which limits a statistical analyses.

### 2.4 Technical Difficulties

One of the largest challenges for this study was the limited usefulness of the lidar above cloud base. While the lidar can see up to about 5 km in clear air, once the beam hits a cloud, any information collected above the cloud base is unusable. This is due to two factors. First, the lidar is extremely sensitive to cloud droplets and can saturate quickly, so when it detects even a shallow, thin cloud it will only see the lowest part of the cloud before the beam is saturated. To overcome this limitation, the original plan was to supplement the lidar subcloud data with W-band and X-band radar observations to provide vertical velocities in the cloud. Unfortunately, the W-band failed on January 12$^{th}$. Also, the ship motion was too drastic for either vertically pointing radar to remain constantly focused upward. Several suggestions for removing the ship motion in the X-band data set were proposed and attempted, but at this time none have proven to be valuable enough to make the data set useful to this study.

The second reason for the lidar data being unusable above cloud base is that a “chirp” or bend in the beam occurs when the beam hits the higher backscatter at cloud base. This chirp causes a positive bias to the velocity values in the next few gates. However, this bias is not constant and cannot be removed at this time. For these reasons, this study only focuses on the subcloud region of the boundary layer, an area in which the lidar can provide us with some new, higher-resolution information about the processes occurring.

One other small, but not inconsequential, difficulty was that the ceilometer was shut down on January 23$^{rd}$, which means that cloud fraction from the lidar could not be compared with ceilometer results on the 23$^{rd}$ or 24$^{th}$.

# Chapter 3- Boundary Layer Structure, Synoptic Conditions and Cloudiness

## 3.1 Introduction

In this chapter the temporal and spatial variability of the boundary layer and cloud properties during RICO are examined. Both directly-measured variables and Value Added Products (VAPs) are considered in this section and include: cloud base height and zenith fractional cloudiness from the ceilometer data set; potential temperature, mixing ratio, inversion strength and thickness, wind speed and direction from the soundings; radiative (solar and infrared) and turbulent (sensible and latent heat) fluxes, SST and surface air temperature from the flux tower and liquid water path from the microwave radiometer.

The synoptic conditions during RICO are classified into four periods of similar conditions and each of these periods is analyzed and classified by the major synoptic changes involved. For each observing period, the composite profiles and time series of cloud and boundary layer parameters are presented. Each synoptic period is highlighted and any prominent features are discussed. The diurnal cycle of some key cloud properties (e.g. fractional cloudiness) is also examined. All of this is done in an attempt to better comprehend the processes occurring in the boundary layer and how they might be related to observed variations in subcloud turbulence.

### 3.2 Boundary Layer Structure

Before we examine the trade wind boundary layer (TWBL) structure during RICO, we describe the idealized TWBL structure used in simple models (Fig. 3.1). The lowest layer is called the surface layer. The surface layer extends from the ocean surface up to about 1000 mb, so it is usually only about 100 meters thick. This layer generally has a super-adiabatic temperature gradient and a decrease of specific humidity with height that results in a slight static instability. The second layer is the mixed layer, a neutrally stratified region with an adiabatic temperature lapse rate and a nearly constant vertical specific humidity distribution that extends up to about 940 mb. The third layer, the transition layer, is not seen in every vertical profile, especially if a cloud is not present. It has a nearly isothermal temperature distribution and a strong decrease in moisture over its depth of about 100 m. The top of this layer usually coincides with the LCL of surface air parcels, forming the cloud base. Thus, the transition layer separates the cloud above from the dry convection and mixing regime occurring below. The transition layer is often averaged out when compositing of several profiles is done. The fourth layer is the cloud layer, which extends up to the base of the trade wind inversion (TWI). It is characterized by a temperature gradient slightly stronger than the moist adiabatic lapse rate and an upward weak decrease of specific humidity, which results in a conditionally unstable density distribution. This layer is cooled and moistened by convection. The fifth and final layer is the TWI itself, where there is a dramatic increase in temperature and decrease in specific humidity. The transition between the cloud layer and the inversion has a relatively small upward decrease in water vapor and little to no change in temperature.

Above the inversion, the free atmosphere is normally relatively warm and dry (Augstein 1974).

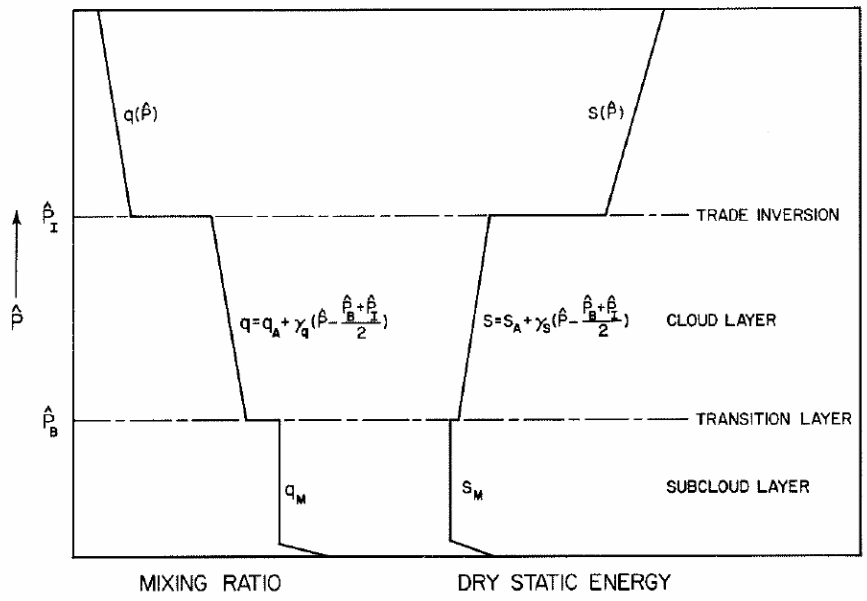


Figure 3.1: Idealized vertical profile of mixing ratio and dry static energy in the BL from Albrecht (1993).

### 3.3 RICO Synoptic Periods

At first look at several meteorological variables, such as cloud base height, moisture content and wind speed and direction, I observed a few striking shifts during different periods of RICO ship observations that all seemed to coincide in time. For example, Figure 3.2 shows the cloud base height from the ceilometer coupled with the LCL calculated from temperature and moisture measurements from the flux tower. Around January 20$^{th}$, the cloud base height increases significantly and remains at this height for the duration of the cruise. Since the LCL stays nicely coupled with the ceilometer during this increase, I believed that the change was caused by a larger synoptic-scale variation.

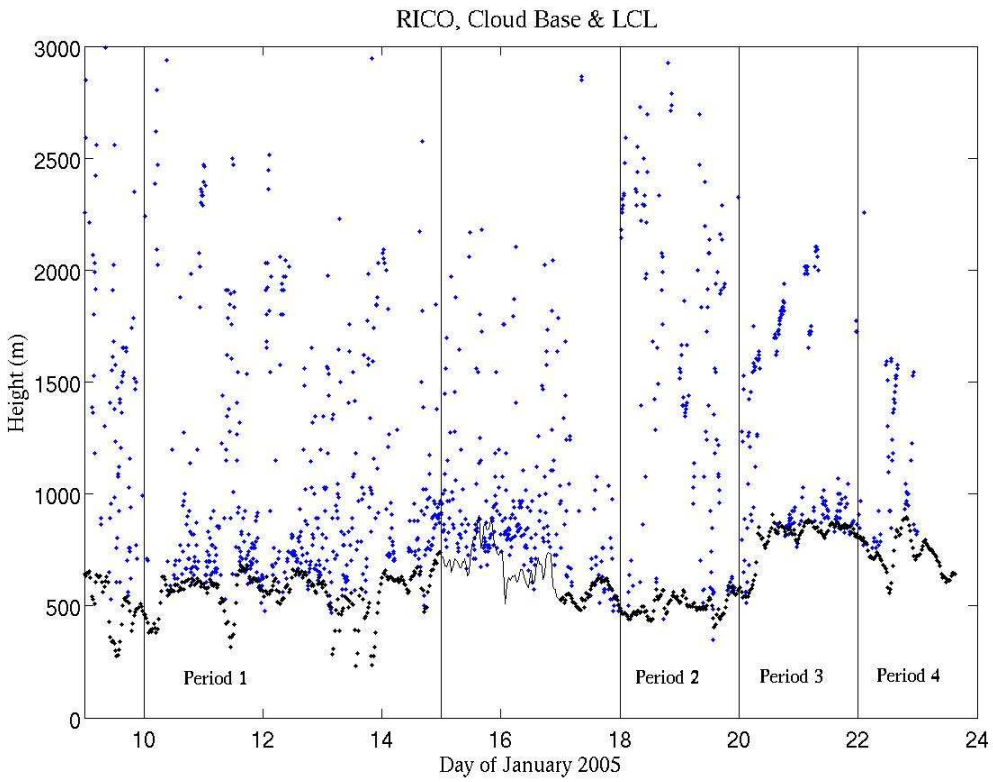


Figure 3.2: Cloud base height (blue dots) from ceilometer and LCL (black dots) from surface fluxes. The four synoptic periods are outlined.

Since synoptic conditions may affect the subcloud turbulence, the meteorological parameters and weather conditions over the entire cruise were classified into four periods identified in Fig. 3.2. Each period was analyzed in detail through NCEP Reanalysis (NCEP Reanalysis data provided by the NOAA/OAR/ESRL PSD, Boulder, Colorado, USA, from their Web site at http://www.cdc.noaa.gov/, some results are shown in Figs. 3.3-3.4) and the overall synoptic conditions influencing each period were categorized and are described below.

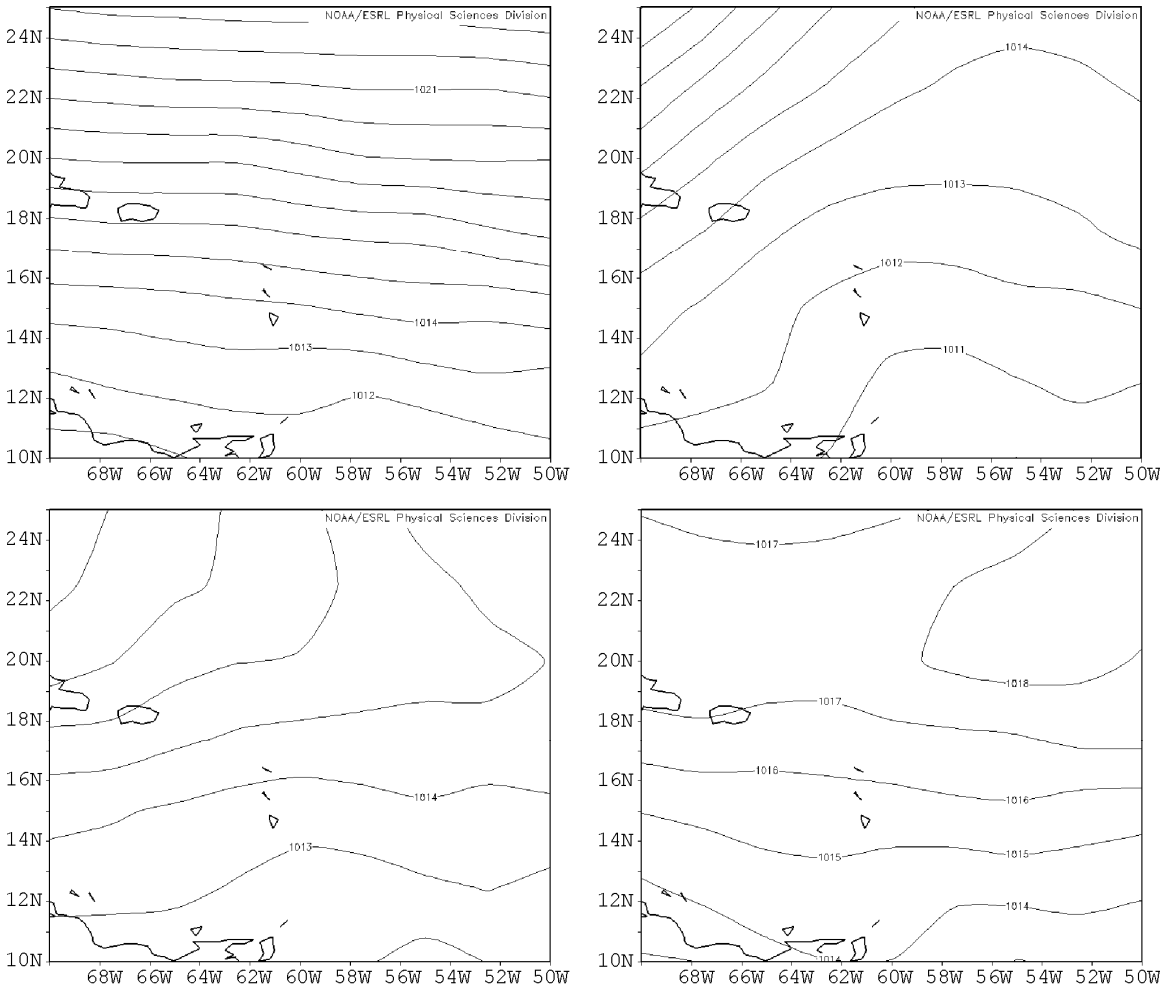


Figure 3.3: Sea Level Pressure Composites, mb: January 10-14, 2005 (upper left), January 18-20, 2005 (upper right), January 20-22, 2005 (lower left) and January 22-24, 2005 (lower right).

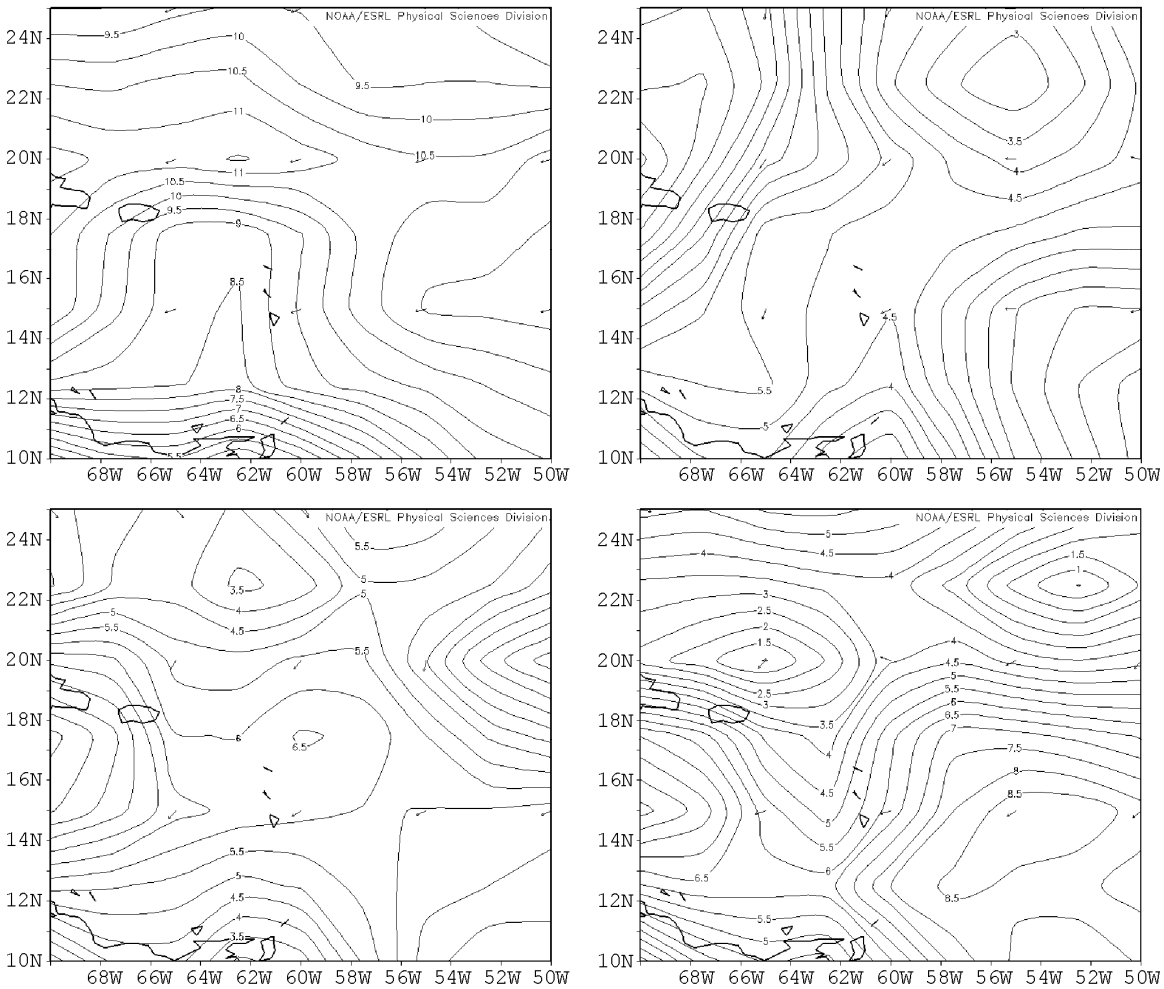


Figure 3.4: Surface Vector Wind Composite, m/s: Figure 1. Surface Zonal Wind Composite, m/s: January 10-14, 2005 (upper left), January 18-20, 2005 (upper right), January 20-22, 2005 (lower left) and January 22-24, 2005 (lower right).

**Period 1: January 10th-14th (hereafter referred to as SP1)**

Winds were strong and mostly zonal over the entire region, with the strongest easterly winds to the east of the islands. This period was very moist throughout the BL and experienced frequent rain showers with the passage of a surge line and a weak trough. Clouds were occasionally convective in nature, as seen by the heavy rainfall at times (Fig. 3.5). The most apparent variable separating this period from the others was the strong, constant easterly winds. A low level easterly wind maximum (LLEWM) occurred

on the 11th along with a line of convection. Above 500mb, northwest winds advected dry air into the higher levels (Ceaser 2005).

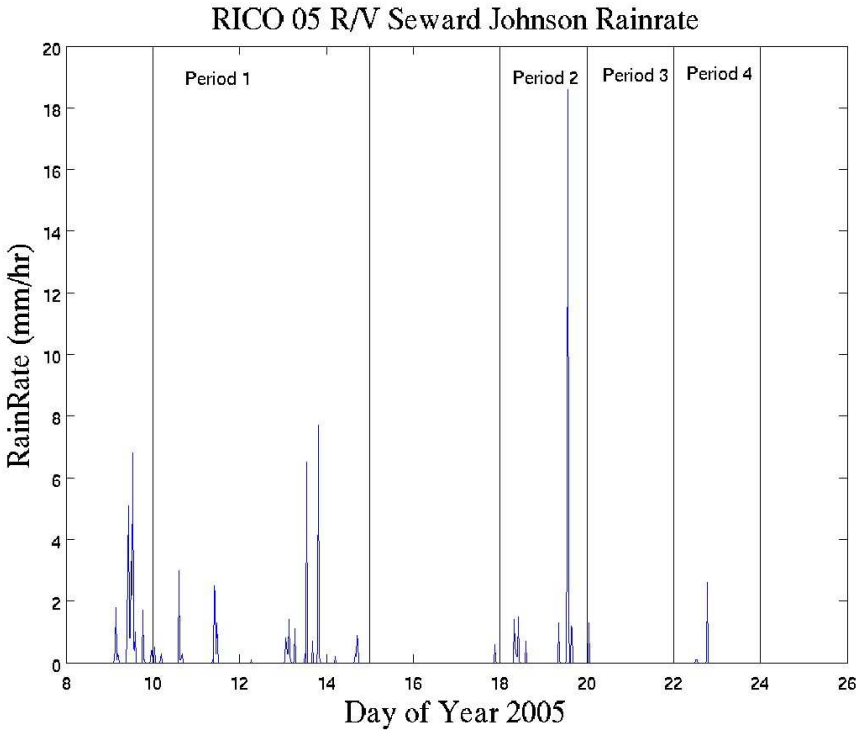


Figure 3.5: Time mapping of rainrate from the flux tower during RICO.

It is important to note that the gap between SP1 and Period 2 is due to a port call in Antigua on January 15th. On the 16thand 17th, the ship ventured back out into the Atlantic, but wind conditions were so extreme, that it had to take cover downwind of Barbuda for a large portion of the day and night. The lidar data sets from January 16th and 17th will be analyzed but will not be used in a Synoptic Period to avoid any data corruption induced by the island.

**Period 2: January 18th-20th (hereafter referred to as SP2)**

This was a period of transition between the unsettled conditions of SP1 and the more "typical" trade wind conditions of SP3. On January 18th, a strong cold front approached from the NW, but as it came closer to the region it became more of a shear line. This increased low level moisture and instability and caused clouds to thicken into bellowing cumulus or overcast stratocumulus. Very dry air aloft limited any significant convective development (Fig. 3.6). When looking at the overall vector winds (Fig. 3.4) it can be seen that winds were still easterly to the east of the islands, but took on a northeasterly component to the west of the islands. Wind speed decreased in magnitude significantly from SP1 (Fig. 3.7). Sea level pressure lowered with the approach of the shear line, and there were many rain showers from 18th-20th.

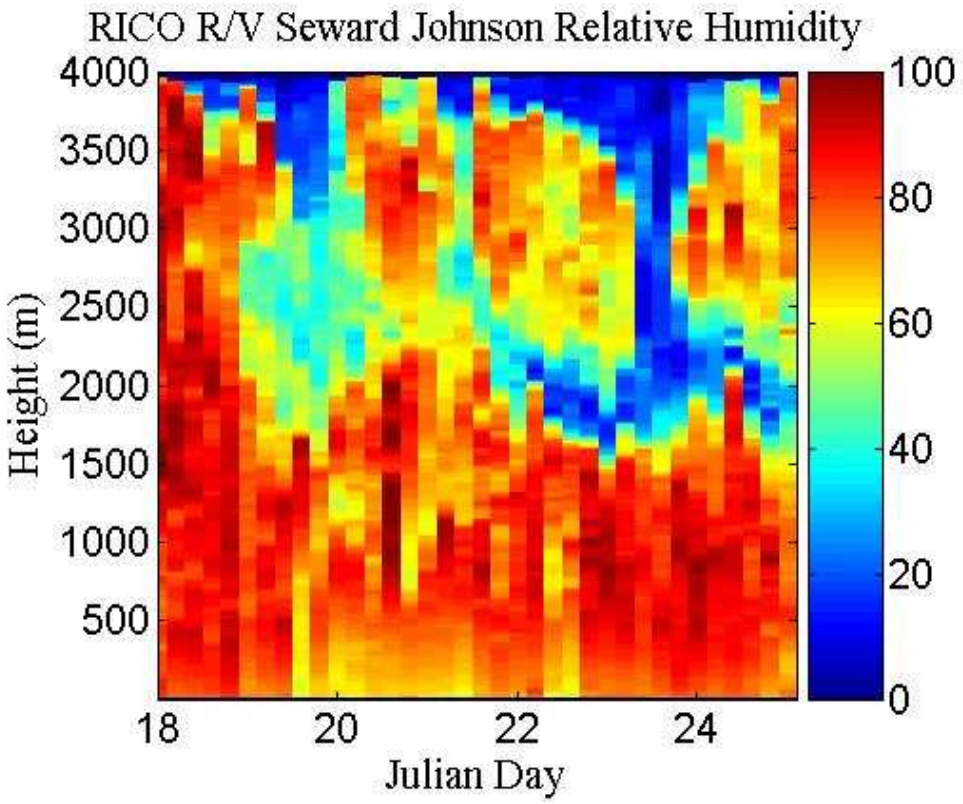


Figure 3.6: Time-height mapping of relative humidity (%) for January 18th-24th from soundings launched during RICO.

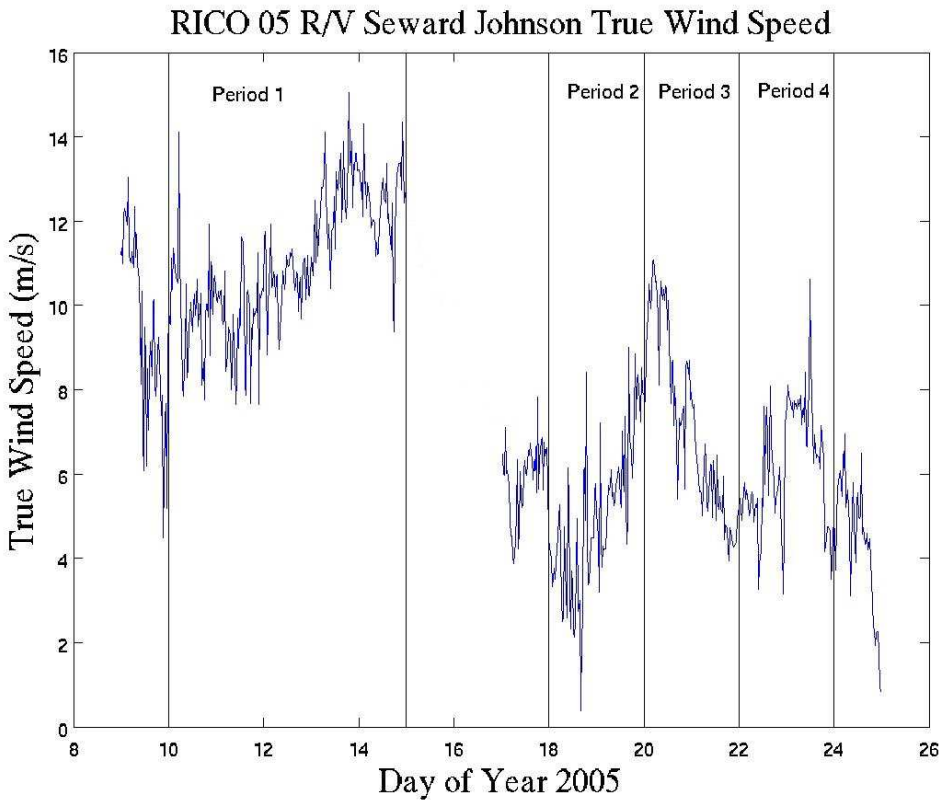


Figure 3.7: Surface true wind speeds taken from the flux tower (14 m) during RICO 2005. The jump in data is due to a port call in Antigua on January 15th-16th, so that data is not included in the set.

**Period 3: January 20th-22nd (hereafter referred to as SP3)**

The shear line passed over the region on the 20th with increased clouds but very little shower activity due to strong subsidence aloft and the lack of low-level moisture. Westerly winds lowered to 700 mb and the trade wind inversion fell below freezing level for the remainder of the experiment, providing a very stable environment. During this period, we saw the most "typical" trade wind conditions- namely light to moderate easterly winds and very little convection or precipitation. Overall, the wind direction remained from the NE. High pressure built in from the NW; clouds were very small and shallow and there was no measurable rainfall (Fig. 3.5). The most striking change during

this period was the drying of the air aloft, which will be shown in further detail in section 3.4.1.

**Period 4: January 22nd-24th (hereafter referred to as SP4)**

This period is very similar to SP3 as cloud bases continued to be high and the winds remained light over the islands. Strong inversions existed at 850 mb and 670 mb and maintained stable conditions. The vector wind composite (Fig. 3.4) shows the wind direction has gained more of an easterly component back again. The high pressure system has passed to east, keeping the conditions mostly suppressed, with only one light rainfall occurrence. However, this period cannot be classified as part of SP3 due to increasing temperatures, humidity (Fig. 3.8), and cloud activity.

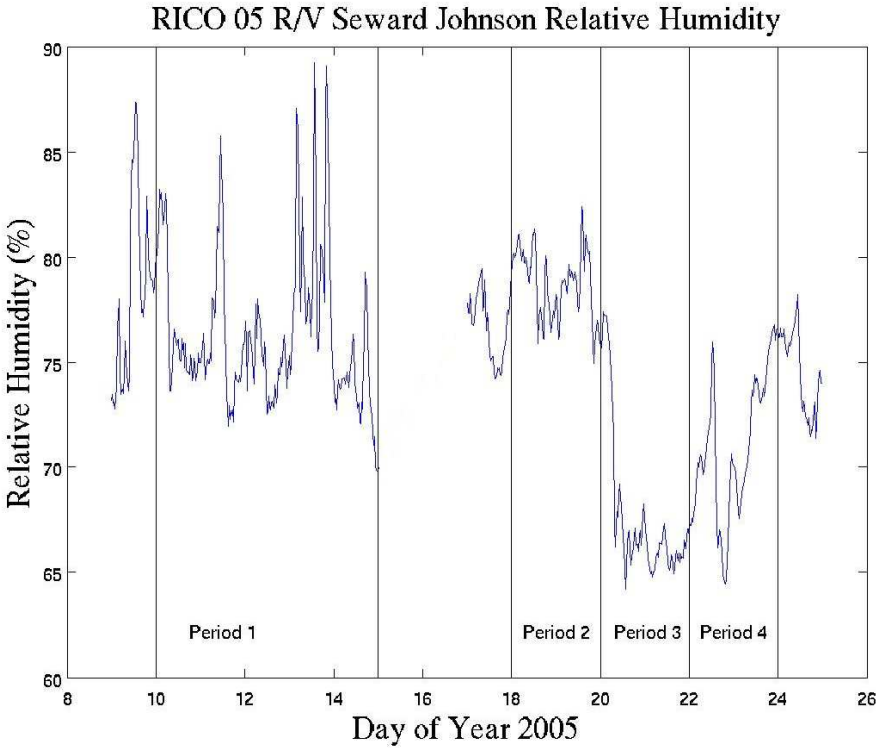


Figure 3.8: Surface relative humidity from the flux tower. The jump in data is due to a port call in Antigua on January 15th-16th, so that data is not included in the set.

### 3.4 Cruise-Composite Mapping of Meteorological Variables

As seen from the four synoptic periods above, a wide range of moisture and cloud conditions were encountered during RICO. Cruise-composite mappings of rawinsonde and flux tower variables can help us to gain a detailed understanding of how these properties change over the course of the experiment.

A typical single sounding from RICO is shown in Fig. 3.9. The different layers of the BL are visible from this figure, especially the mixed layer, transition layer, cloud layer, and TWI, though they are not nearly as well defined as the idealized case shown in Fig. 3.1. While this type of single profile is very detailed and provides valuable height profiles of many variables, for the sake of our analysis, it is more useful to look at these variables averaged by regime as done in Figs. 3.11, 3.13 and 3.14, or at cruise composites of all the soundings, as done in Figs. 3.10 and 3.12.

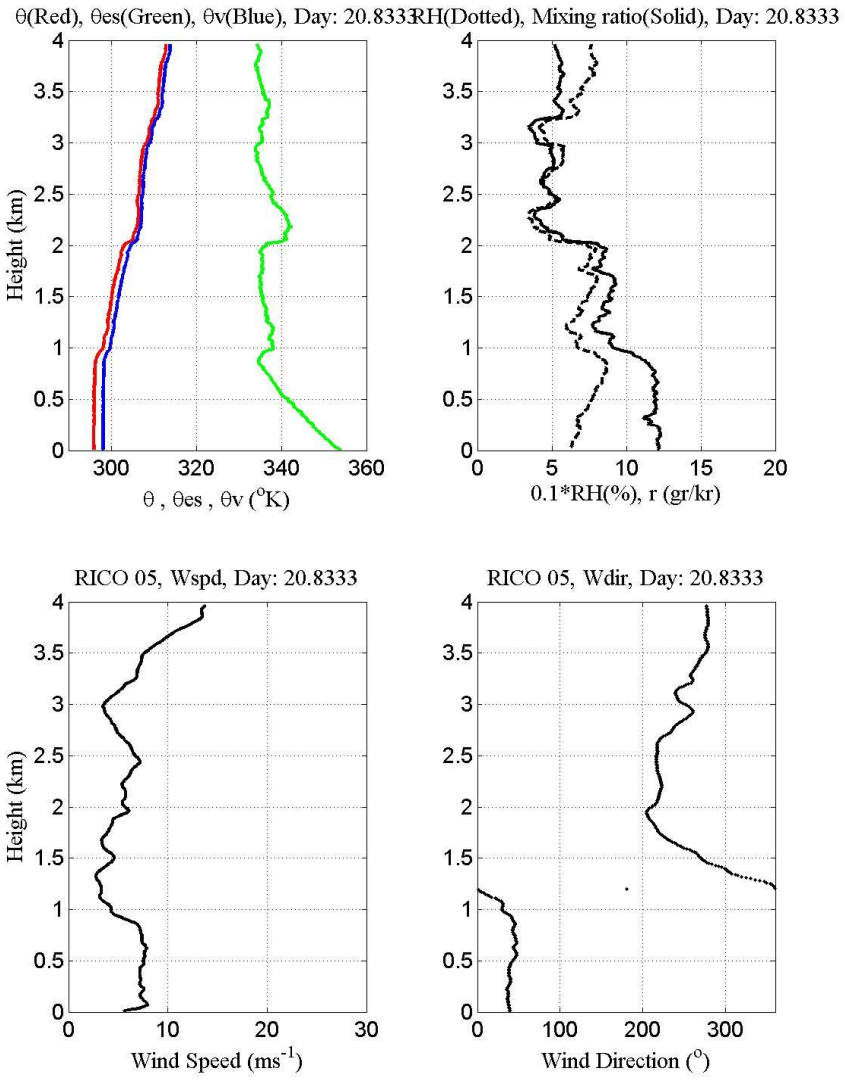


Figure 3.9: Sample sounding from RICO, released on January 20, 2005.

### 3.4.1 Moisture and Potential Temperature Structure

The marine atmospheric boundary layer (MABL) mixing ratio structures from rawinsondes launched during RICO are shown in Fig. 3.10. The LCL (calculated from surface fluxes) is also shown. One of the goals of this study is to identify the synoptic and

MABL changes and relate them to lidar turbulence statistics and this figure illustrates a striking change in the structure during RICO. During SP1 and SP2, the subcloud layer is very moist and well mixed, with the remainder of the BL being evenly stratified from very moist at cloud base to slightly dry aloft (about 4 km). A shift to drier conditions is seen during SP3, after the passage of the shear line, as the entire region below 4 km dries by about 2 g/kg. This is accompanied by an increase in the LCL by about 300 meters. The overall profile during SP3 is still stratified. SP4 shows a re-moistening below cloud base, but a further intrusion of dry air from 2 km-4 km, increasing the moisture gradient around 1.75 km. The LCL still remains higher than SP1 or SP2, but has decreased in height slowly during SP4. The LCL and moisture content were strongly coupled during the entire cruise.

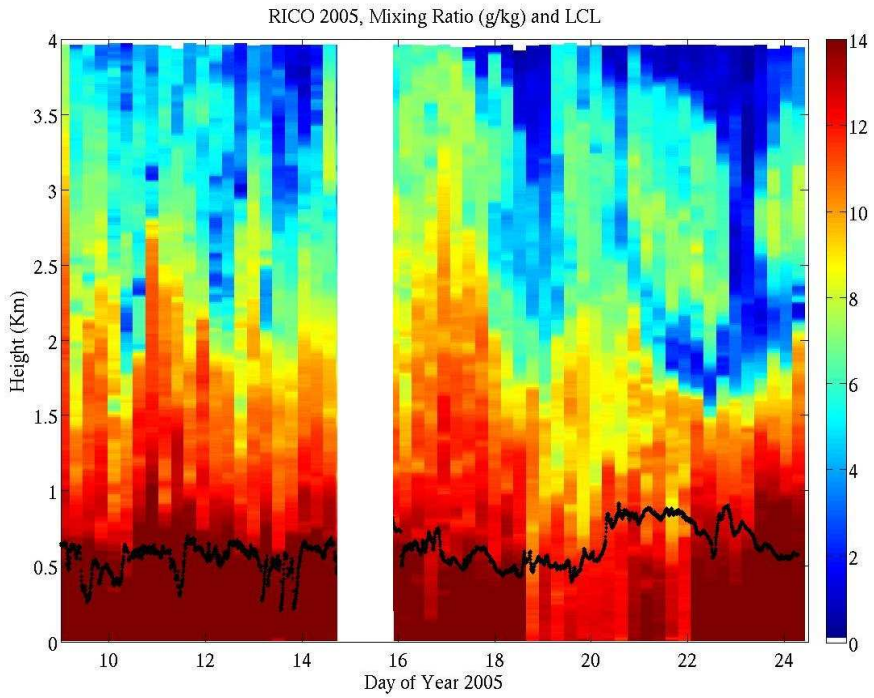


Figure 3.10: Time-height mapping of mixing ratio r (g/kg) from soundings launched during RICO. The LCL (black dots) is calculated from surface fluxes. White space indicates missing soundings during interlude between the two legs of the experiment.

Another view of the moisture structure in the BL can be seen by averaging the soundings in each synoptic period, as done in Fig. 3.11. From this figure, the similarities in the moisture structure between SP1 and SP2 are obvious, as well as the decrease in moisture by 2-3 g/kg during SP3. SP4 shows a rebound in moisture content at the surface, but still lower values near the LCL. The pool of drier air seen in blue during the later days of Fig. 3.10 is also visible on this image as a decrease in mixing ratio around 2 km during SP4. When averaging the soundings over a few days, the various layers of the BL tend to be blurred, but this kind of analysis is crucial for understanding the variations between various time intervals during RICO so that I can determine if any shifts in lidar turbulence statistics can be related to synoptic scale influences.

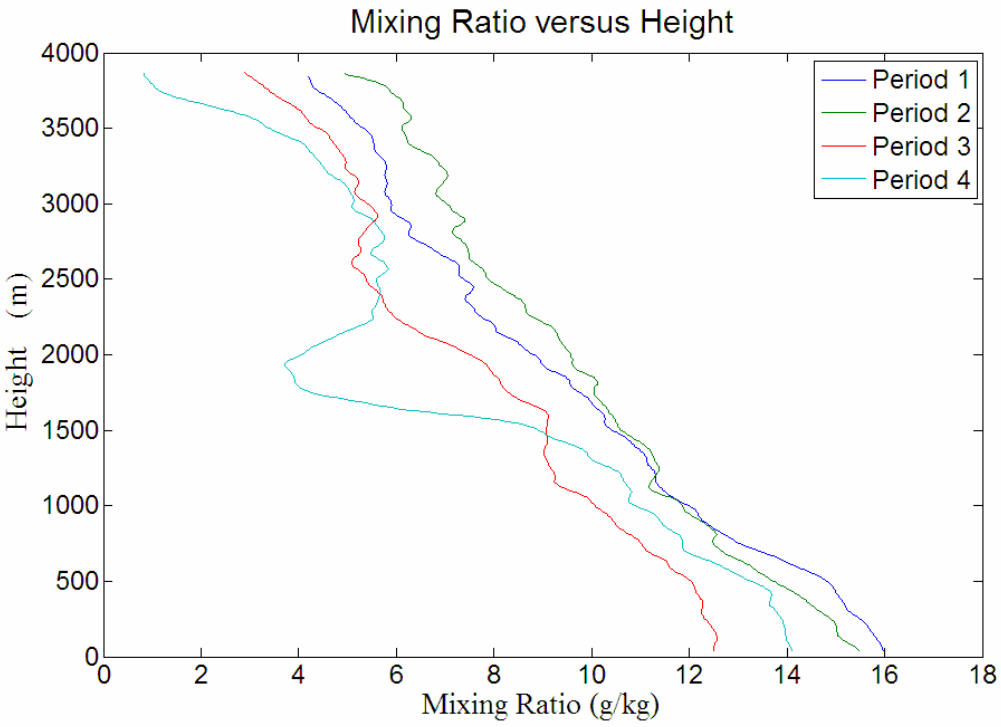


Figure 3.11: Average mixing ratio with height during each of the 4 Synoptic Periods.

The evolution of potential temperature (θ, in Kelvin) throughout the lowest 4 km of the boundary layer is shown in Fig. 3.12. As expected for this subtropical location, the

temperature profile is very uniform throughout the 3 week period. The boundary layer inversion is nicely defined, and its evolution with time is clear. Around January 21st-22nd, θ decreases a few degrees K at a height of 1.5-2 km as compared with the rest of the cruise. This is most likely related to the increase in cloud base height and TWI height during SP3 and SP4. You can see the beginning of the higher values of θ starting to take over at that height again in the last sounding of this plot, which coincides with the lowering of cloud base and LCL as seen in Fig. 3.2. Overall, there is a very uniformly stratified, gradual increase of potential temperature from around 298 K at the surface to 315 K around a height of 3.5 km.

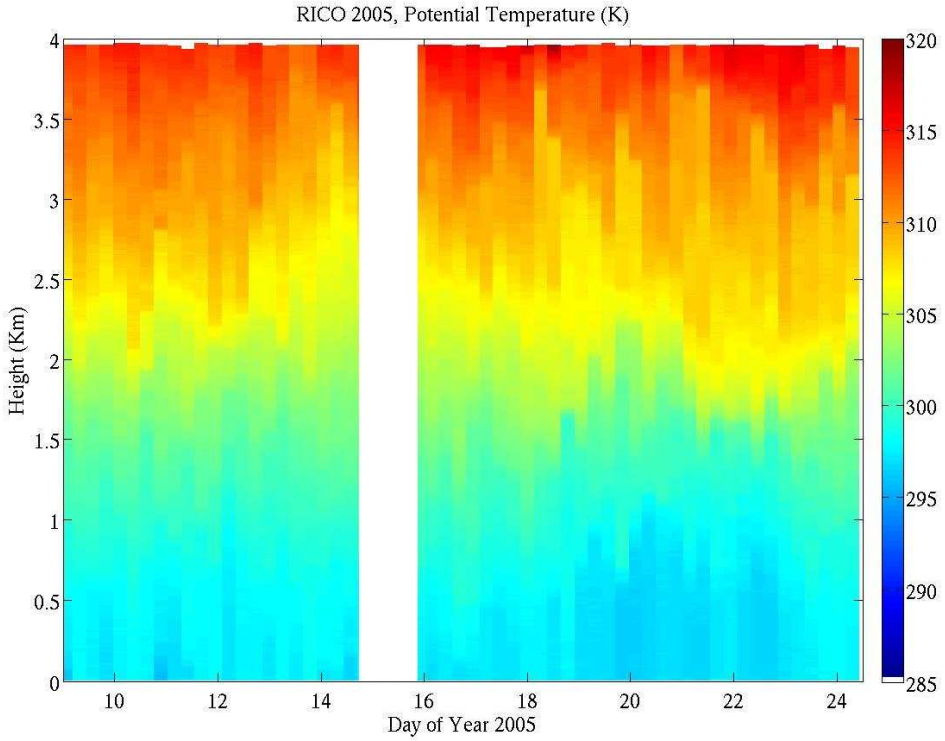


Figure 3.12: Time-height mapping of potential temperature (K) from soundings launched during RICO. White space indicates missing soundings.

The average profiles of potential temperature by synoptic period are shown in Fig. 3.13. This figure illustrates the higher values of θ in SP1 and SP2 in the entire subcloud layer. Above the inversion, SP1, SP2 and SP3 all have very close values, but SP4 increases by about 5 K between 1500 m and 2500 m. This is representative of some warm air advection occurring above the inversion during the final days of the experiment and is related to the pool of drier air seen in blue at the end of Fig. 3.10.

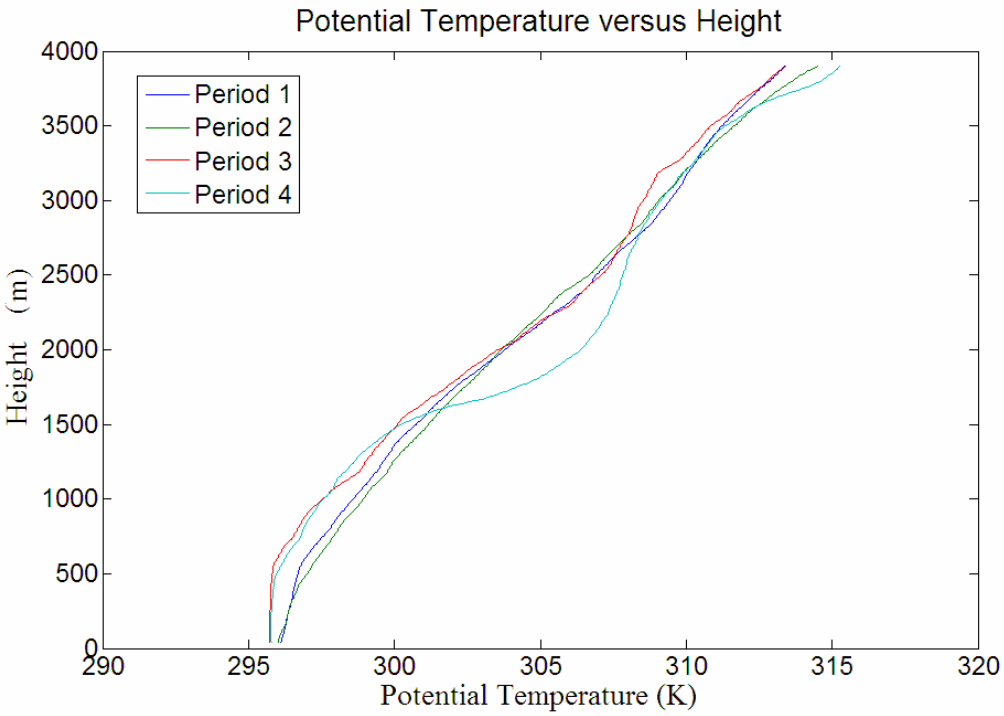


Figure 3.13: Average θ (K) with height during each of the 4 Synoptic Periods.

The static stability associated with each of the composite soundings was evaluated using plots of equivalent potential temperature ($\theta_e$) vs. saturation equivalent potential temperature ($\theta_{es}$) averaged from all of the soundings made during each synoptic period. Fig. 3.14a shows $\theta_e$ in blue vs. $\theta_{es}$ in green for SP1. The inversion is visible in $\theta_{es}$ around 2 km. The amount of CAPE, or convective available potential energy, can be estimated by comparing the near surface value of $\theta_e$ (which is conserved with height, shown as

dashed red line) with $\theta_{es}$. Above the LCL up to the Equilibrium Level (EL) the difference between the surface $\theta_e$ and $\theta_{es}$ can be related to CAPE. The larger the CAPE, the more likely that convective conditions will occur. The composite sounding from SP1 has the most CAPE out of all four periods, which is expected given the highly convective conditions that were experienced during this time period.

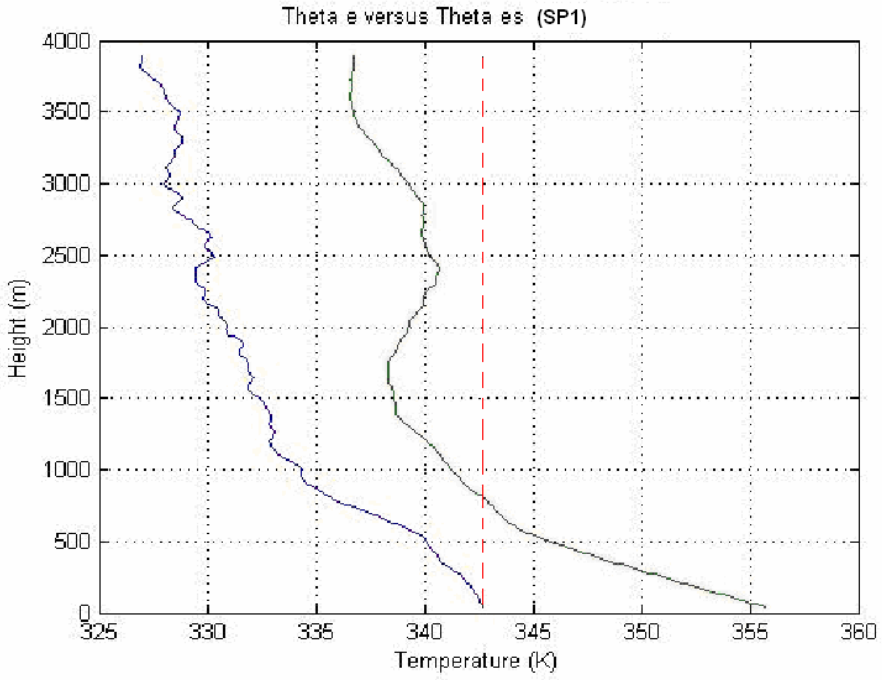


Figure 3.14a: Composite of soundings during SP1 (January 10th-14th). $\theta_e$ is shown in blue and $\theta_{es}$ is shown in green. Dashed red line shows surface $\theta_e$ conserved with height.

Fig. 3.14b is the same as Fig. 3.14a, but for SP2. The inversion is not readily visible in this figure, most likely because this was a period of transitioning conditions. There is only a very slight inversion in $\theta_{es}$ around 2.5 km. The atmosphere is still very moist throughout the BL. There is still a considerable amount of CAPE, but not as much as seen during SP1.

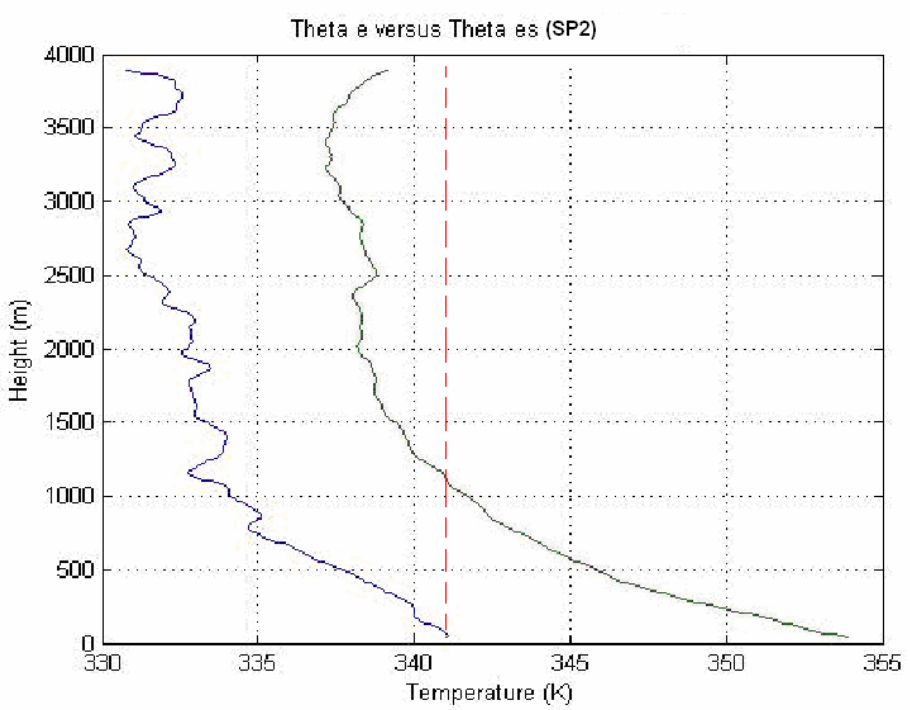


Figure 3.14b: Composite of soundings duringSP2 (January 18th-20th). $\theta_e$ is shown in blue and $\theta_{es}$ is shown in green. Dashed red line shows surface $\theta_e$ conserved with height.

Fig. 3.14c shows the composite sounding for SP3. Here the drastic change in BL conditions is clearly seen. The inversion is visible in both $\theta_e$ and $\theta_{es}$ around 2-2.5 km. The level of surface moisture has decreased, causing the entire BL to be drier, especially the inversion layer. The decreased moisture also limits CAPE, giving us suppressed, standard trade wind conditions.

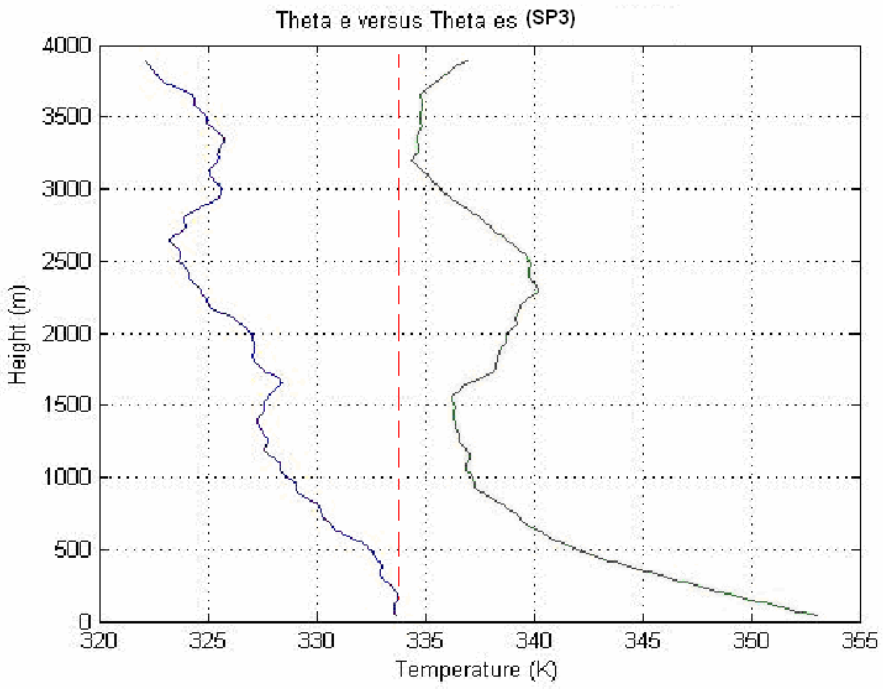


Figure 3.14c: Composite of soundings during SP3 (January 20th-22nd). $\theta_e$ is shown in blue and $\theta_{es}$ is shown in green. Dashed red line shows surface $\theta_e$ conserved with height.

The composite $\theta_e$,$\theta_{es}$ profiles for SP4 are shown in Fig. 3.14d. The inversion is even more visible in both $\theta_e$ and $\theta_{es}$ around 2 km then it is in the previous figure. The surface moisture remains lower than in SP1 and SP2, and while the subcloud layer has moistened slightly, the inversion layer is even drier than during SP3. Figs. 14a-14d help to further our understanding of the BL conditions during each Synoptic Period, and the distinction between the "convective" SP1 and SP2 and the "typical trade wind" SP3 and SP4 is clearly defined by these results.

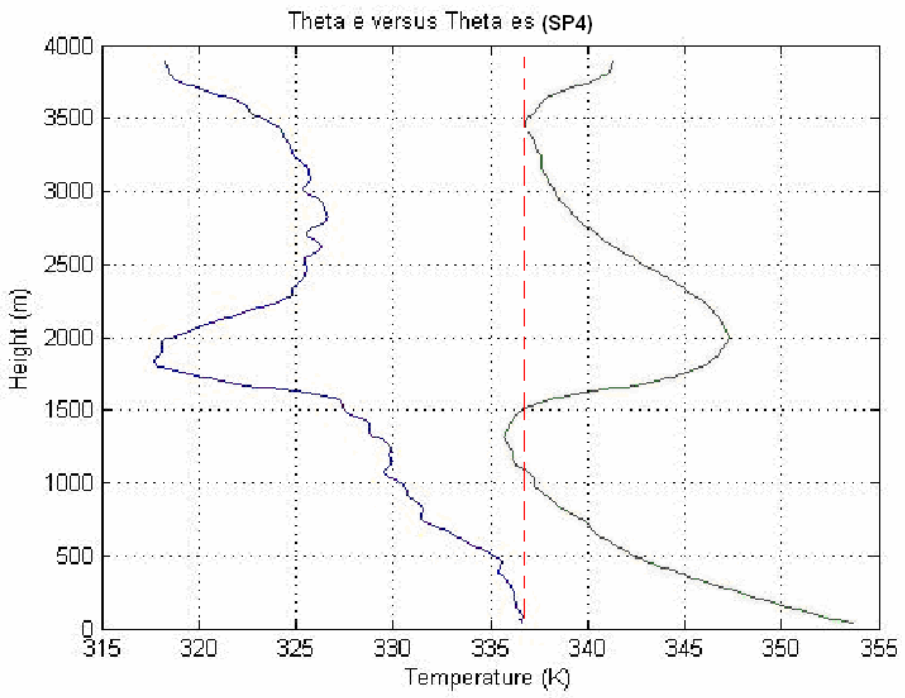


Figure 3.14d: Composite of soundings during SP4 (January 22nd-24th). $\theta_e$ is shown in blue and $\theta_{es}$ is shown in green. Dashed red line shows surface $\theta_e$ conserved with height.

### 3.4.2 Air Temperature and SST Profiles

The surface and near surface temperature, moisture and wind conditions are defined for the entire cruise using observations from the flux tower and a sea snake. Fig. 3.15 shows the evolution of air temperature ($T_{air}$) and the sea sea surface temperature (SST) from the sea snake, located at 0.5 meters below sea surface. As expected, the SST remained warmer than $T_{air}$ throughout the experiment, probably due to cold advection moving cooler air over the surface. The diurnal variation for $T_{air}$ is about 2-2.5 degrees. The diurnal variation in SST is also visible in this figure, although it is only about 0.5 degrees and is less pronounced during SP3 and SP4. Overall, the SSTs over the course of the cruise do not change drastically except for a dip on January 18th, which is may be due

to cool rainwater on the ocean surface or crossing a cold pool of water was the ship emerged from behind Barbuda. As for $T_{air}$, there is a fundamental difference in daily high temperature between SP1 (Leg 1 of the cruise) and SP2 and SP3, despite the ship being located over relatively the same latitude during these time periods. The surface air temperature is only about 1 degree cooler during the later periods, but it is a consistent decrease and is probably due to the passage of the cold-front-turned-weak-shear-line. $T_{air}$ begins a gradually warm-up during SP4, and by January 25$^{th}$, daily high temperatures have returned to what they were during SP1.

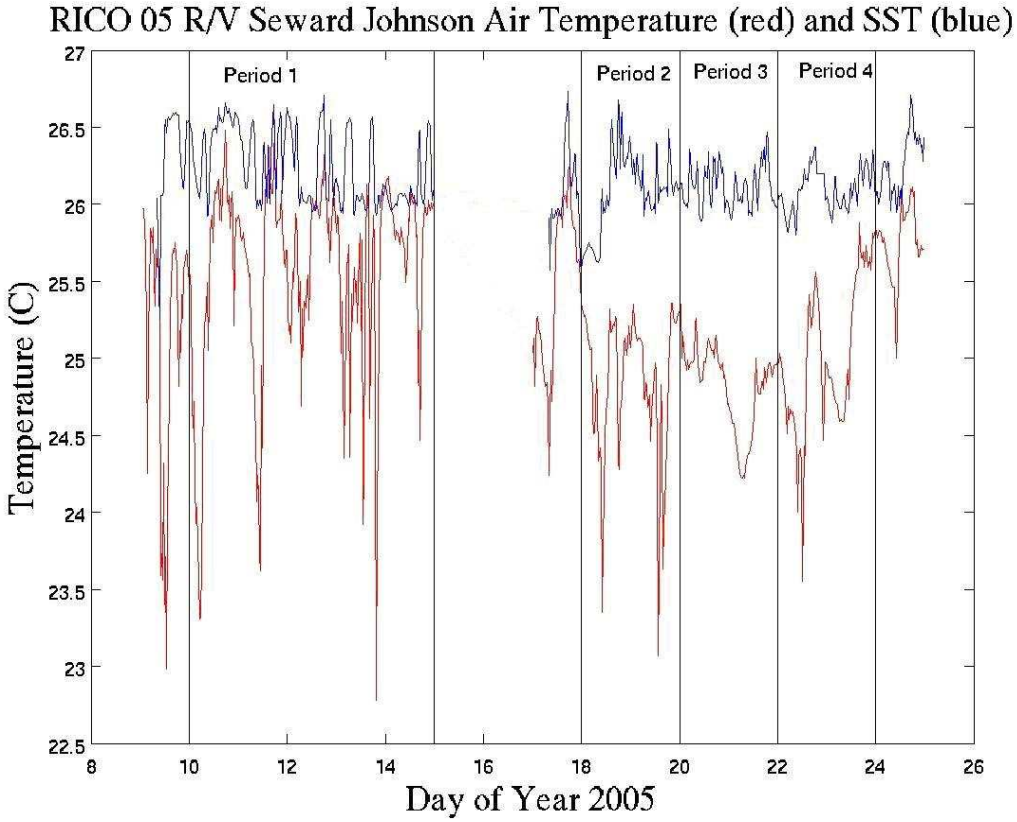


Figure 3.15: Time evolution of Surface Air Temperature ($T_{air}$, red) and SST (blue) during RICO 2005 in degrees C. The jump between January 15$^{th}$-17$^{th}$ is missing observations due to the interlude between the two legs of the experiment.

### 3.4.3 Wind Speed and Direction

The winds observed from the ship are examined using time-height mappings made from the soundings. The wind speed is shown in Fig. 3.16, and the most striking feature in this figure is the area of high the wind speeds observed during the first leg of the cruise (January 9$^{th}$-14$^{th}$). During this time, wind speeds of 13-20 m/s are found throughout the first 2 km of the BL. Above this height, the winds are reduced to 2-5 m/s, except from January 12$^{th}$-14$^{th}$, when the high winds are present up to 3.5 km. During Leg 2 (January 16$^{th}$-24$^{th}$) of the cruise, there is a decrease in wind speeds from the surface to 2.5 km. In this time frame, the highest wind speed throughout the BL is only 10 m/s. There is an interesting feature of higher wind speeds from 3-4 km on January 20$^{th}$-24$^{th}$, which is actually related to the return of stronger westerlies aloft, which have lowered in height down to 5 km (Caesar 2005).

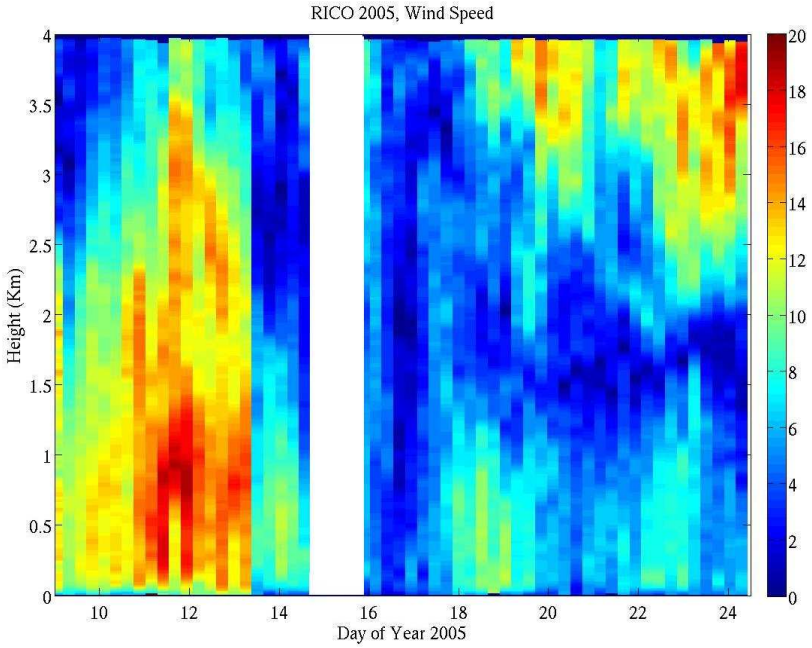


Figure 3.16: Time-height mapping of wind speeds (m/s) from sounding launched during RICO. White spaces indicate missing or bad data.

To get a detailed view of the wind speeds during each Synoptic Period, Fig. 3.7 presents the time trace of surface wind speeds from the flux tower (at 14 m). These show the drastic decrease in wind speeds between SP1 and the later 3 periods. The wind speeds that occurred from January 17$^{th}$-24$^{th}$ are much more typical of the winter trade wind regime and will provide a nice comparison of "standard" turbulence conditions vs. the convective conditions seen during SP1 later on in this thesis.

Winds in the tropical trades are usually easterly at lower levels and westerly above the TWI. During the winter months, weaker easterly winds are observed at the surface compared with those during the summer months. The time-height mapping of wind direction taken from the soundings during RICO is shown in Fig. 3.17. During Leg 1, easterly winds are present from the surface up to 4 km, except for a small area of southwesterly winds around 3.5 km on January 10$^{th}$. During Leg 2 easterly winds only extend from the surface up to about 1.5 km during the majority of this period. Above this level the wind direction ranges from SW to NW up to 4 km. This is that intrusion of drier air seen in Fig. 3.10 and corresponds to the stronger wind speeds seen aloft in Fig. 3.16.

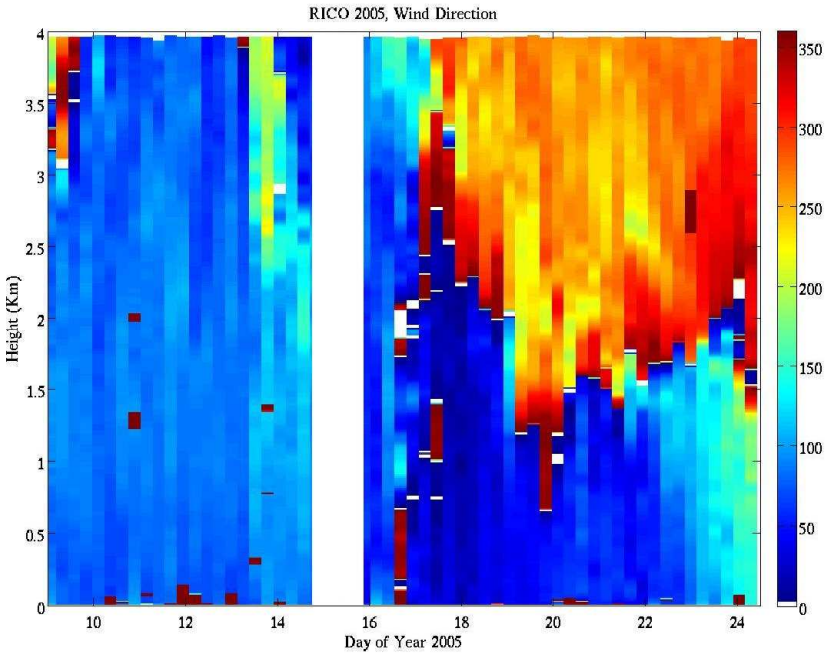


Figure 3.17: Time-height mapping of wind direction (0 is due north) from sounding launched during RICO. White spaces indicate missing or bad data.

### 3.4.4 Radiative and Turbulent Fluxes

Surface radiative and turbulent fluxes are typically among the main variables that influence the vertical structure of the TWBL. They are closely tied to the amount of cloud cover and thus the amount of precipitation produced by these clouds. Time series of both incoming solar and IR fluxes from the flux tower are shown in Fig. 3.18. Both incoming shortwave and longwave radiation demonstrate a rather expected variability throughout each cruise, as they are primarily modulated by fractional cloudiness. During periods with mostly cloudy skies, the IR fluxes are higher, ranging from 400 to 430 W/m$^2$ while the maximum (noontime) solar fluxes are lower, and range between 400 and 700 W/m$^2$. Clear-sky periods are associated with reduced incoming longwave radiation, ranging from 370-390 W/m$^2$, and higher noontime solar fluxes (700-800 W/m$^2$). These fluxes are

5-minute averaged, so since we did not encounter any days of 100% overcast conditions, it is understandable that there is not a large variation between maximum incoming solar radiation even on days with higher fractional cloud cover, because quite a bit of solar radiation made it through clear-sky sections on all days. This span of values for both longwave and shortwave radiation provides a rough estimate of the intensity of the radiative forcing associated with the Atlantic FWC Regime, and highlights the importance of an accurate representation of these clouds in the radiative transfer schemes of regional and global climate models.

The surface turbulent fluxes calculated from the tower turbulence measurements are shown in Fig. 3.19. The sensible heat (SH) and latent heat (LH) fluxes are primarily modulated by winds and the sea-air temperature difference variations. The sensible heat flux is tied to SST-$T_{air}$. Latent heat fluxes exhibit much higher values (in $W/m^2$) than the SH fluxes in general, which is expected over the warm ocean. The convective velocity scale w* (Eq. 3.1, also known as the Deardorff velocity) is shown in the lower panel of this figure. The velocity scale is given as:

$$w^* = [g\overline{T}^{-1}\overline{(w'T_v')}_0 h]^{1/3} \quad \text{(Eq. 3.1)}$$

where g is gravity, T is surface temperature, $(w'Tv')_o$ is the virtual heat flux at the surface and h is subcloud layer depth (assumed to be cloudbase height).

This variable is related to buoyancy production of turbulence in the boundary layer and is a useful scaling parameter for convective boundary layers. It is closely tied to both the SH and LH fluxes, since under ocean conditions the LH contributions to the virtual flux can be important. During the convective conditions of Leg 1, w* is more closely tied to SH, but during the more “trade wind” conditions of Leg 2, it is equally modulated by

both turbulent fluxes. The values of our calculated w* range from 0-1 m/s, with a cruise average of 0.48 m/s, which is similar to the average w* values of 0.54 m/s found by Nicholls and LeMone (1980) during GATE for FWC conditions. The two peaks seen around January 15th and 16th are due to the ship being stationed in port in Antigua and behind Barbuda and those days are ignored in this analysis. Table A1 in the Appendix shows a list of the mean w* during each day of RICO, values that will be used to scale lidar velocities later in this thesis.

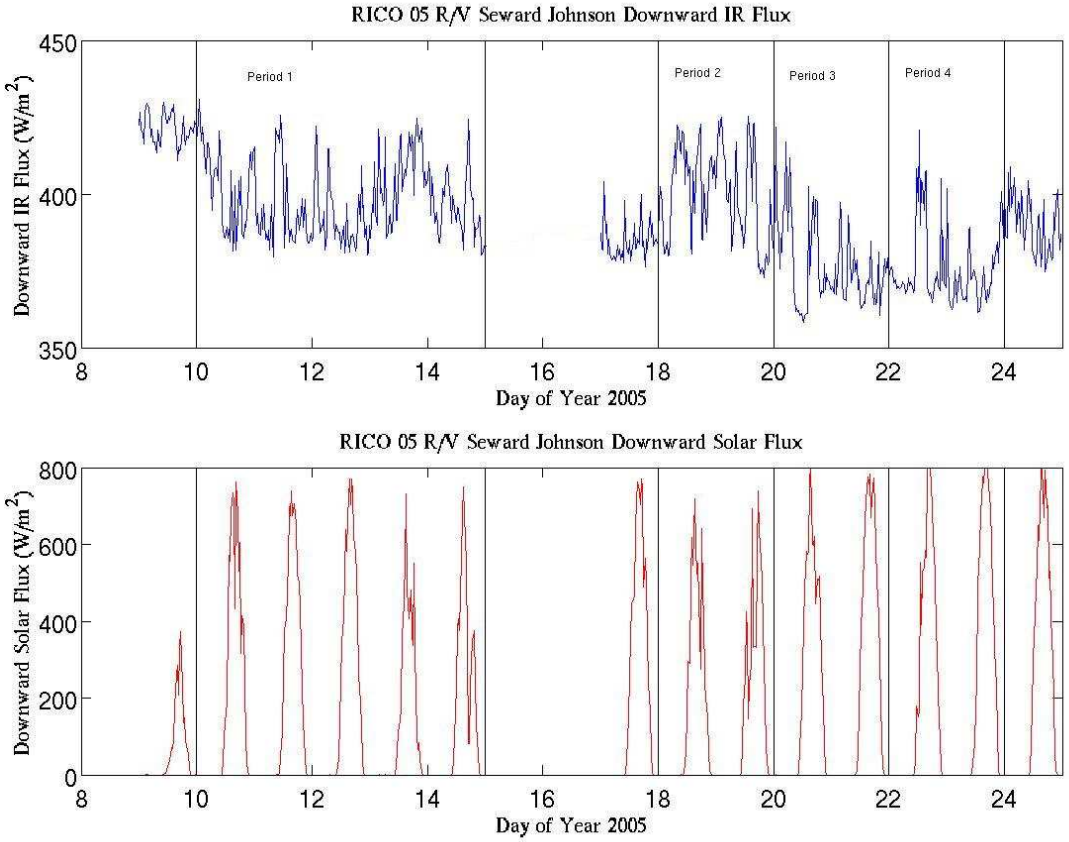


Figure 3.18: Time mapping of Incoming IR Flux (blue) and Incoming Solar Flux (red) from the flux tower during RICO.

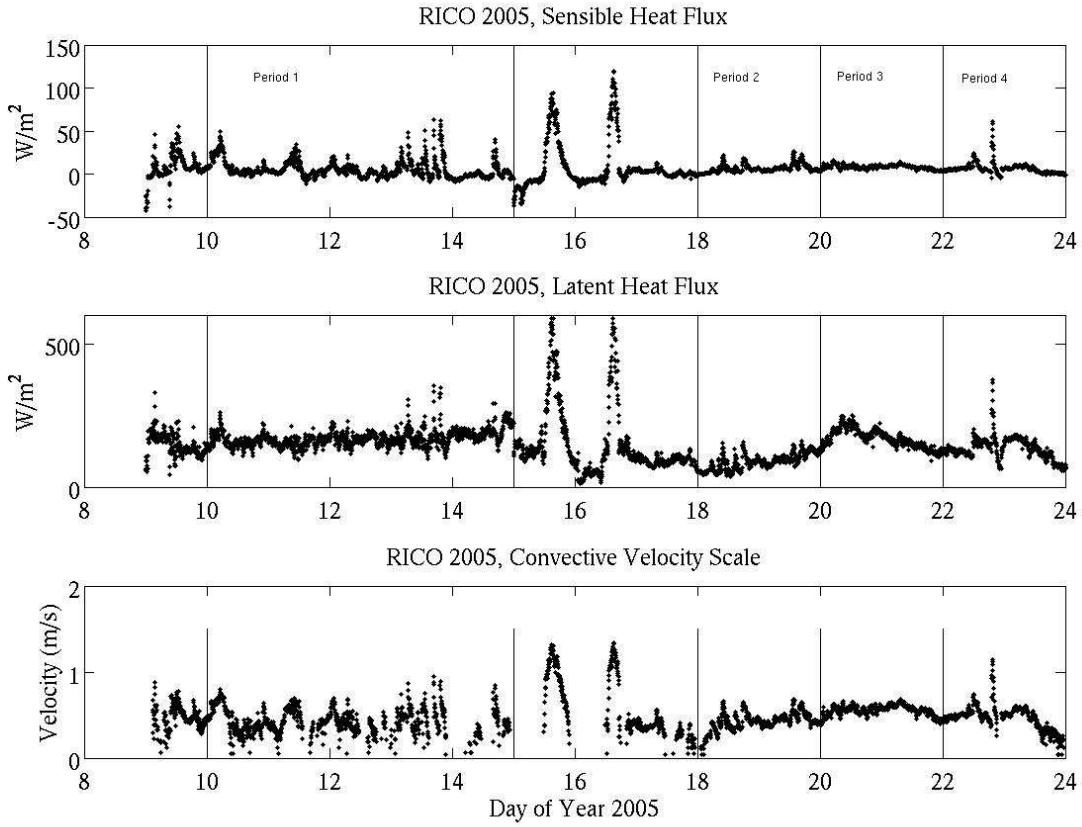


Figure 3.19: Time mapping of Sensible Heat Flux (top panel), Latent Heat Flux (middle panel) and Convective Velocity Scale (lower panel) during RICO.

### 3.4.5 Fractional Cloudiness and Precipitation Occurrence

The ceilometer backscatter can be used to estimate the height of the cloud base with a temporal resolution of 30 seconds and a spatial resolution of 15 m as was seen in Fig. 3.2 (blue dots). Fig. 3.20 shows a histogram of cloud base height from the ceilometer over the entire RICO cruise. The main peak is seen around 700 meters, which is the average cloud base height from SP1 and SP2. A second, less dramatic, peak is seen between 1400-2000 meters, and is related to the higher cloud bases during SP3 and SP4.

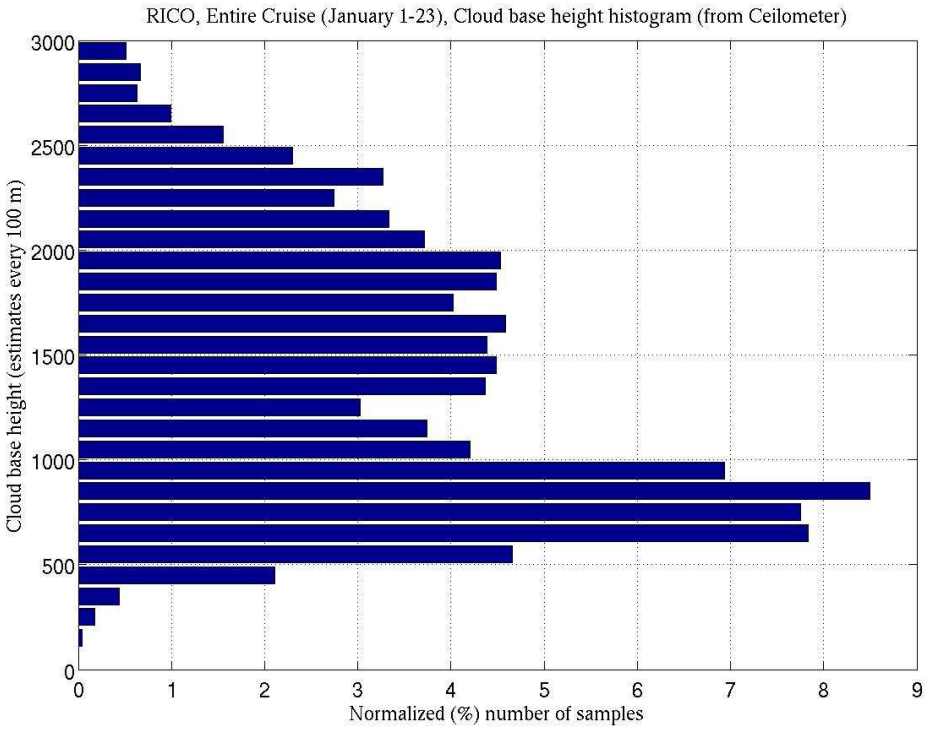


Figure 3.20: Histogram of cloud base height during RICO 2005.

Fractional cloudiness was highly variable during the RICO experiment. Fig. 3.21 shows the averaged fractional cloudiness by day. Typical fractional cloudiness in the tropical Atlantic trade wind winter regime is around .25-.30 (LeMone and Pennell 1976), and you can see that 7 of the days that were encountered during RICO were significantly above this value. These days were associated with enhanced convection and the passage of a surge line, which explains the additional cloud cover. Another way to look at fractional cloudiness is by hour. Fig. 3.22 shows the diurnal cycle of cloud fraction during RICO. Contrary to other studies (such as ATEX, Augstein et al. 1973) which saw a 20% higher cloud fraction during the night, RICO had the highest cloud fraction between 6-10 AM local time. Overall, there is not much diurnal variation in fractional cloudiness. Thus, even though the lidar was only operating during the daytime, the

turbulence statistics will most likely be representative of the entire day. A histogram of cloud fraction averaged over the entire RICO cruise is shown in Fig. 3.23. This figure demonstrates that while RICO did see more cloudy conditions than past experiments, the majority of the time still saw less than 10% cloudiness. All of the other cloud fraction bins show frequency occurrences less than 15% of the time.

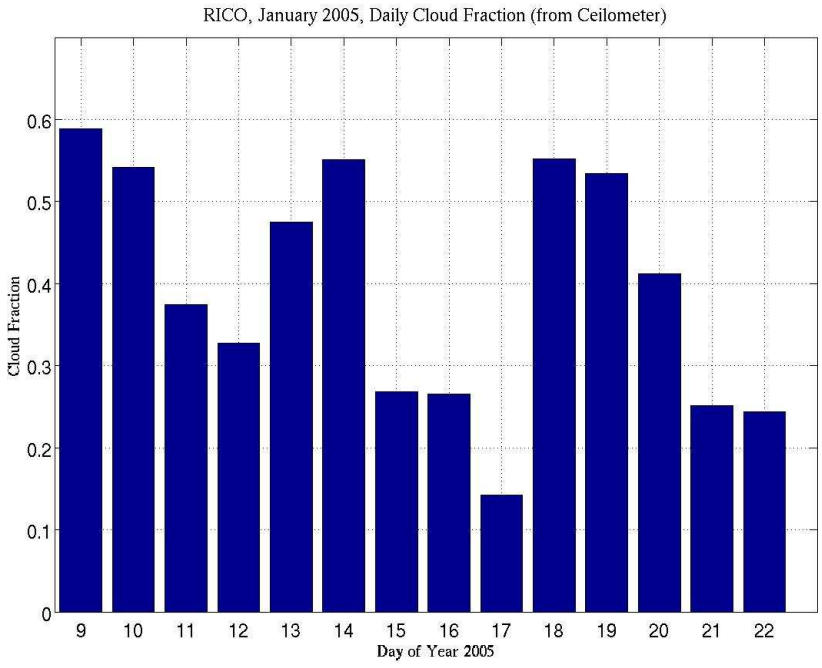


Figure 3.21: Daily averaged fractional cloudiness (from ceilometer) during RICO 2005.

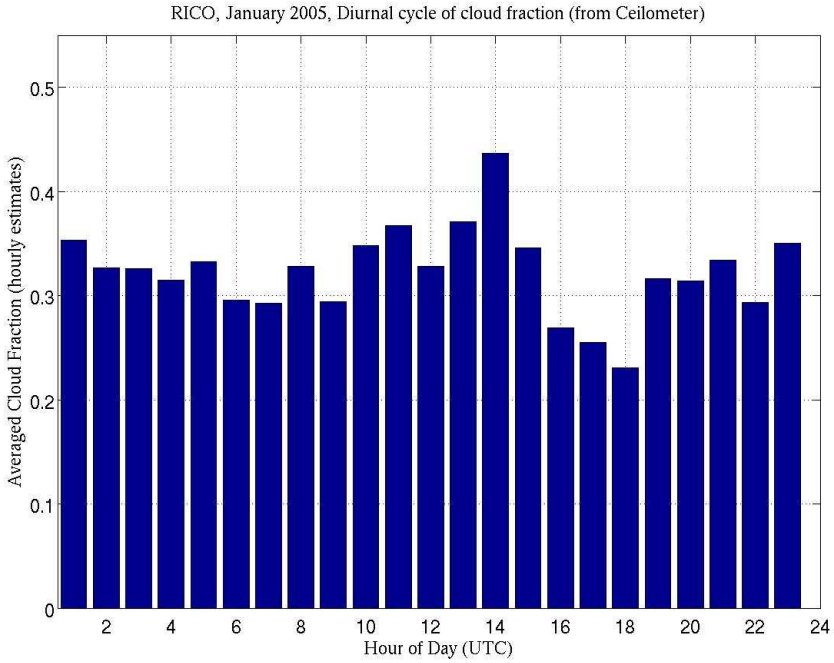


Figure 3.22: Histogram of hourly cloud fraction (from ceilometer) during RICO. Local time on the ship was 4 hours behind UTC.

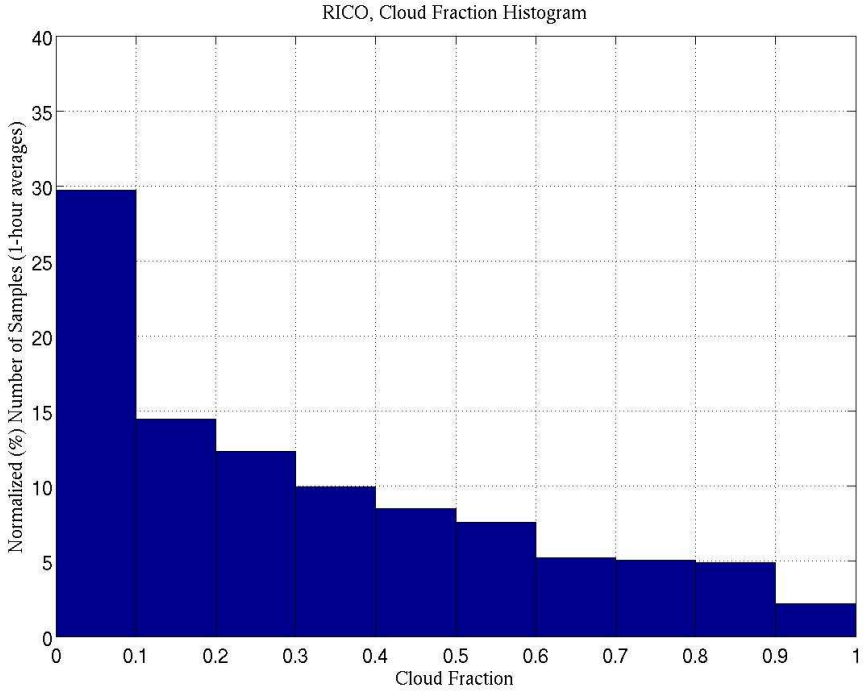


Figure 3.23: Cloud fraction histogram (from ceilometer) during RICO.

One final variable of interest in understanding the boundary layer is the rainfall amount. Although RICO was planned during a time period where rain events are typically non-existent or very small scale, the conditions encountered during Leg 1 were anything but dry as we experienced convective clouds with frequent shower activity. The rainfall was typically not too heavy during SP1 as compared to SP2, which saw a brief but very intense rainfall associated with the shear line on the 19$^{th}$ (Fig. 3.5). However, no rainfall was measured from the shear line passage on the island of Antigua (Ceasar 2005), as the ship just encountered one very moist cloud that then tracked west of the islands. This shows that while the data set collected on the ship is useful for understanding the trade wind weather conditions, it is just a point measurement and cannot be assumed to represent the entire Atlantic trade wind region.

### 3.4.6 All Fluxes Broken Down by Synoptic Period

A summary of the meteorological conditions at the surface during RICO are shown in Table 3.1. The overall cruise average is displayed along with the average from each Synoptic Period to facilitate with the comparisons among the periods and illustrate points not discussed previously. Most of the changes in the averaged variables occur during SP3 and SP4, where the LCL increases in height, the cloud fraction decreases to the “typical” amounts expected during the trade wind regime, the relative and specific humidity decrease, and both the solar and IR fluxes increase, which is expected due to less cloud cover. One unexpected feature during SP3 is an increased w*, up to 0.55 m/s. This is tied to an increase in sensible and latent heat fluxes and a deeper subcloud layer. During SP1

and SP2, wind speeds are very high, as is the bulk wind stress. Cloud fraction is higher, and the solar and IR flues are lower. SP2 has the highest rainrate, due to the brief but heavy rainfall on the 19$^{th}$. One unique feature seen during SP2 is a very low bulk latent heat flux, which is most due to the high values of relative humidity and low wind speeds.

| Variable | Cruise Mean | Synoptic Period 1 ($10^{th}$-$14^{th}$) | Synoptic Period 2 ($18^{th}$-$20^{th}$) | Synoptic Period 3 ($20^{th}$-$22^{nd}$) | Synoptic Period 4 ($22^{nd}$-$24^{th}$) |
|---|---|---|---|---|---|
| Latitude ($^{o}$N) | 17.8 | 17.9 | 17.8 | 17.9 | 17.7 |
| Longitude ($^{o}$W) | 61.7 | 61.7 | 61.7 | 61.7 | 61.8 |
| Bulk Wind Stress ($N/m^2$) | 0.104 | 0.171 | 0.037 | 0.077 | 0.052 |
| Bulk Sensible Heat Flux ($W/m^2$) | 5.24 | 6.14 | 6.37 | 8.03 | 5.64 |
| Bulk Latent Heat Flux ($W/m^2$) | 139 | 163 | 88.4 | 167 | 132 |
| Convective Velocity Scale (m/s) | 0.480 | 0.424 | 0.475 | 0.549 | 0.464 |
| True Wind Speed (m/s) | 7.97 | 10.7 | 5.02 | 7.19 | 6.17 |
| True Wind Direction | 72.9 | 75.6 | 57.1 | 43.6 | 64.9 |
| Air Temp (C) | 25.3 | 25.5 | 24.8 | 24.8 | 25.0 |
| Sea Snake Temp (C) (at -0.05m) | 26.2 | 26.3 | 26.1 | 26.1 | 26.1 |
| Sat. Specific Humidity (SST) | 20.8 | 21.0 | 20.7 | 20.8 | 20.7 |
| Specific Humidity | 15.0 | 15.7 | 15.5 | 13.3 | 14.1 |
| SST (Interface) (C) | 25.9 | 26.0 | 25.8 | 25.7 | 25.8 |
| Relative Humidity (%) | 74.7 | 77.0 | 78.8 | 67.7 | 70.9 |
| Downward Solar Flux ($W/m^2$) | 177 | 173 | 159 | 209 | 212 |
| Downward IR Flux ($W/m^2$) | 392 | 398 | 400 | 377 | 376 |
| Net Solar Flux ($W/m^2$) | 168 | 164 | 151 | 199 | 201 |
| Net IR Flux ($W/m^2$) | -59.4 | -54.1 | -51.4 | -74.4 | -74.7 |
| $Z_{LCL}$ (m) | 605 | 559 | 500 | 801 | 732 |
| Cloud Fraction (%) | 39.5 | 45.5 | 54.6 | 33.1 | 24.4 |
| Rainrate (mm/hr) | 0.154 | 0.169 | 0.338 | 0.014 | 0.031 |

Table 3.1: A list of the surface variables from the flux tower, ceilometer, and rain gage. Variables are averaged by Synoptic Period as well as the entire cruise.

# Chapter 4- Lidar Observations

## 4.1 Introduction

Typical data collection for the lidar during RICO entailed repeated sequences of four types of scans using a motion-compensated full-hemispherical scanner. The scan sequence consisted of short, full 360º PPI scans (repeated 3 times every hour and in between all other scans) to calculate horizontal mean winds versus altitude, sector scans at two levels and RHI scans to observe rain shafts, outflows, and other below-cloud wind activity. At the end of each hour, zenith stares allowed for measurement of vertical wind velocities. Fig. A2 (Appendix) shows a color-coded display of the actual scan schedule used during the ship-board portion of the experiment. Results in this study are only from data collected in the vertical, or zenith stare. This occurred for 10-20 minutes at the end of each hour that the lidar was operating. There were a few cases of a zenith stare of less than 5 minutes, which were discarded since they were too short to calculate worthwhile statistics from. Table A2 (Appendix) shows how many useful zenith stare files there were on each day during RICO. Each of these files was processed individually in terms of the data processing discussed in section 4.2, and then a composite file for each day was made for turbulence statistics by day, which are analyzed in section 4.3. Finally, each daily file was again composited into 4 files based on the Synoptic Periods, which are analyzed in section 4.5.

### 4.2 Data Processing

The motion-corrected vertically pointing lidar data were subjected to further post-processing before calculating any statistics. Examples of this post-processing are shown here for the same 15 minute case on January 11, 2005, from 14.75-15 UTC. The need for further data processing was revealed as I plotted the velocity as a time-height profile, as I noticed that some mesoscale features still remained in the vertical velocity data set (Fig. 4.1). To eliminate outliers from the data, all vertical velocities less than -5 m/s or greater than 5 m/s are removed. Further, any SNR values less than -5 dB and the corresponding velocities were removed. To remove the mesoscale variability, the perturbation velocity (w') at a given point is obtained by subtracting the mean velocity at that level for the time period from the observed w. An example of the w' field for the velocities shown in Fig. 4.1 is shown in Fig. 4.2, where red colors (positive values) represent updrafts and blue colors (negative values) represent downdrafts..

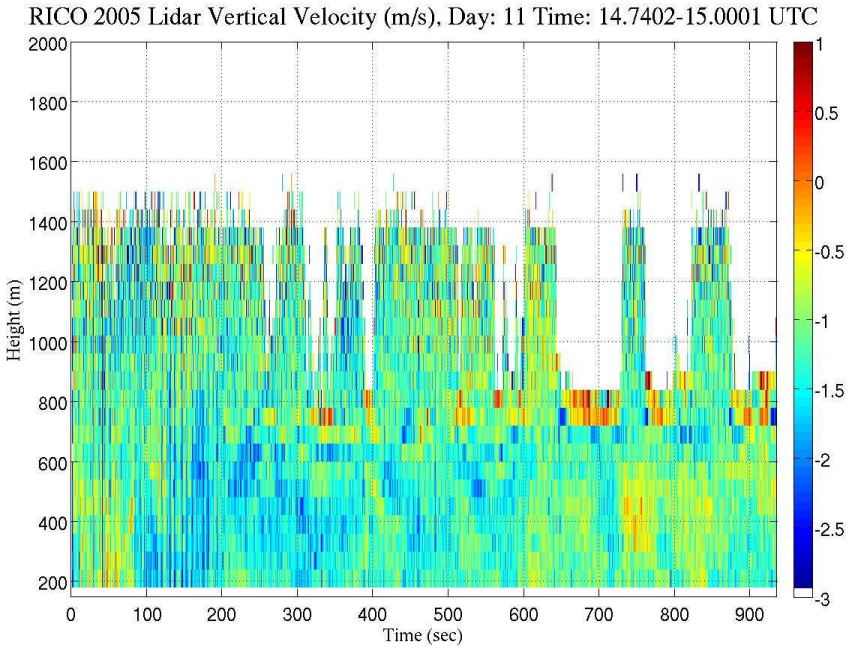


Figure 4.1: Time-height mapping of lidar unadjusted vertical velocities from January 11, 2005. Red colors (positive values) represent updrafts while blue colors (negative values) represent downdrafts.

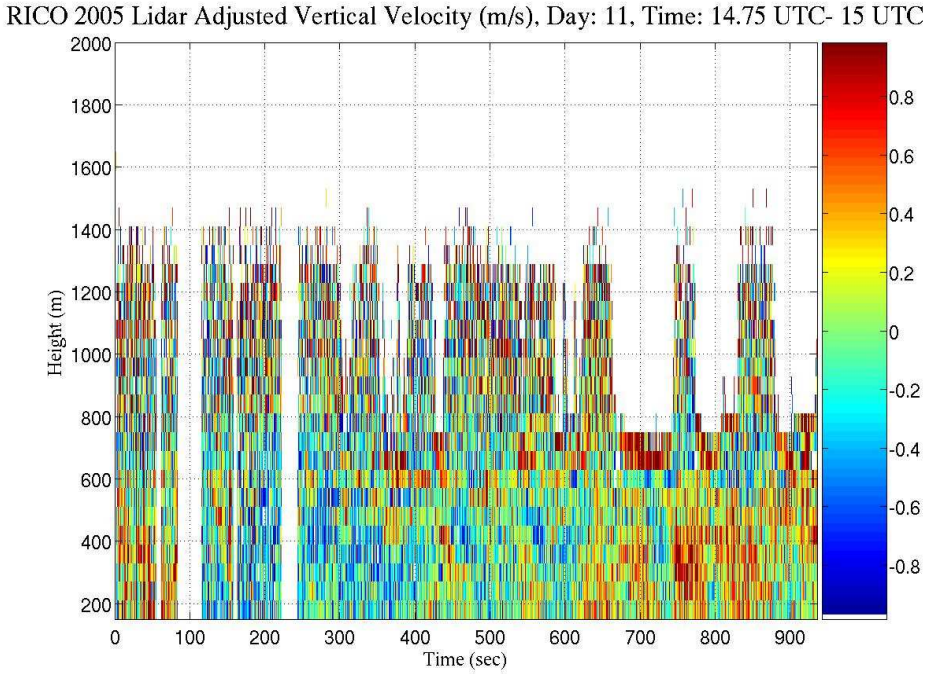


Figure 4.2: Lidar adjusted vertical perturbation velocity from January 11, 2005. Red colors (positive values) represent updrafts while blue colors (negative values) represent downdrafts.

The results shown in Fig. 4.2 show that removing the mean velocity at each height eliminates the bias of about -1 m/s seen in Fig. 4.1. Figure 4.2 also shows updrafts and downdrafts to a sufficiently small scale that small-scale turbulence (red colors right next to blue colors) becomes apparent. Further, the vertical extent of convective-scale updrafts and downdrafts, many of which extend from cloud base (about 600 m) down to 200 m, are clearly evident in the record. Although previous studies indicate that updrafts and downdrafts may only extend to about 100 meters below the cloud base (LeMone and Pennell 1976), these results show coherent updrafts and downdrafts extending over 400 meters from the cloud base that are in agreement with the findings by Emmitt (1978) during GATE.

For all of the data sets, I needed to find a cloud threshold SNR to determine if a cloud was present above the lidar at a particular time. After several trials, a SNR of 15 dB was determined to be the best threshold for finding the true cloud and thus the true cloud base. Figure 4.3 shows all SNR values with height vs. SNR 15 dB and up (Fig. 4.4) plotted with cloud base from the ceilometer (black dots) for the same case from January 11, 2005. The lidar clouds show excellent agreement with the ceilometer clouds, indicating that an SNR of 15 dB is a good indictor of a cloud. The radar returns shown in Fig. 4.3 illustrate how the lidar quickly becomes saturated even with small shallow clouds and cannot retrieve any useful information from above the cloud.

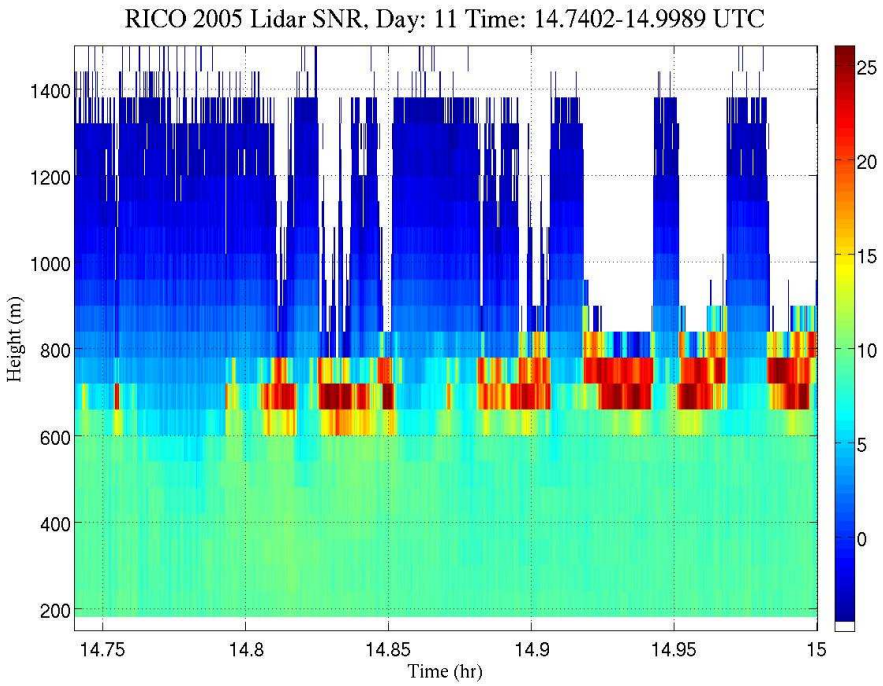


Figure 4.3: Time-height mapping for all SNR values for 14.75-15 UTC on January 11, 2005.

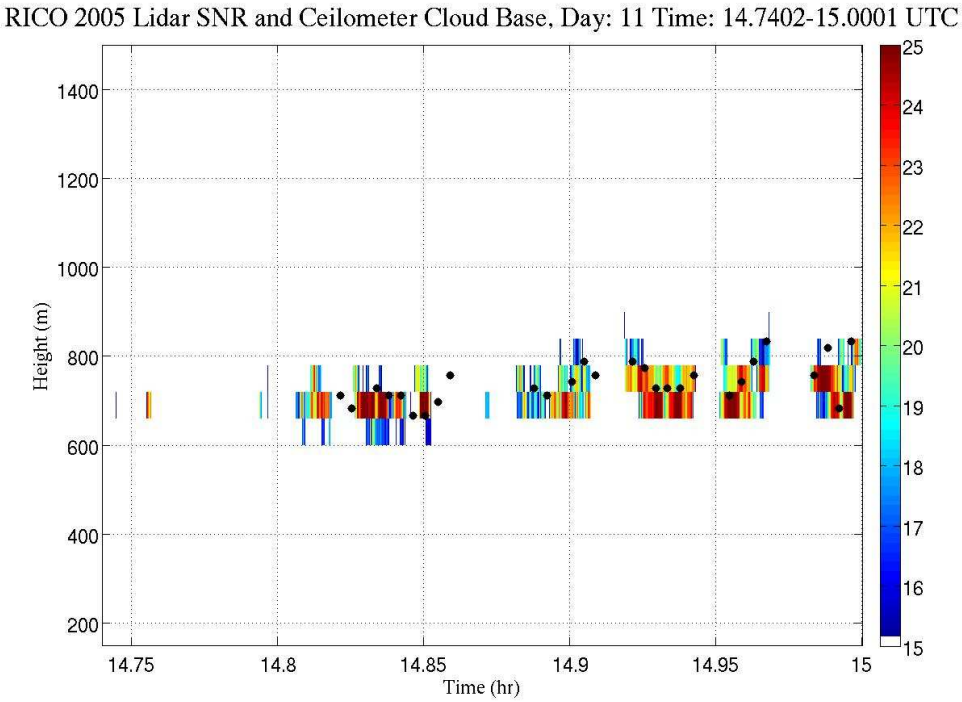


Figure 4.4: Lidar SNR>14 dB (color bar) and ceilometer cloud base (black dots) (bottom panel) for 14.75-15 UTC on January 11, 2005.

Using the 15 dB threshold, each one second record is evaluated to see if the SNR exceeds 14 dB anywhere in the lowest 2 km. If so, that entire column is tagged as a "cloud column", otherwise it is considered a "no-cloud column." This classification is done so that statistics can be calculated as cloud vs. no cloud conditions to see the effect the cloud has on the subcloud region. An example of this distinction is shown in Fig. 4.5 which shows the maximum value of SNR below 2 km in each one second time column. Columns with SNR values greater than 14 dB are marked as "cloud" columns (shown here as red squares). These lidar-determined clouds have good agreement with the clouds found by the ceilometer in Fig. 4.4. A similar classification was also done for updrafts, where the maximum velocity in each one second column (again below 2 km) is plotted and any velocities exceeding 1 m/s are tagged as strong updrafts (not shown).

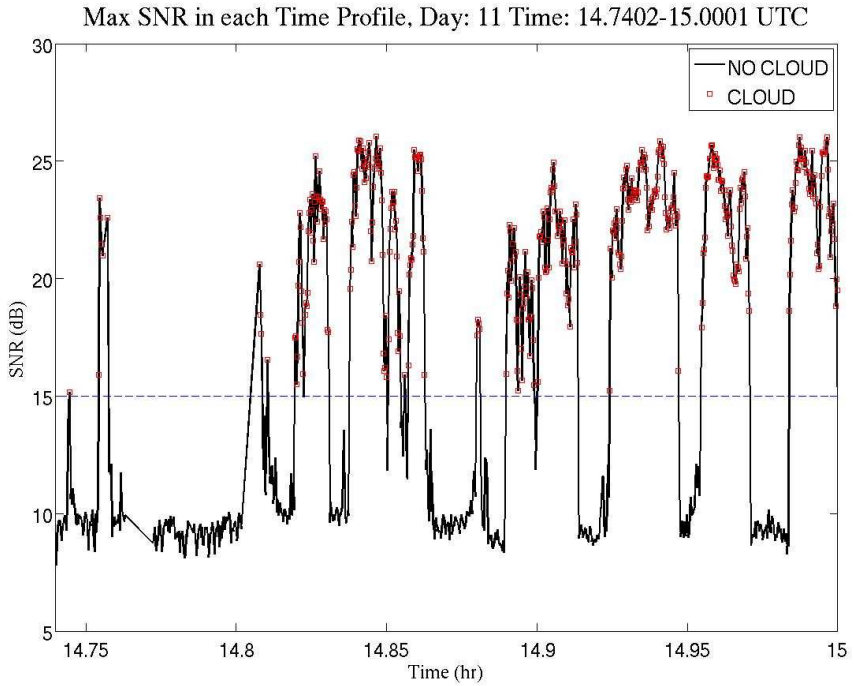


Figure 4.5: Maximum SNR in each time profile (black) from 14.75-15 UTC on January 11, 2005. Tagged cloud columns are shown as red squares. The dashed blue line represents the SNR threshold of 15 dB for determining whether or not a cloud is present.

Another way to display the vertical velocity perturbations with height is to plot the velocity vs. time at each gate, starting from the surface and extending up to cloud base. This is shown in Fig. 4.6 with a factor of 2 added onto the values in each gate to separate them. The distinction between cloud (red) and no cloud (blue) conditions is shown. With this type of image, it is easy to see coherent updrafts and downdrafts, especially under the clouds, extending over 7 or 8 gates (400-500 meters) vertically.

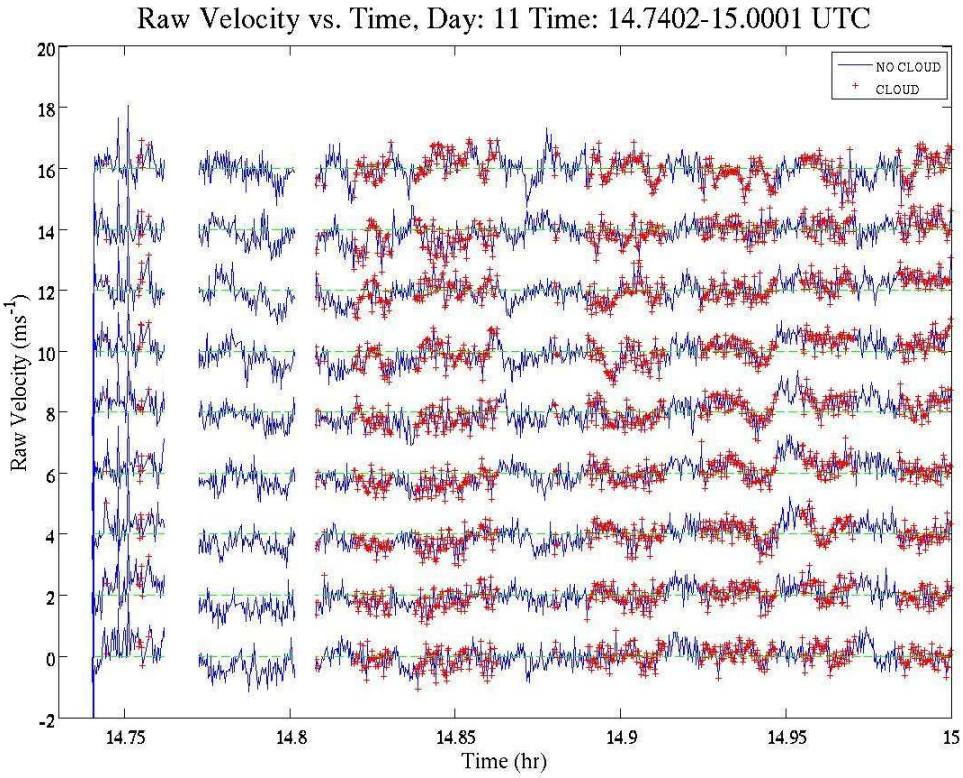


Figure 4.6: Raw velocity at each gate from 14.75-15 UTC on January 11, 2005. Tagged cloud columns are shown in red, no-cloud columns in blue. There is a factor of 2 separating each gate for distinction. Dashed green lines show zero velocity at each gate.

One final correction that was made was the removal of the first five samples (or first five seconds) of each file. This was done because as the lidar switches to a new scanning mode (in this case the zenith mode), it takes a few seconds to stabilize and faulty velocity

values can be returned. These are seen in the first few samples in Fig. 4.6. Such artifacts were removed from every data set.

### 4.3 Daily Turbulence Statistics

As the individual lidar files were combined into daily files, it was determined that some additional scaling and data removal was necessary before turbulence statistics could be calculated. First, I normalized all of the heights by the height of the LCL calculated from the surface fluxes. This gave us a scaled height range of 0 to 1, where 0 represents sea level and 1 represents cloud base. I also normalized all $\sigma_w$ by the mean w* in each time period. These two normalizations allow for a more direct comparison of turbulence, regardless of the weather conditions. For each day I plotted the profile of $\sigma_w/w^*$ vs. $Z/Z_{LCL}$ for each 10-15 minute file, as shown in Fig 4.7 for the 7 individual files on January 18$^{th}$. The top panel shows $\sigma_w$ vs. $Z/Z_{LCL}$, and the bottom shows $\sigma_w/w^*$ vs. $Z/Z_{LCL}$. For many of the days, normalizing by w* caused the individual profiles to collapse together in the bottom panel. If there was one profile that remained a significant outlier despite the normalizations, that file was removed before daily compositing was done, as was the case for the profile shown in green here.

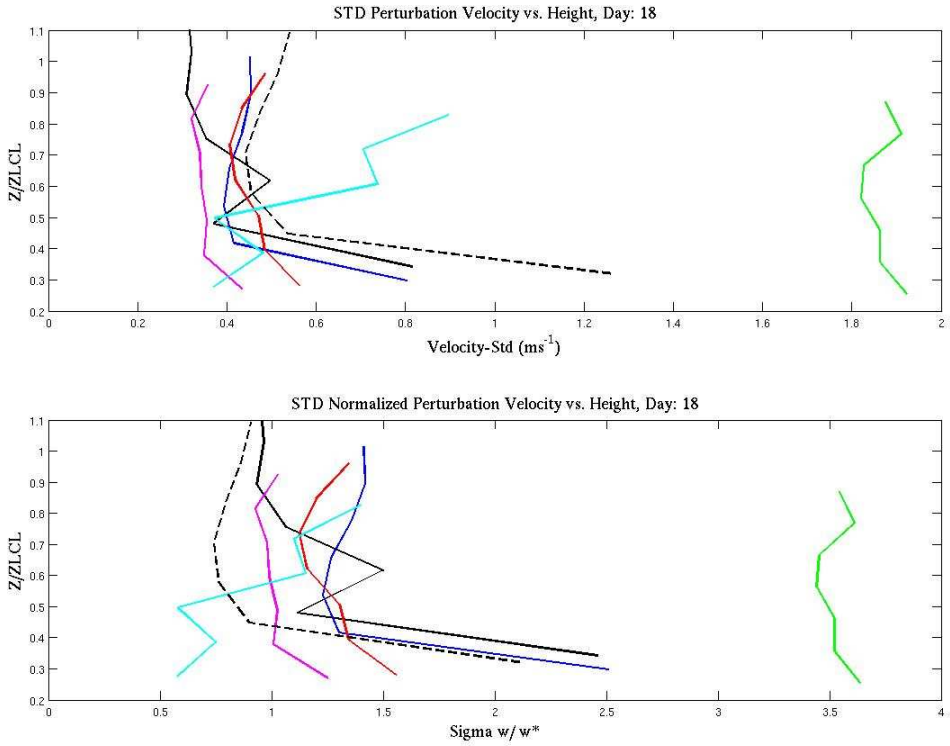


Figure 4.7: Individual profiles of $\sigma_w$ vs. $Z/Z_{LCL}$ (top) and $\sigma_w/w^*$ vs. $Z/Z_{LCL}$ (bottom). Each color in the top panel corresponds to the same profile in the bottom panel.

Fig. 4.7 raises another lidar issue, which is that occasionally the first lidar gate (60-120 m) does not provide accurate information. Normally this gate is ignored, but since it is important to this thesis to show the turbulence structures as close to the ground as possible, it is included. However, if lowest data point appears out of range (as it does in 3 of the profiles here) its implications about the turbulence profiles should be ignored.

### 4.3.1 FFT Profiles

After combining the individual files into daily files, I calculated the spectra of the velocity perturbation at each gate below cloud base, shown for January 14$^{th}$ in Figure 4.8. Each spectrum is logarithmically smoothed so that several gates could be plotted on the

same figure without the small scale peaks in each curve becoming distracting. A -5/3 slope line is also shown (thick black line) to demonstrate how well the spectra follows the idealized turbulence theory that low frequency motions should have a -5/3 slope. It is easy to see that the lower frequency (higher time scale) motions closely follow this slope. However, at frequencies higher than 0.3 Hz there is a deviation from the -5/3 slope due to high frequency motions and noise. There is a secondary peak in the spectra at several of the gates below cloud base around 0.1 Hz. This smaller peak is due to motions on a time scale of 10 seconds and spatial scale of 100 m, and may be due to ship motion residuals since it shows up in almost every daily spectral image.

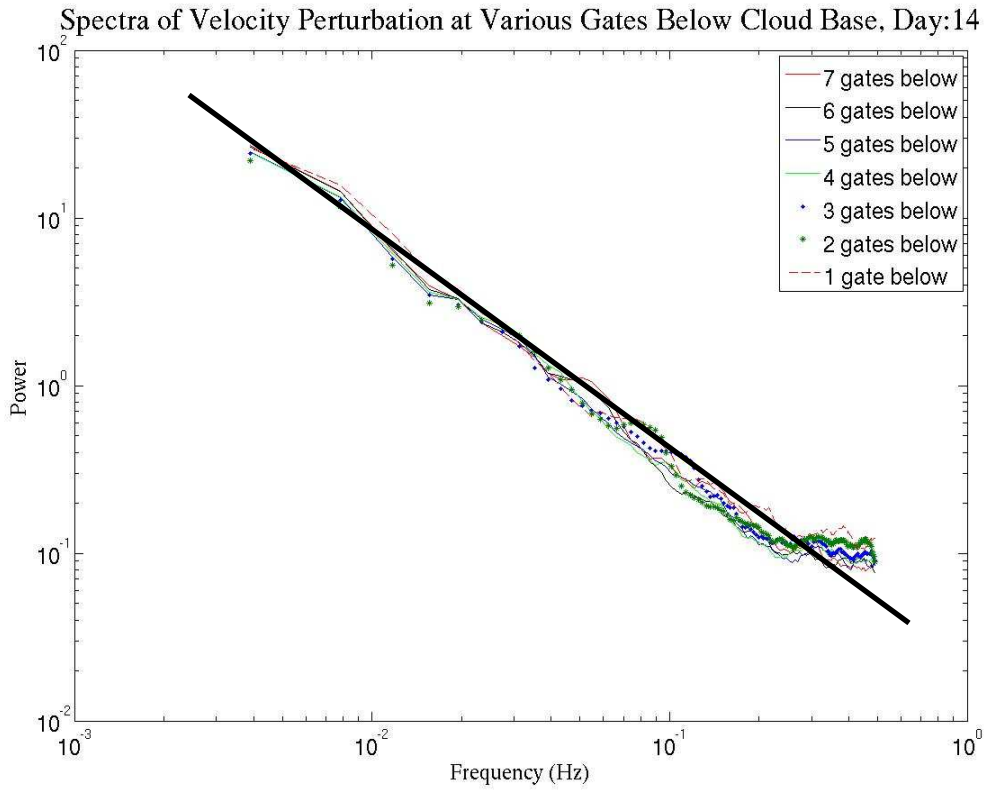


Figure 4.8: FFT of velocity perturbation at each gate (60 m each) below cloud base on January 14, 2005. Thick black line shows -5/3 slope line.

### 4.3.2 Cloud and Updraft Occurrences

To help understand the daily conditions and how they affect the turbulence statistics, Table 4.1 shows percentages of time that clouds, strong updrafts (w> 1 m/s) and both occur during each day, calculated from lidar observations. Cloud cover is highest on the 12$^{th}$, 20$^{th}$ and 22$^{nd}$ and lowest on the 10$^{th}$, 18$^{th}$ and 21$^{st}$. Strong updrafts occur most often on the 9$^{th}$, 12$^{th}$, 13$^{th}$ and 22$^{nd}$ and are associated with high cloud tops (3-4 km) and precipitation. The percentage of time that a cloud and a strong updraft occur at the same time are highest on the 9$^{th}$, 12$^{th}$, 20$^{th}$ and 22$^{nd}$ and lowest on the 10$^{th}$, 16$^{th}$, 21$^{st}$ and 24th. Average velocity at cloud base is significantly higher on January 12$^{th}$ than any other day, although it is still high on the 17$^{th}$, 18$^{th}$ and 22$^{nd}$. Only three days during RICO show net downdrafts at cloud base (14$^{th}$, 21$^{st}$ and 24$^{th}$). These three days had shallow, short-lived cumulus clusters that were organized in lines oriented from NE-SW. Velocity variations at cloud base are highest on the 12$^{th}$, 17$^{th}$, 18$^{th}$, 22$^{nd}$ and 23$^{rd}$, which is not surprising given that a larger range of values would occur with the high velocities at cloud base on these days. In the lowest 600 m of the boundary layer (below cloud base on all days), strong updrafts dominate on the 9$^{th}$ and 12$^{th}$, while weak downdrafts dominate on the 14$^{th}$, 16$^{th}$, 17$^{th}$ and 21$^{st}$. Variations in velocity in the lowest 600m are high on the 12$^{th}$, 13$^{th}$ and 22$^{nd}$, which is expected due to the high amounts of cloud cover and strong updrafts present on these days.

| Date in January 2005 | % Clouds | % Strong Updrafts | % Clouds & Updrafts | Average Velocity at Cloud Base (m/s) | STD of Perturb-ation Velocity at Cloud Base (m/s) | Mean Velocity in Lowest 600m | STD Velocity in Lowest 600m |
|---|---|---|---|---|---|---|---|
| **9** | 21.6 | 27.6 | 10.0 | 0.207 | 0.500 | 0.203 | 0.057 |
| **10** | 16.1 | 7.60 | 1.29 | 0.008 | 0.362 | -0.041 | 0.018 |
| **11** | 30.7 | 14.0 | 8.28 | 0.030 | 0.429 | 0.077 | 0.039 |
| **12** | 58.7 | 35.4 | 21.7 | 0.286 | 0.713 | 0.296 | 0.195 |
| **13** | 26.9 | 21.0 | 8.07 | 0.069 | 0.414 | 0.036 | 0.263 |
| **14** | 32.7 | 13.8 | 6.52 | -0.024 | 0.426 | -0.049 | 0.028 |
| **16** | 19.9 | 4.14 | 2.70 | 0.006 | 0.315 | -0.017 | 0.053 |
| **17** | 23.2 | 7.93 | 5.89 | 0.148 | 0.721 | -0.002 | 0.087 |
| **18** | 10.6 | 15.1 | 5.50 | 0.139 | 0.749 | 0.114 | 0.099 |
| **19** | 23.0 | 11.6 | 5.78 | 0.089 | 0.377 | 0.127 | 0.092 |
| **20** | 65.6 | 14.1 | 10.7 | 0.119 | 0.436 | 0.093 | 0.072 |
| **21** | 17.2 | 10.4 | 3.96 | -0.023 | 0.285 | -0.015 | 0.060 |
| **22** | 55.3 | 19.1 | 9.54 | 0.135 | 0.722 | 0.096 | 0.212 |
| **23** | 35.1 | 8.87 | 4.66 | 0.044 | 0.735 | 0.084 | 0.124 |
| **24** | 43.9 | 2.72 | 1.70 | -0.048 | 0.538 | 0.092 | 0.135 |

Table 4.1: Cloud, updraft, and turbulence statistics each day during RICO.

### 4.3.3 Fractional Cloudiness and Updrafts

The lidar can also be used to calculate fractional cloudiness and fractional updrafts that depend on the set thresholds for marking clouds and updrafts. In order to calculate the fractional cloudiness, I used the same cloud threshold of 15 dB as the previous sections. Updraft fraction was calculated for two different thresholds, the first being the same “strong updraft” threshold used in section 4.3.2 of w>1 m/s. The second threshold

used the perturbation velocities and called anything where w'>0.5 m/s an updraft. This value was chosen instead of the expected w'>0 m/s to avoid calling any downdraft an updraft due to the removal of the mean velocity at each height shown in section 4.2. The overall updraft fraction may be slightly underestimated due to this choice, but it is done to avoid gross overestimation by lowering the threshold too much. Daily fractional cloudiness from the ceilometer and lidar, along with the fraction of updrafts and strong updrafts from the lidar are listed in Table 4.2. As mentioned before, the ceilometer was shut down early, so no fractional cloudiness information is available for the 23$^{rd}$ or 24$^{th}$. A striking feature seen here is that the lidar sees a much lower cloud fraction than the ceilometer. The obvious explanation for this is that the lidar observations used to make these calculations cover less than 10% of the time that the ceilometer covers on a given day so the lidar could encounter fewer clouds during this time period and result in a skewed viewpoint of the fractional cloudiness. Some of the days (12$^{th}$, 17$^{th}$, 20$^{th}$ and 22$^{nd}$) do show a higher cloud fraction from the lidar, which should be taken into account when looking at the fractional updrafts. If the lidar zenith stares encountered more clouds than the daily average, the higher fractional updrafts during these time periods should not be assumed to represent the average conditions over the entire day. Updraft fraction is between .2-.45 during RICO, with strong updrafts occurring between 3 and 21% of the time. Despite more convective conditions and disturbed weather during SP1 and SP2, the overall fraction of updrafts is only slightly higher during these two periods. However, strong updrafts are much more common, leading to the conclusion that mass flux into cloud base should also be higher during these times.

| Date in Jan. 2005 | Fractional Cloudiness (ceilometer) | Fractional Cloudiness (lidar) | Fractional Updrafts (lidar, w'>0.5 m/s) | Fractional Strong Updrafts (lidar, w>1 m/s) |
|---|---|---|---|---|
| **9** | .589 | .216 | .326 | .276 |
| **10** | .542 | .161 | .339 | .076 |
| **11** | .374 | .307 | .358 | .140 |
| **12** | .328 | .587 | .435 | .354 |
| **13** | .475 | .269 | .364 | .210 |
| **14** | .551 | .328 | .452 | .139 |
| **16** | .265 | .200 | .305 | .041 |
| **17** | .143 | .232 | .240 | .089 |
| **18** | .552 | .107 | .313 | .151 |
| **19** | .534 | .230 | .276 | .116 |
| **20** | .412 | .656 | .419 | .141 |
| **21** | .251 | .172 | .387 | .104 |
| **22** | .244 | .553 | .423 | .191 |
| **23** | N/A | .351 | .328 | .090 |
| **24** | N/A | .439 | .206 | .028 |

Table 4.2: A list of statistics of fractional cloudiness and fractional updrafts each day during RICO.

### 4.4 Mass Flux

The mass flux is calculated from the lidar data following the method of Kollias and Albrecht (2000) using Eq. 4.1 where $M_c$ is the mass flux at a given height over a time period, ρ is density, σ is fractional area of updrafts over the time period, $w_u$ is average vertical velocity of updrafts, and $w_d$ is average vertical velocity of downdrafts.

$$M_c = \rho\sigma(1-\sigma)(w_u - w_d) \quad \text{(Eq. 4.1)}$$

Since I am using the perturbation vertical velocity to remove mesoscale vertical velocity variability, I set the threshold for updrafts as w'> 0.5 m/s. If a column does not have a w' value greater than this threshold below cloud base, that column is marked as a downdraft for statistical purposes. Several updraft thresholds between 0<w'<0.5 m/s

were tested before this value was chosen. The resulting mass flux curves from each trial are shown in Fig. 4.9 from January 23rd where the x-axis is mass flux normalized by the surface w* and the y-axis is height normalized by the height of the LCL so 0 represents the surface and 1 represents cloud base. The curve with the threshold of w'>0.5 best agrees with the values found by Nicholls and LeMone (1980, see Fig. A3 in Appendix). The x-axis values are almost exactly in agreement, which is expected since the 23rd is one of the days where we encountered typical trade wind conditions, and Nicholls and LeMone saw comparable conditions over the 4 days that they show in their figure. Figure 4.10 shows mass flux normalized by w* for each of the Synoptic Periods from Chapter 3 (solid lines) along with interpolated GATE values (stars). While the overall shape of these curves is similar by period, the curve from SP1 has much higher mass flux values, showing how the increased convection could be due to greater mass flux throughout the subcloud layer. Overall, the mass flux curve shows increasing mass flux from the surface into the middle of the subcloud layer, at which point it starts to feel the effect of the TWI or cloud base overhead and the vertical transport decreases in magnitude.

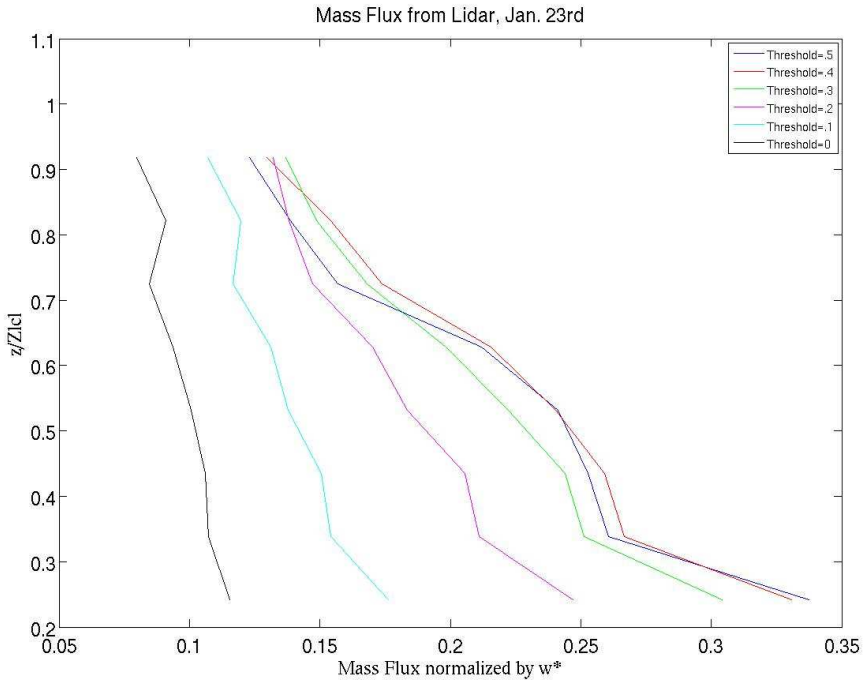


Figure 4.9: Mass flux curves from lidar data for January 23rd. Each velocity threshold is shown as an individual curve.

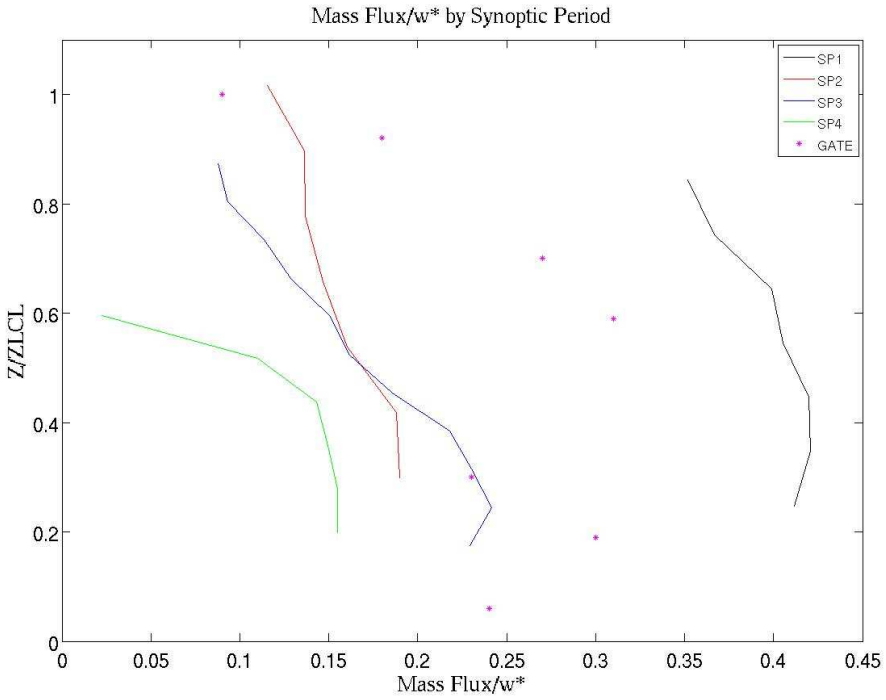


Figure 4.10: Mass flux curves from lidar data for SP1 (black line), SP2 (red line), SP3 (blue line) and SP4 (green line). Magenta stars show interpolated values calculated by Nicholls and LeMone (1980) during GATE.

Table 4.3 shows the daily mass flux at cloud base from the lidar along with the w* value at 14 m from the flux tower. As expected, the mass flux is higher from the $12^{th}$-$14^{th}$ as a passing trough caused the atmosphere to become more unstable and increased vertical transport. The ratio of mass flux to w* should remain fairly constant over all of the days regardless of weather conditions, as each should be higher on days with more convection, but it varies with much higher values during SP1 and SP2. This indicates that processes other than surface fluxes may be affecting the mass flux.

| DATE | Mass Flux (cloud base) | w* (surface) | Ratio of Mass Flux (Base)/w* |
|---|---|---|---|
| **9** | 0.124 | 0.460 | .269 |
| **10** | 0.081 | 0.340 | .237 |
| **11** | 0.081 | 0.336 | .241 |
| **12** | 0.242 | 0.448 | .540 |
| **13** | 0.197 | 0.532 | .105 |
| **14** | 0.155 | 0.466 | .332 |
| **16** | 0.066 | 0.654 | .101 |
| **17** | 0.089 | 0.268 | .332 |
| **18** | 0.089 | 0.426 | .210 |
| **19** | 0.067 | 0.525 | .128 |
| **20** | 0.061 | 0.549 | .111 |
| **21** | 0.048 | 0.550 | .087 |
| **22** | 0.060 | 0.507 | .118 |
| **23** | 0.057 | 0.466 | .122 |
| **24** | 0.050 | 0.418 | .120 |

Table 4.3: A list of daily mass flux and w* during RICO.

## 4.5 Coupling Turbulence with Synoptic Periods

### 4.5.1 Cloudy vs. Clear Conditions

The mean vertical velocity and variance are good general indicators of boundary layer turbulence, and using the cloud threshold, the total variance can be separated into the components associated with clouds and clear areas. To better understand how various synoptic conditions affected the turbulence profiles, the lidar data were grouped into the four Synoptic Periods described in Chapter 3. The height used for this analysis is the actual height normalized by the height of the LCL so that 0 is the surface and 1 is cloud base. Cloud base influences are seen in most of the profiles beginning around $z/z_{LCL}$ = z*=0.8 due to averaging of the files over each day and using LCL as a scaling height rather than the cloud base height defined by the lidar SNR. The large jumps in the turbulence profiles between 0.8 and 1 may include some cloud sampling as indicated by the increase in the SNR. This cloud sampling may introduce artifacts due to the lidar chirp effect discussed earlier. Since it is useful to normalize the height axis to effectively compare results from different days and under different weather conditions, the LCL scaling is maintained, although the actual cloud base may be in the range of z* = 0.8 and 1.

Each composite synoptic period file was used to calculate mean and standard deviation of w' for clouds vs. clear sky. Figure 4.11 shows the mean profile of w' along with the frequency of occurrence of each w' value at each height for SP1. From this figure, we can see that the mean vertical velocities are very close to 0 under clouds and

clear sky. Under clouds (upper panel), there is a slight bias towards positive velocities, signifying the slight influence of updrafts. Fig. 4.12 shows turbulence results in the form of $\sigma_w/w^*$ vs. height, where the red profiles represent conditions under clouds, the blue profiles represent clear sky and the black profiles are an average of all conditions. For SP1, we see that the variance of w' under clear sky decreases with height, while under clouds it decreases at first and then increases into cloud base. This is most likely due to the influence of both updrafts and downdrafts just under cloud base as SP1 had the most convective conditions with very active clouds, an ill-defined TWI, cloud tops penetrating 2-3 km and frequent rainfall.

Normally in the tropical Atlantic trade wind regime under clear skies or very weak, shallow cumulus clouds, you would expect to see a profile similar to that found by Nicholls and LeMone during GATE (see Fig. A4, Appendix). The clear sky variance profile that we see during SP1 seems to follow the same shape as the upper half of the Nicholls and LeMone curve, but since the lidar does not collect accurate data in the lowest 150 meters of the atmosphere, it is difficult to know if our clear sky curve would follow their curve in the lower subcloud layer. To get a better idea of this, the green symbol in Fig. 4.12 shows the flux tower value of $\sigma_w/w^*$ for SP1. An extrapolation from the lidar observations to the flux tower turbulence would give a turbulence structure similar to GATE during RICO suppressed conditions. The deviation from this profile only occurs with convective conditions and active clouds overhead.

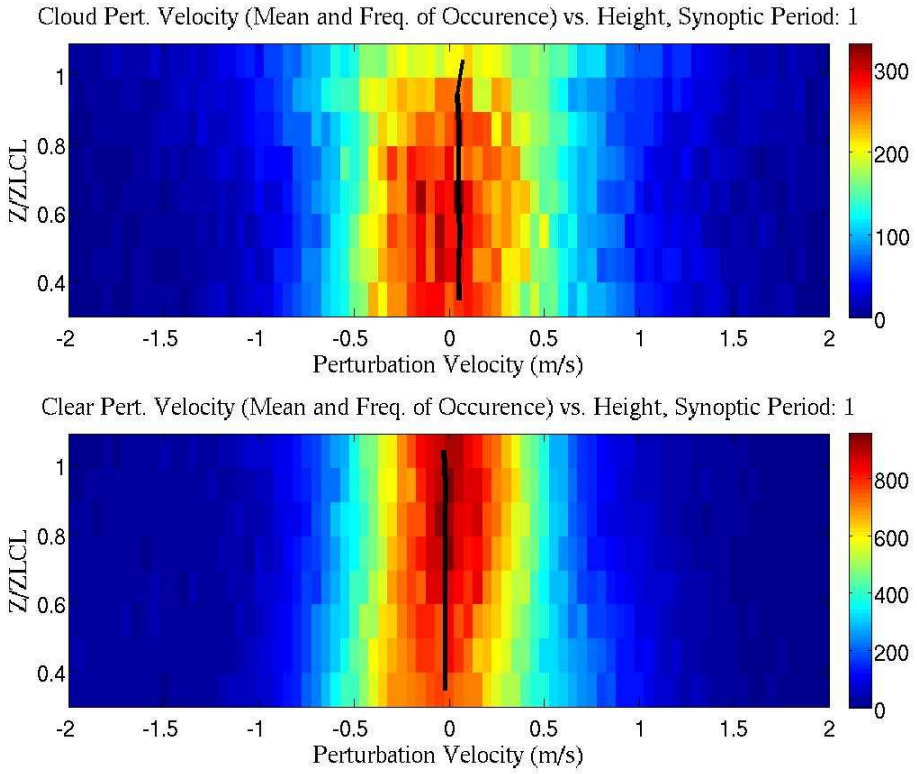


Figure 4.11: Perturbation velocity (w') for SP1. Black curve is a mean of all w' at each height for clouds (upper panel) and clear sky (lower panel). Colors represent frequency of occurrence for each perturbation velocity value at each height, where red colors are located at the most common w' values.

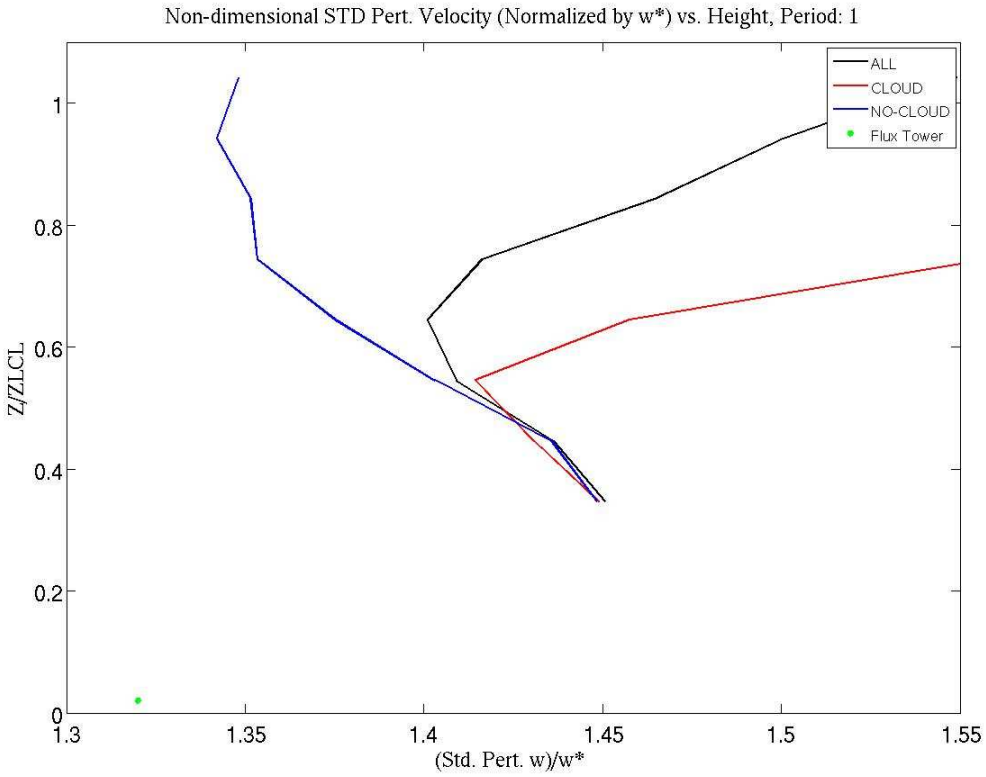


Figure 4.12: Standard Deviation of w' normalized by w* for SP1 (January 10th-14th). Red curve represents columns under clouds, the blue curve represents clear sky and the black curve is a mean of all conditions. Green star represents $\sigma_w/w^*$ from the flux tower (14m height) for all conditions in the same time period.

Figure 4.13 shows the spectra of the perturbation velocity at each gate below cloud base for SP1. Low frequency motions follow the expected -5/3 slope line of turbulence on a log-log plot, although there is some deviation from this line due to the very active conditions of SP1. There is a large peak on time scales of 5-10 seconds, which is due to increased ship pitching and rolling under the high wind speeds that occurred during this period. Some of this high frequency variation may be related to “streaks” seen in the lidar data on January 12th. Some, but apparently not all, of this streakiness was removed during data processing.

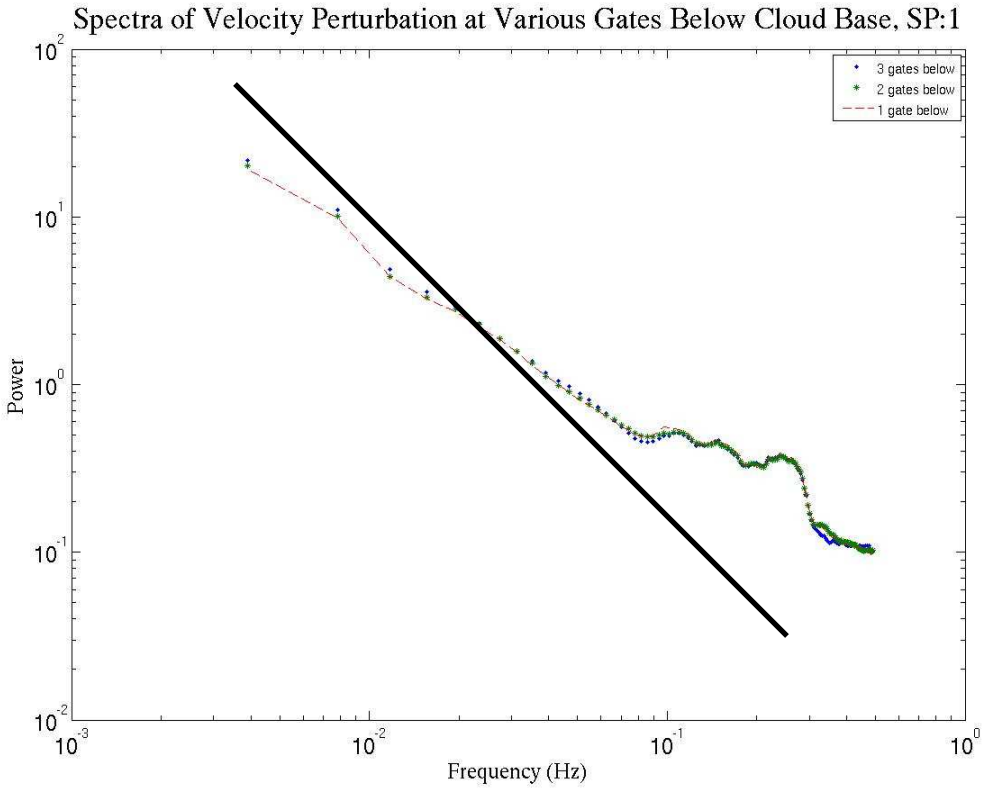


Figure 4.13: Spectra of w' shown on a log-log plot for SP1 (January 10th-14th) at 60 m below cloud base (dashed red), 120 m below cloud base (green star) and 180 m below cloud base (blue star). Thick black line shows expected -5/3 slope line of turbulence.

Figure 4.14 shows the turbulence profiles for SP2. As seen for SP1 (Fig. 4.12), our clear sky variance profile and flux tower observations follow those of Nicholls and LeMone (Fig. A4), while the CLOUD variance profiles increase in height towards cloud base. The increasing variance with height is due to the presence of strong updrafts and downdrafts from clouds, while the decrease just below base is most likely caused by the increase in downdrafts just beneath the clouds associated with the heavy precipitation observed on the 18th. The mean w' under clouds is positive in the middle of the subcloud layer but decreases with height, becoming negative as it approaches cloud base (not shown). This is due to the influence of downdrafts and rainfall out of the clouds.

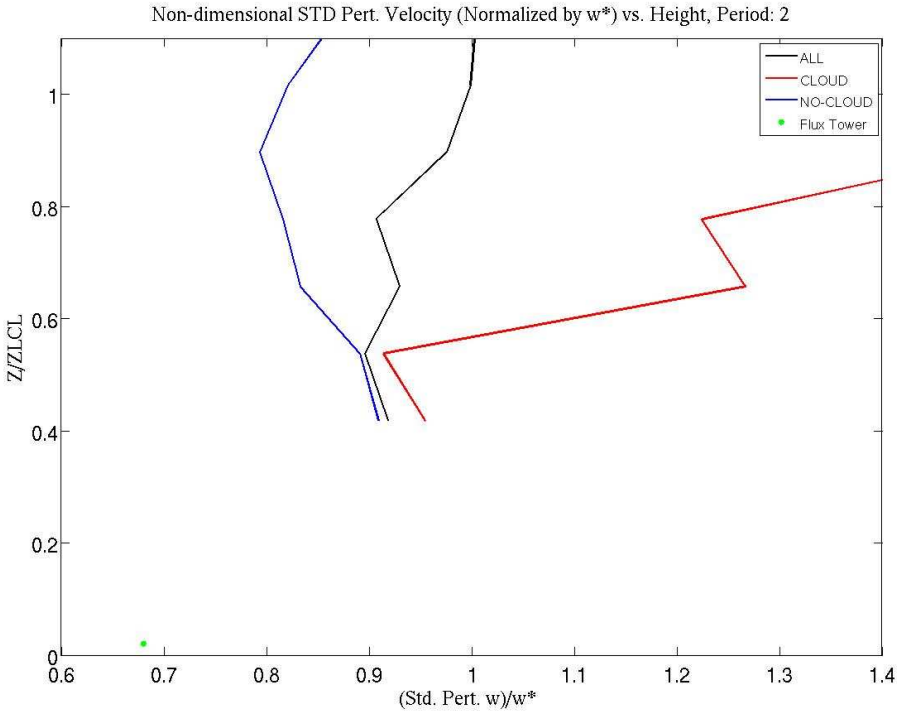


Figure 4.14: As in Figure 4.12, except for SP2 (January 18$^{th}$-20$^{th}$).

Figure 4.15 shows the spectra of the perturbation velocity at each gate below cloud base for SP2. Again, low frequency motions follow the expected -5/3 slope line of turbulence very closely, but there is still a deviation due to ship motion and noise at higher frequencies. The low frequency motions are on a smaller scale than seen during SP1, which may be representative of less intense convective-scale motions.

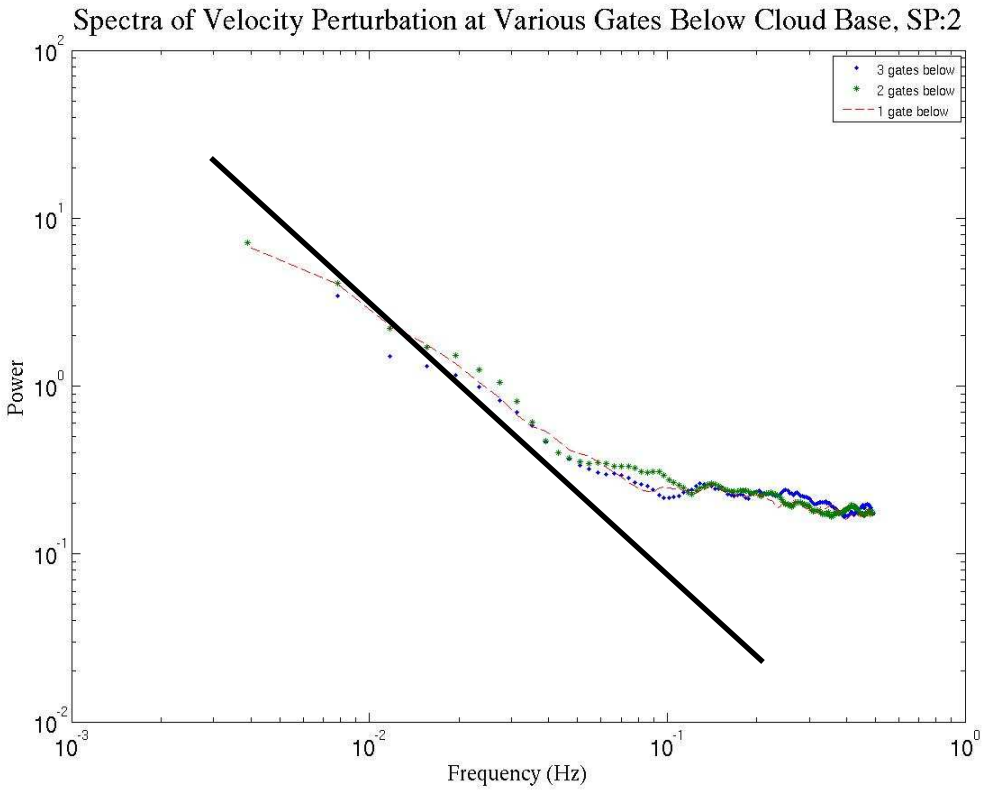


Figure 4.15: As in Fig. 4.13, but for SP2.

Figure 4.16 shows the turbulence profiles for SP3, which had the most suppressed conditions observed during RICO. While clouds were still present, they were very weak and shallow and typical of the wintertime trade wind regime. For this reason, we expect that our velocity variance curves should most closely follow those of Nicholls and LeMone, which they do as all three profiles decrease with height from the middle of the subcloud layer to cloud base. It is easy to imagine that interpolating a curve from the lowest lidar height down to the flux tower point would give the same inverted ‘C’ shape curve as seen in Fig. A4.

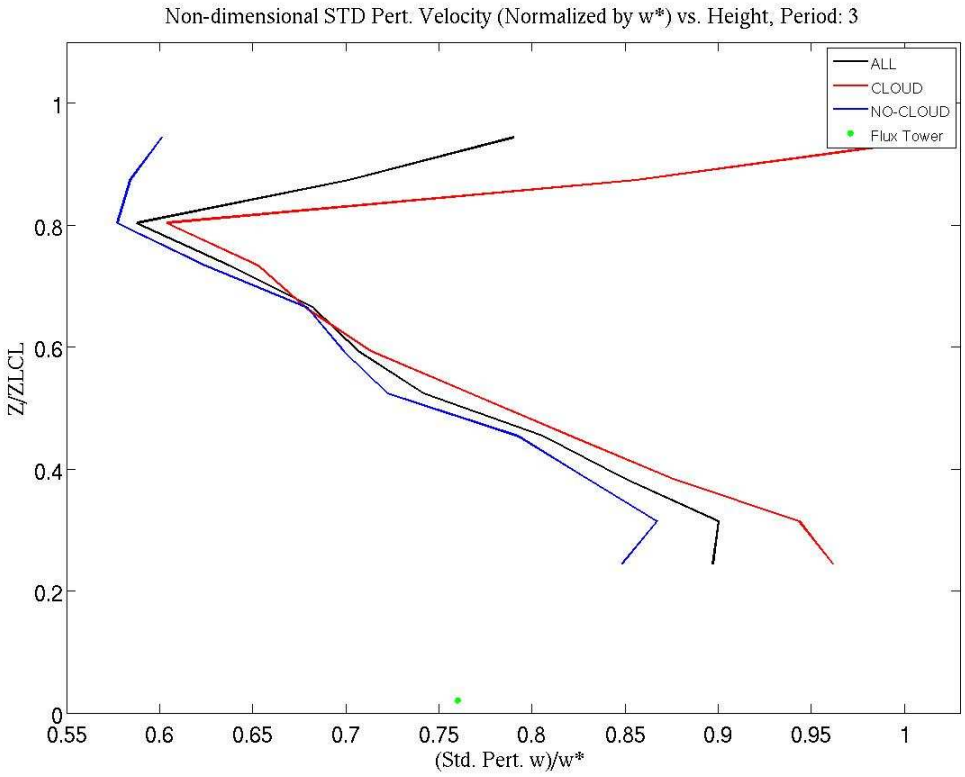


Figure 4.16: As in Figure 4.12, except for SP3 (January 20$^{th}$-21$^{st}$).

The spectra show that low frequency motions follow the expected -5/3 slope line of turbulence even more closely than the previous two periods. There is still a deviation from this line above 10 seconds due to noise (Fig. 4.17), though the small peaks due to ship motion have decreased as the lower wind speeds during this period caused less ship motion. Cloud-scale processes are not evident in this figure as the clouds observed were too weak and shallow (vertical extent of <200 m) to have an influence on the subcloud region.

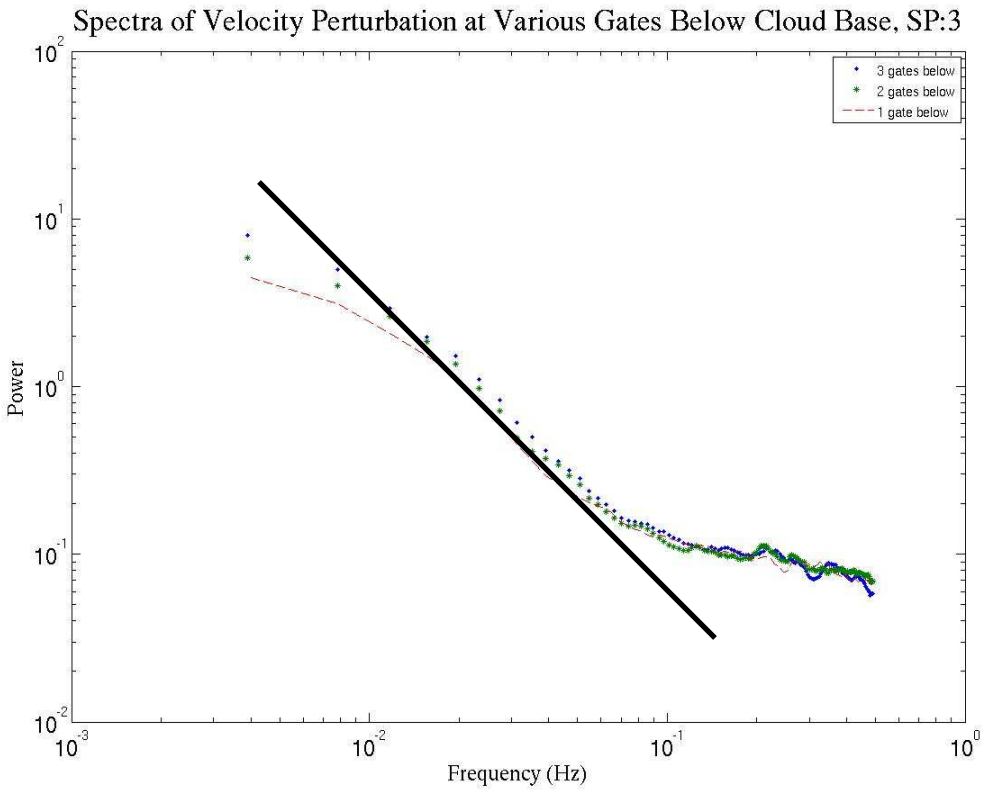


Figure 4.17: As in Fig. 4.13, but for SP3.

Figure 4.18 shows turbulence results for SP4, which was had mostly suppressed weather conditions similar to SP3 although the cloud interaction with the subcloud layer was increasing and cloud tops started to penetrate the strong TWI. As in the previous four periods, the variance of w' under clear sky decreases with height, while under clouds it decreases at first and then increases just below cloud base. The clear sky curve in Fig. 4.18 again follows that of Nicholls and LeMone, as do the lower parts of the ALL and CLOUD profiles, although they increase with height just below cloud base. This is most likely due to the influence of increasing updrafts and downdrafts associated with the increasing cloud activity during this period, showing again how convection alters the expected turbulence curve.

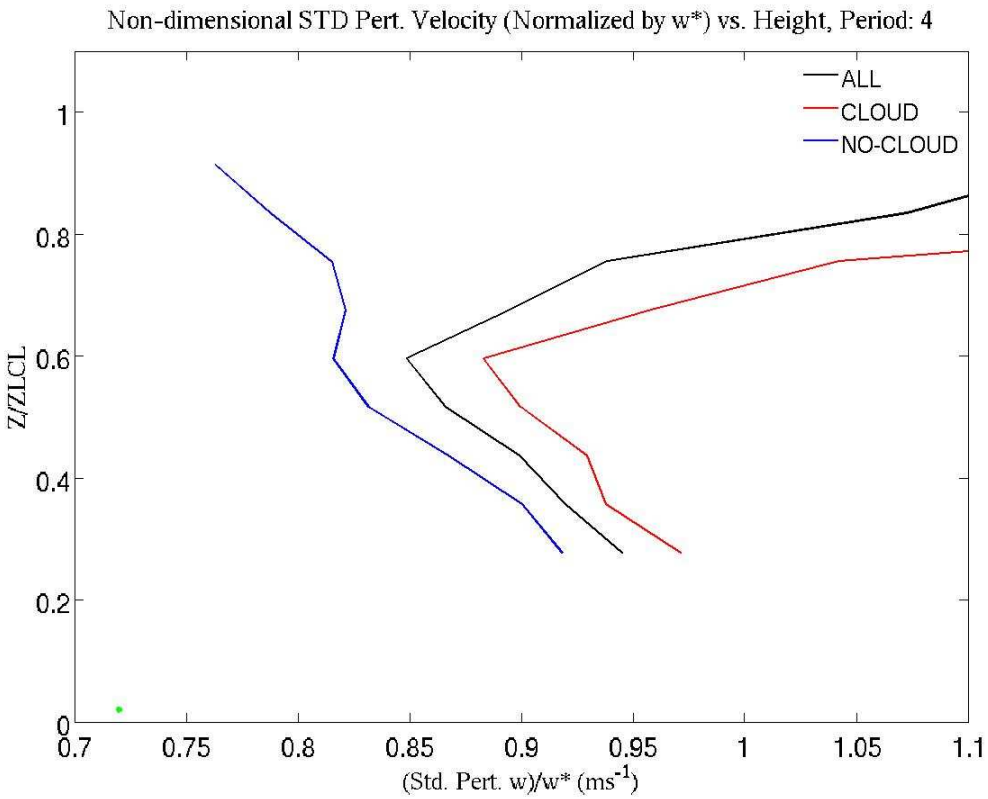


Figure 4.18: As in Figure 4.12 except for SP4 (January 22$^{nd}$-24$^{th}$).

Figure 4.19 shows the spectra of the perturbation velocity for SP4. As in the previous three synoptic periods, low frequency motions follow the expected -5/3 slope line of turbulence and the high frequency noise deviates from this line. There is slightly more variance just below cloud base in this figure, which supports the idea that the increasingly active clouds seen in SP4, while not as convective as SP1 or SP2, are still affecting the subcloud layer.

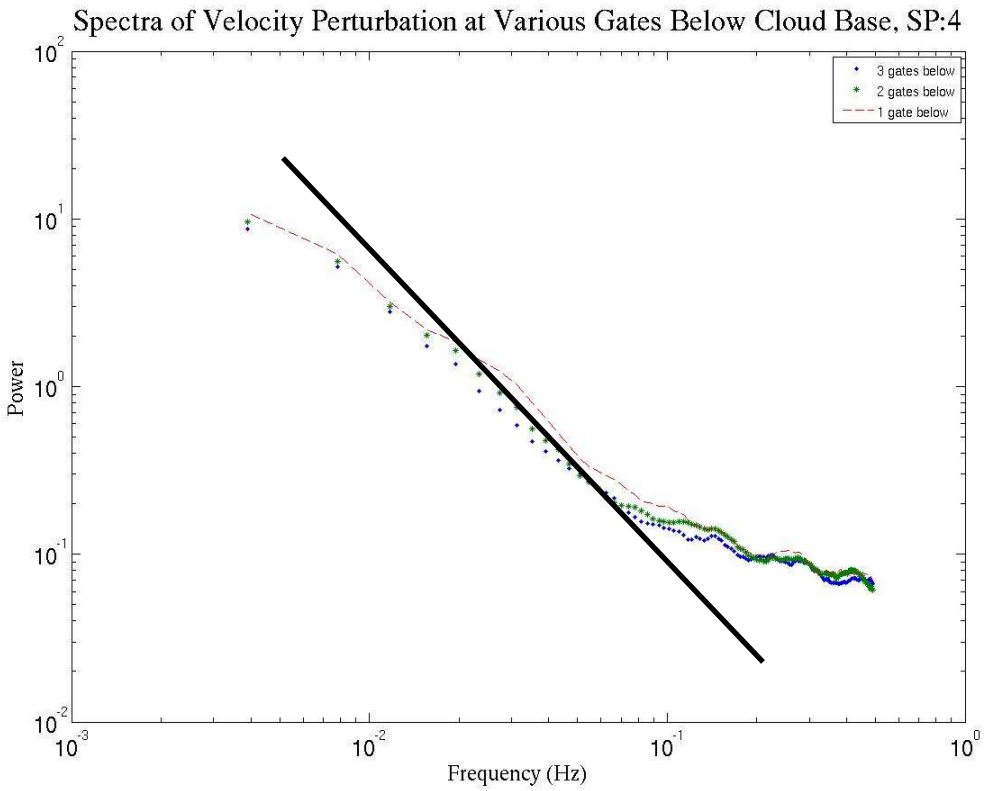


Figure 4.19: As in Fig. 4.13, but for SP4.

Figure 4.20 shows the turbulence profiles of all conditions by each Synoptic Period (solid lines). Normalizing each profile by w* allows for days with different types of weather conditions to be compared on the same image. Here we see that SP2, SP3 and SP4 all have profiles that collapse together when normalized by w*. These three profiles are similar to the results seen during GATE, shown here as magenta stars. Adding the normalized flux tower values from each period to this image shows how the lidar curves could be interpolated to the surface and follow a similar shape as the GATE curve. It appears that the peak variance in the RICO curves occurs at a lower height then the GATE curve, but since the lowest height returns for the lidar are not very reliable, it is hard to say exactly where the peak would be located. Also, if we assume that due to averaging the cloud base is located closer to 0.8 $Z/Z_{LCL}$ then the upper portion of the lidar

curves would be stretched relative to the GATE curve. The turbulence curve and flux tower point from SP1 are slight outliers on this figure, which is expected due to the drastically different convective conditions observed during this period. Also, this period had the most days of all of the Synoptic Periods (5 compared with 2 from SP2 and SP3 and 3 from SP4), and averaging over more days provides more samples and leads to more opportunity for an increased standard deviation.

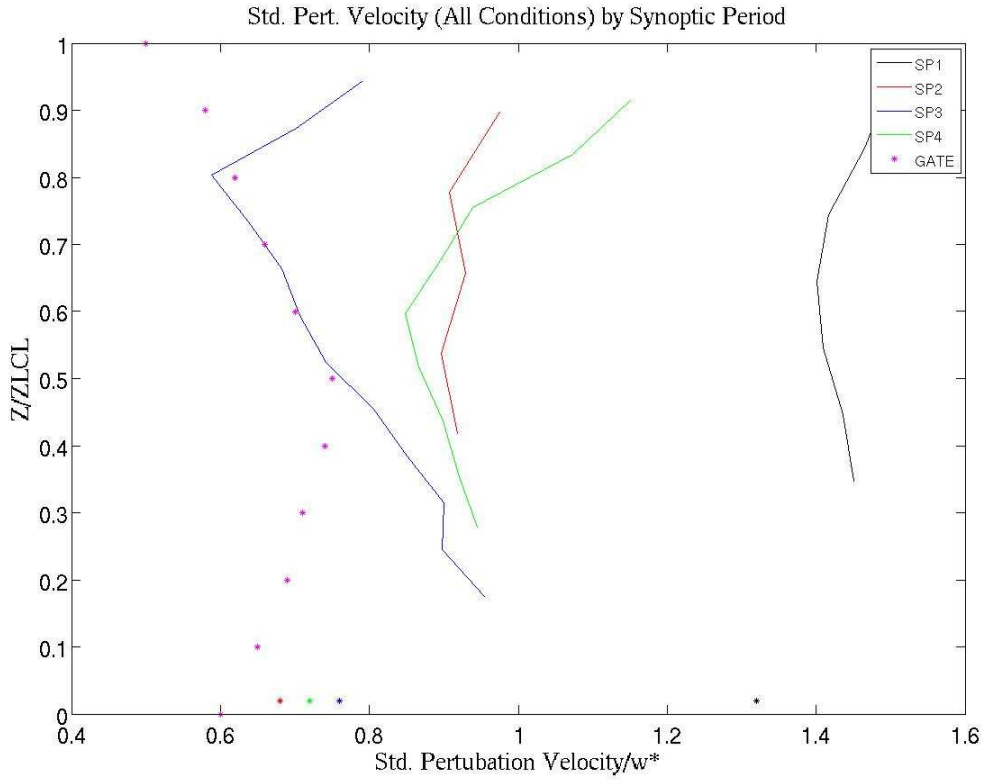


Figure 4.20: Standard deviation of w' for all conditions. Each Synoptic Period is shown as a solid line and is normalized by the mean w* during that period. The flux tower $\sigma_w/w^*$ observations are shown as stars (black for SP1, red for SP2, blue for SP3 and green for SP4). Observations collected during GATE by Nicholls and LeMone (1980) are shown as magenta stars for comparison purposes.

### 4.5.2 Updrafts

As in section 4.5.1, each synoptic period composite file was used to calculate mean and standard deviation of w’ for strong updrafts vs. downdrafts. Strong updrafts are classified as any column which has w>1m/s below cloud base. The results are shown as a set of two images for each synoptic period where the top image is the mean w’ and the bottom is the standard deviation of w’. It is important to remember that due to the scaling of height by LCL and averaging over several days, cloud base is probably closer to 0.8 $Z/Z_{LCL}$ than 1.0 $Z/Z_{LCL}$ for these figures. Figure 4.21 shows these results for SP1 where the red profiles represent conditions under strong updrafts, the blue profiles represent profiles under weak updrafts or downdrafts and the black profiles are an average of all conditions. For SP1, we see that the mean w’ for updrafts is always positive (which is expected), though it does decrease slightly with height, leading to the conclusion that the updrafts are stronger in the middle of the subcloud layer than they are just under cloud base. The variance of w’ for updrafts decreases with height in the lower subcloud layer, then increases with height into cloud base. This is due to the fact that just below cloud base some updrafts become stronger while profiles that have an updraft at lower levels may see a downdraft just below cloud base as seen by the decreasing values of w’ in the UPDRAFT profile.

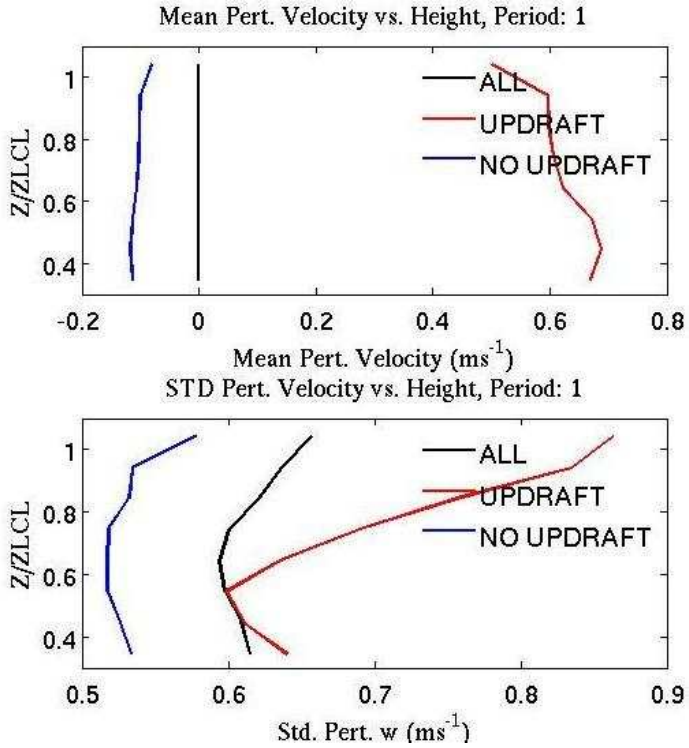


Figure 4.21: Turbulence profiles from SP1 (January 10th-14th). Upper panel: Mean w'; Lower panel: Standard Deviation of w'. In all plots, the red curve represents columns with an updraft of 1 m/s or greater, blue curves represent columns without a strong updraft and black represents all columns.

Figure 4.22 shows these results for SP2 where again we see that the mean w' for updrafts is always positive and decreasing towards cloud base, though now the velocity values are weaker than SP1. The variance of w' for updrafts again decreases with height in the lower subcloud layer, then increases with height in the middle of the subcloud layer before decreasing into cloud base. The increase in variance in the middle of the subcloud layer is most likely due to varying strengths of updrafts and vertical transports depending on whether or not a cloud is present overhead.

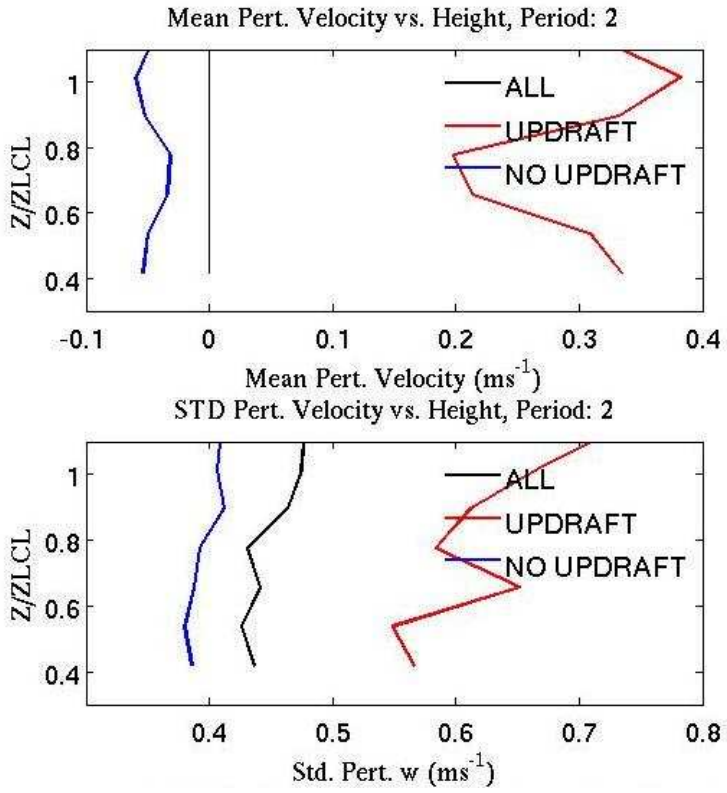


Figure 4.22: As in Figure 4.21, except for SP2 (January 18th-20th).

Figure 4.23 shows these results for SP3 where yet again the mean w' for updrafts is always positive. During this period it increases in strength in the lower subcloud layer before decreasing dramatically up to cloud base. This increase again implies that the updrafts are stronger in the middle of the subcloud layer than they are just under cloud base, as only the surface fluxes seem to be affecting the subcloud layer during this period. The overall variance of w' for updrafts decreases with height, though it does have a couple of jumps of increasing variance, one in the lower subcloud layer and one just below cloud base. The jump in variance below cloud base is probably caused by strong updrafts occurring at the same time as weak updrafts or downdrafts out of the clouds.

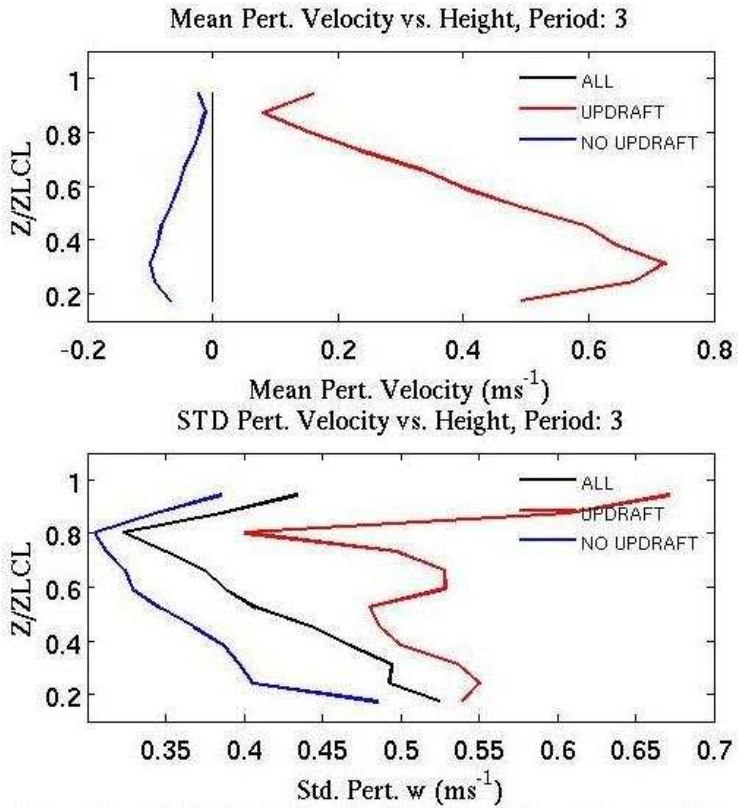


Figure 4.23: As in Figure 4.21, except for SP3 (January 20th-22nd).

Figure 4.24 shows these results for SP4 where we see that the mean w' profile for updrafts is similar to that seen during SP2, as it is positive but decreasing up to cloud base (here seen around 0.6 $Z/Z_{LCL}$). The variance of w' for updrafts decreases with height until just below cloud base and then increases going into cloud base due to the presence of both updrafts and downdrafts under the clouds.

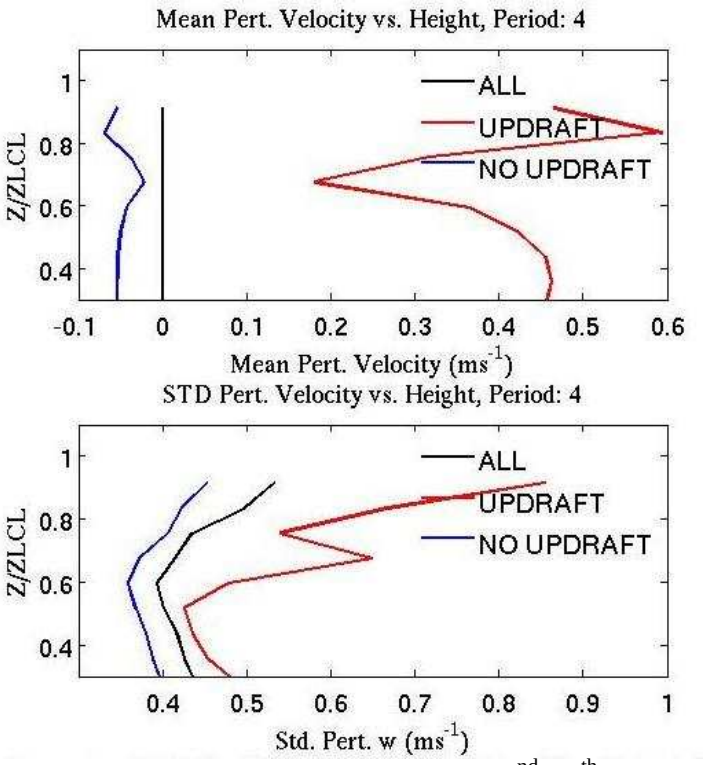


Figure 4.24: As in Figure 4.21, except for SP4 (January 22nd-24th).

### 4.5.3 Cloud and Updraft Occurrences

Table 4.4 shows percentages of time that clouds, updrafts and both occur during each Synoptic Period as well as a cruise average, all calculated using lidar data. Cloud cover is lowest during SP2, although this is not consistent with ceilometer observations (Fig. 3.21) as the fractional cloudiness was lower in the afternoons when most of the lidar observations were collected. The overall percentage cloud cover is 30%, which is slightly lower than the ceilometer value of 39%, but the lidar was not running at night when higher cloud fraction was observed, so the lidar values should be lower. Strong updrafts occur 13-14% of the time during SP1 and SP2, which have more convective conditions, but decrease to 10-11% during the more calm conditions of SP3 and SP4, which is shown in the lower mass flux values during the later periods. Interestingly, the correlations

between clouds and strong updrafts remain constant with each period, and imply that 1 in 4 FWC will have an active updraft. This number is significantly higher than the current 2-3% used in models, and may be due to the fact that I included strong updrafts occurring anywhere in the subcloud region. It is possible that looking at only strong updrafts in the gate or two below cloud base would cause my percentage to decrease, and that will be considered during future work. The average velocity at cloud base is strongest during SP2, which is expected with more strong updrafts. However, it is slightly negative during SP1, which means that despite more strong updrafts in the subcloud region, downdrafts still played a dominating role at cloud base. Mean velocity in the lowest 600m is highest in SP2, signifying either more moderate updrafts or stronger updrafts overall during this period since the percentage of updrafts is not any higher during this time span than SP1. Variance values below cloud base and in the lowest 600 m are highest during SP4, which is due to the variation in conditions (more clouds, updrafts and higher velocities on the 22$^{nd}$ and less updrafts and negative velocities on the 24$^{th}$). The highest variance values are seen for all the days, again this is expected due to the wide range of conditions encountered during RICO.

| Synoptic Period | Dates in January 2005 | % Clouds | % Strong Updrafts | % Clouds & Updrafts | Average Velocity at Cloud Base (m/s) | STD of Perturb-ation Velocity at Cloud Base (m/s) | Mean Velocity in Lowest 600m | STD Velocity in Lowest 600m |
|---|---|---|---|---|---|---|---|---|
| **1** | $10^{th}$-$15^{th}$ | 28.3 | 14.5 | 6.29 | -0.024 | 0.426 | 0.039 | 0.028 |
| **2** | $18^{th}$-$20^{th}$ | 17.5 | 13.2 | 5.66 | 0.110 | 0.490 | 0.121 | 0.088 |
| **3** | $20^{th}$-$22^{nd}$ | 38.1 | 12.0 | 6.88 | 0.019 | 0.434 | 0.032 | 0.063 |
| **4** | $22^{nd}$-$24^{th}$ | 47.0 | 10.4 | 6.69 | 0.085 | 0.534 | 0.081 | 0.171 |
| | | | | | | | | |
| **ALL** | $9^{th}$-$24^{th}$ | 30.1 | 13.6 | 7.07 | 0.072 | 0.569 | 0.051 | 0.089 |

Table 4.4: A list of cloud, updraft, and turbulence statistics by Synoptic Period during RICO

# Chapter 5- Discussion and Future Work

## 5.1 Summary

Ship-based observations of marine fair weather cumulus clouds during RICO have been used to classify the boundary layer structure in the tropical Atlantic trade wind regime. RICO was the first field experiment to focus on this environment in several decades and provided new data sets about the region using new or improved technology. It was also the first experiment in this region in which a lidar was included in the ship instrumentation, which allowed for a detailed view of the small-scale variations in the subcloud layer. Here, observations from the soundings launched during RICO are used to document the structure and variability of the boundary layer and observations from the flux tower are used to provide a description of surface variables and rainfall throughout the cruise. Vertically pointing lidar data is used to study the subcloud vertical velocities and calculate turbulence statistics for clouds, clear-sky and strong updrafts. These results may be useful for future implementation in Large Eddy Simulation (LES) Models as the detailed lidar observations can accurately describe the spatial extent of the subcloud eddys. Some of the main features observed during RICO are summarized below.

-During RICO, 4 distinct weather conditions were experienced that appeared to be forced by synoptic-scale variations. This first period (SP1) occurred from January 10$^{th}$ - 14$^{th}$ and saw strong easterly winds, a moist BL with frequent rain showers, and convective clouds due to a significant amount of CAPE. SP2 occurred between January 18$^{th}$ and 20$^{th}$ and was a period of transition. Conditions were still convective, though not

as much rainfall occurred. Winds came out of the NE and decreased significantly in magnitude. SP3 occurred from January 20$^{th}$-22$^{nd}$ and saw the most typical trade wind conditions with light easterly winds and very little convection or precipitation. Clouds were present but they were very weak and shallow. SP4 occurred between January 22$^{nd}$ and 24$^{th}$ and was similar to SP3 except with increasing temperatures and moisture. The weather, cloud, and turbulence conditions observed are as follows:

-Air temperatures were around 23.5-26.0 $^{o}$C while SSTs were fairly constant around 26.0 $^{o}$C.

- Wind speeds were high during the first leg of the cruise and then decreased dramatically during Leg 2. Winds were easterly throughout the lowest 4 km of the BL except for a lowering of westerlies down to 2 k during SP3 and SP4.

-Cloud cover during RICO was observed with a ceilometer to be more frequent than previous experiments with a cloud fraction of .39. This could be attributed to the fact that previous experiments calculated fractional cloudiness visually while RICO used a ceilometer. Contrary to previous experiments which saw a 20% increase of clouds at night, RICO saw less than a 10% increase. Most of the time during RICO saw cloud fractions between 0-.10. Lidar observed fractional cloudiness was typically significantly lower than the ceilometer due to only making observations a total of 2-3 hours per day.

- Spectra of vertical velocity perturbation from the lidar show the most variation in the gate just below cloud base. Low frequency motions closely follow the expected -5/3 slope line of turbulence. High frequency motions deviate from this line and are mostly due to noise.

-Daily turbulence profiles have 4 different structures for cloudy vs. clear conditions and days with similar structures span the synoptic periods.

-According to the lidar, clouds are present between 10-65% of the time while updrafts are present between 21-45% of the time. Strong updrafts (w>1 m/s) are present between 8-28% of the time with the higher percentages occurring during SP1.

-Mass flux is found to decrease with height up towards cloud base although the mass flux values are much higher during SP1 and SP2 and coincide with increased convection.

- Turbulence profiles of cloudy vs. clear conditions show that during suppressed conditions, the variance in w' decreases with height from the middle of the subcloud layer up to cloud base. The addition of the flux tower w' allows for interpolation down to the surface and provides a curve similar to that found by Nicholls and LeMone (1980) during suppressed conditions. However, during convective conditions, the cloud profiles are found to increase in variance with height into clouds base, showing the influence of updrafts going into the cloud and downdrafts coming out of the clouds. The weak clouds found during suppressed conditions in previous experiments did not have strong enough updrafts or downdrafts to see this result, so this structure is a new result as the clouds are developed enough to dominate dynamics lower in the atmosphere.

-Turbulence profiles of strong updrafts vs. weak updrafts and downdrafts show the mean w' in updraft columns decreasing with height up to cloud base leading to the conclusion that either the updrafts are stronger in the middle of the subcloud layer than they are just under cloud base or that columns that have a strong updraft lower in the subcloud layer often have downdrafts just below cloud base.

- Despite changing synoptic influences, the correlations between clouds and strong updrafts remain constant with each synoptic period.

- Average velocity at cloud base is strongest during SP2, which is expected with more strong updrafts. However, it is slightly negative during SP1, which means that despite more strong updrafts in the subcloud region, downdrafts still played a dominating role at cloud base.

### 5.2 Outlook and Future Work

The winter months in the Northern Hemisphere typically provide the best time to sample marine fair weather cumulus clouds without the influence of intense convection or organized tropical systems. While RICO was planned to study the typical suppressed conditions, the first half of the cruise encountered disturbed conditions. This turned out be useful as the disturbed period turbulence statistics were compared to the typically observed suppressed statistics and a different turbulence structure was found to be present during convective conditions. The documentation of these results along with the overall observed variability in the MABL and clouds is an important step in understanding the physical processes that contribute to the formation, maintenance and dissipation of marine FWC.

Our current understanding of marine FWC and the MABL in the trade wind regime comes from experiments that took place during the 1970s. Since that time, the majority of progress in understanding the processes occurring in this region came from modeling. The RICO data set will provide a new comparison for these modeled results. Neverless, parameterization schemes, model evaluations and general assessments based solely on

the findings from RICO may be valid only for specific cases or time periods and not the entire trade wind regime. This is especially true for the convective conditions encountered as this type of weather is generally expected to occur in the late fall or early spring as transitions to or from the suppressed wintertime conditions. Future experiments in the marine environment of the tropical Atlantic trades would be helpful to determine if the convective conditions encountered during RICO are truly more common during the winter months than previously thought. It would also be helpful to have a lidar on an experiment solely devoted to vertical stares in order to calculate more trustworthy vertical velocity and turbulence statistics.

Some of the results obtained in this study can be directly correlated to satellite data or model parameterization for boundary layer structures and turbulence processes in the subcloud layer. A deeper analysis of the data should reveal even more interesting features, and could be used for evaluating specific satellite products and boundary-layer model simulations. For instance, Zhao and Di Girolamo (2006) found that the Advanced Spaceborne Thermal Emission and Reflection Radiometer (ASTER) saw a cloud fraction of only 0.08 during RICO. They filtered out all clouds except trade wind cumuli so the overall cloud fraction should be lower than that shown in thesis, but this result is significantly lower, which bears further studying. As other data sets from RICO are processed and analyzed in the next few years, a better understanding of marine FWC should emerge and new results can be implemented into models.

# APPENDIX

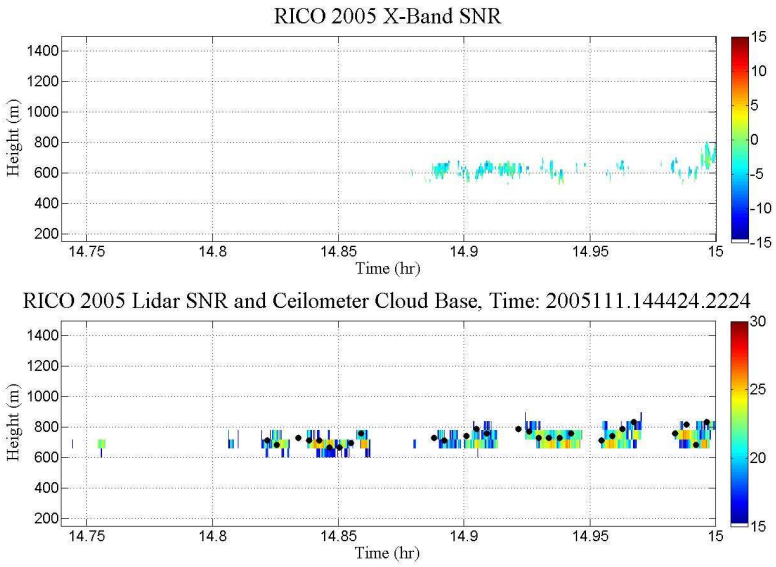


Figure A1: Time-height mapping reflectivities from January 11, 2005. The upper panel shows SNR from the X-band radar and the lower panel shows SNR from the lidar (colorbar) and ceilometer cloud base (black dots). This figure shows that the shorter wavelength of the lidar is much more sensitive to small, shallow cumulus clouds than the X-band radar, as the lidar finds the exact same cloud information as the ceilometer. The X-band only finds the stronger clouds.

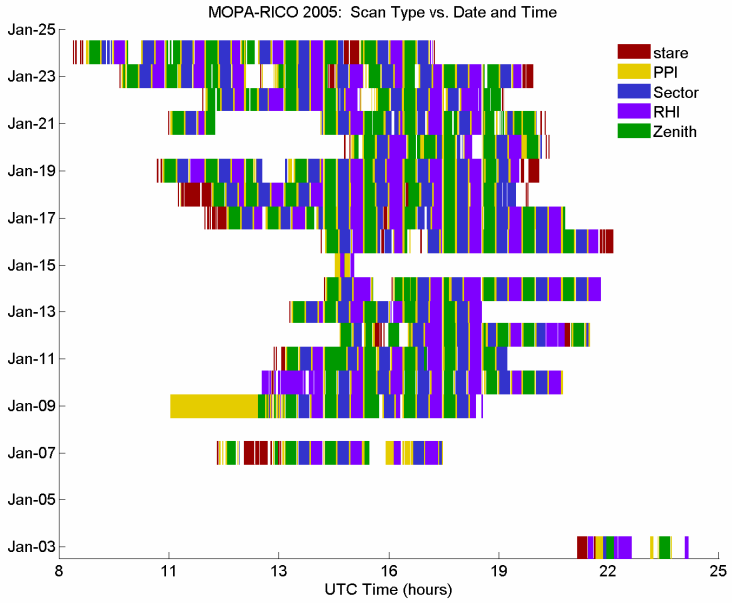


Figure A2: Lidar scan type by day and hour during RICO.

| **Date in January** | **Mean w* (m/s)** |
|---|---|
| 9th | 0.460 |
| 10th | 0.340 |
| 11th | 0.336 |
| 12th | 0.448 |
| 13th | 0.532 |
| 14th | 0.466 |
| 16th | 0.654 |
| 17th | 0.268 |
| 18th | 0.426 |
| 19th | 0.525 |
| 20th | 0.549 |
| 21st | 0.550 |
| 22nd | 0.507 |
| 23rd | 0.466 |
| 24th | 0.418 |

Table A1: Mean convective velocity scale value (m/s) per day.

| DATE in January 2005 | # Useable Lidar Zenith Files |
|---|---|
| 9th | 5 |
| 10th | 9 |
| 11th | 6 |
| 12th | 3 |
| 13th | 5 |
| 14th | 5 |
| 16th | 6 |
| 17th | 8 |
| 18th | 6 |
| 19th | 6 |
| 20th | 3 |
| 21st | 5 |
| 22nd | 7 |
| 23rd | 3 |
| 24th | 6 |

Table A2: A list of the number of useful lidar zenith stare files each day during RICO.

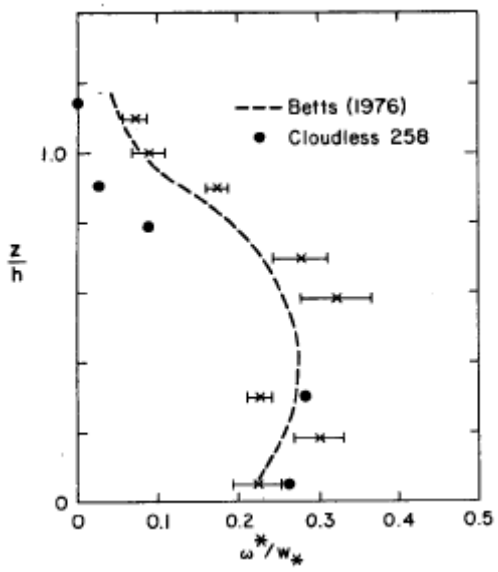


Figure A3: Mass flux normalized by w* from Nicholls and LeMone (1980). Solid circles represent clear sky days while the averages from days with cumulus cover are shown as x with a standard deviation bar. The curve is from results of Betts (1976a).

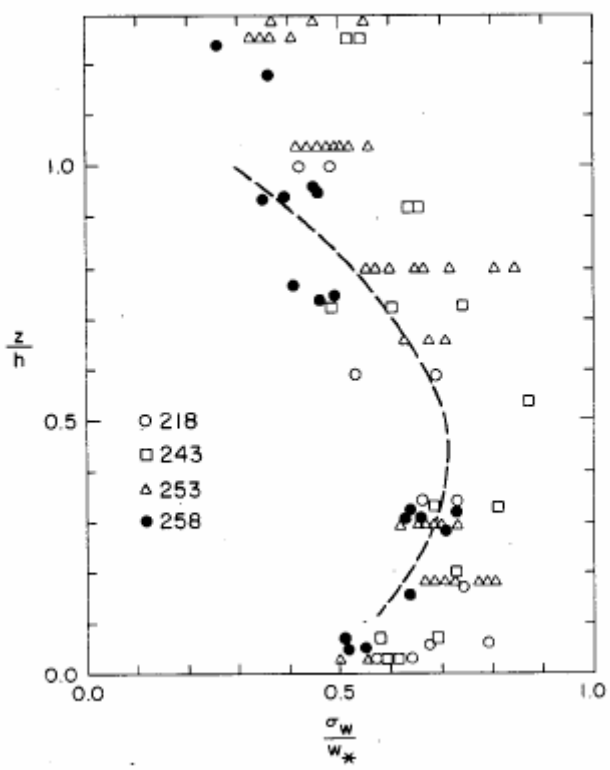


Figure A4: Profile of standard deviation of vertical velocity normalized by w* from Nicholls and LeMone (1980). Solid circles represent clear sky days while the open circles, squares and triangles are days of weak cumulus clouds. The dashed curve is from the laboratory results of Willis and Deardorff (1974).

# BIBLIOGRAPHY

Albrecht, B. A., 1981: Parameterization of trade-cumulus cloud amounts, *J. Atmos. Sci.*, **38**, 97-105.

——, 1989: Aerosols, cloud microphysics, and fractional cloudiness. *Science,* **245**, 1227-1230.

——, 1993: Effects of precipitation on the thermodynamic structure of the trade wind boundary layer. *J. Geo. Res.*, **98**, 7327-7337.

——, M. P. Jensen, and W. J. Syrett, 1995: Marine boundary layer structure and fractional cloudiness. *J. Geophys. Res.,* **100,** 14209–14222.

Augstien, E., H. Riehl, F. Ostapoff and V. Wagner, 1973: Mass and energy transports in an undisturbed Atlantic tradewind flow. *Mon. Wea. Rev*., **101**, 101-111.

——, H. Schmidt, F. Ostapoff, 1974: The vertical structure of the atmospheric planetary boundary layer in undisturbed trade winds over the Atlantic Ocean. *Bound-Lay Meteorol*., **6**, 129-150.

Bellon, G., and B. Stevens, 2005: On bulk models of shallow cumulus convection. *J. Atmos. Sci.*, **62**, 3286-3302.

Betts, A. K., 1974: Thermodynamic classification of tropical convective soundings. *Mon. Wea. Rev*., **102**, 760-764.

——, 1975: Parametric interpretation of trade wind cumulus budget studies. *J. Atmos. Sci.*, **32**, 1934-1956.

——, 1976a: Modeling subcloud layer structure and interaction with a shallow cumulus layer. *J. Atmos. Sci*., **33**, 2363-2382

——, 1976b: The thermodynamic transformation of the tropical subcloud layer by precipitation and downdrafts. *J. Atmos. Sci.*, **33**, 1008-1020.

Brewer, W. A., R. M. Hardesty, W. L. Eberhard, and B. J. Rye, 1998: Combined wind and water-vapor measurements using the NOAA Mini-MOPA Doppler lidar. Proceedings of the 19th International Laser Radar Conference, NASA Langley Research Cent., Hampton, VA, pp. 565-568.

Bolton, D., 1980: The computation of equivalent potential temperature. *Mon. Wea. Rev*., **108**, 1046-1053.

Bretherton, C. S. and S. Park, 2007: A new bulk shallow cumulus-topped boundary layer model. Submitted to *J. Atmos. Sci*, in press.

Caesar, K.A.: Summary of the weather during the RICO project- December 8th, 2004 and January 24th, 2005. *Caribbean Institute for Meteorology and Hydrology*, January 2005.

Davies, F., C. G. Collier, G. N. Pearson, and K. E. Bozier, 2004: Doppler lidar measurements of turbulent structure function over an urban area. *J. Atmos. Oceanic Technol*., **21**, 753-761.

Donner, L. J., 1993: A cumulus parameterization including mass fluxes, vertical momentum dynamics, and mesoscale effects. *J. Atmos. Sci.*, **50**, 889-906.

Emanuel, K. A., and M. Bister, 1996: Moist convective velocity and buoyancy scales. *J. Atmos. Sci.*, **53**, 3276-3285.

Emmitt, G. D., 1978: Tropical cumulus interaction with and modification of the subcloud region. *J. Atmos. Sci.*, **35**, 1485-1502.

Hill, R. J., S. Tucker, and W. A. Brewer, 2006: Ship-motion correction of the Doppler velocity measured by the NOAA Mini-MOPA lidar. *J. Atmos. Oceanic Tech*., manuscript in preparation.

Holland, J. S., and E. M. Rasmusson, 1973: Measurements of the atmospheric mass, energy and momentum over 500-kilometer square of tropical ocean. *Mon. Wea. Rev*., **101**, 44-55.

Hoppel, W. A., J. W. Fitzgerald, G.M. Frick, R. E. Larson, and E. J. Mack, 1990: Aerosol size distributions and optical properties found in the marine boundary layer over the Atlantic Ocean. *J. Geophys. Res.*, **95,** 3659-3686.

Kalnay et al., 1996: The NCEP/NCAR 40-year reanalysis project, *Bull. Amer. Meteor. Soc*., **77**, 437-470.

Kollias, P., B.A. Albrecht, 2000: The turbulence structure in a continental stratocumulus cloud from millimeter-wavelength radar observations. *JAS*, **57,** 2417-2434.

Kollias, P., B.A. Albrecht, R. Lhermitte, A. Savtchenko, 2001: Radar Observations of Updrafts, Downdrafts, and Turbulence in Fair-Weather Cumuli. *JAS*, **58**, 1750-1765.

Lothon, M., D. H. Lenschow, S. D. Mayor, 2006: Coherence and scale of vertical velocity in the convective boundary layer from a Doppler lidar. *Bound-Lay Meteorol*., **16,** 521-536.

Lottman, B. T., R. g. Frehlich, S. M. Hannon, and S. W. Henderson, 2001: Evaluation of vertical winds near and inside a cloud deck using coherent Doppler lidar. *J. Atmos. Oceanic Technol*., **18**, 1377-1386.

LeMone, M. A., and W. T. Pennell, 1976: The relationship of trade wind cumulus distribution to subcloud layer fluxes and structure, *Mon. Wea. Rev*., **104**, 524-539.

Malkus, J. S., 1958: On the structure of the trade wind moist layer. *Pap. Phys. Oceanogr. Meteor*., **13**, No. 2.

Nicholls, S. and M. A. LeMone, 1980: The fair weather boundary layer in GATE: The relationship of subcloud fluxes and structure to the distribution and enhancement of cumulus clouds. *J. Atmos. Sci.*, **37**, 2051-2067.

Pennell, W. T., and M. A. LeMone, 1974: An experimental study of turbulence structure in the fair weather trade wind boundary layer. *J. Atmos. Sci.*, **31**, 1308-1323.

Rauber, R. M., B. Stevens, J. Davison, S. Goke, O. L. Mayol-Bracero, D. Rogers, et al., 2007a: In the driver's seat- RICO and education. *Bull. Amer. Meteor. Soc.*, in review.

Rauber, R. M., B. Stevens, H. T. Ochs III, C. Knight, B. A. Albrecht, A. M. Blyth, et al., 2007b: Rain in (shallow) cumulus over the ocean- the rico campaign. *Bull. Amer. Meteor. Soc*., in review.

Siebesma, A. P., C. S. Bretherton, A. Brown, A. Chlond, J. Cuxart, P. G. Duynkerke, et al., 2003: A large eddy simulation intercomparison study of shallow cumulus convection. *J. Atmos. Sci.*, **60**, 1201-1219.

Schubert, W. H., P. E. Ciesielski, C. Lu, and R. H. Johnson, 1995: Dynamical adjustment of the trade wind inversion layer. *J. Atmos. Sci.*, **52**, 2941-2952.

Stull, R.B, 1988: An introduction to boundary layer meteorology. Kluwer Academic Publishers. 666 p.

Willis, G. E., and J. W. Deardorff, 1974: A laboratory model of the unstable planetary boundary layer. *J. Atmos. Sci.*, **31**, 1297-1307.

Zhao, G., and L. Di Girolamo, 2006: Cloud fraction errors for trade wind cumuli from EOS-Terra instruments. *Geophys. Res. Lett*., **33**, L20802, doi: 10.1029/2006GL027088.

RICO Operations Plan, Draft from September 30, 2004.